Preparation and Properties of Functional Ionic Liquids Containing Cationic Metal Complexes

Funasako, Yusuke

(Degree)
博士（理学）

(Date of Degree)
2014-03-25

(Date of Publication)
2016-03-25

(Resource Type)
doctoral thesis

(Report Number)
甲第6121号

(URL)
https://hdl.handle.net/20.500.14094/D1006121

Doctoral Dissertation

Preparation and Properties of Functional Ionic Liquids Containing Cationic Metal Complexes

January, 2014

Graduate School of Science, Kobe University

Yusuke Funasako

CONTENTS

CHAPTER 1

General Introduction

1.1 General Features of Ionic Liquids

Ionic liquids (ILs) are salts with melting points below 100 °C. They exhibit characteristic properties such as nonvolatility, fire retardancy, and high ionic conductivity.[1] Furthermore, they can be designed for specific tasks.[2] ILs comprising organic cations have been extensively investigated in recent years. The onium-type cations often employed as the components of ILs are shown in Figure 1. The anions used for synthesizing ILs are often halogens, tetrafluoroborate (BF_4), hexafluoro phosphate (PF_6), trifluoromethanesulfonate (CF_3SO_3), and bis(trifluoromethanesulfonyl)amide (Tf_2N).

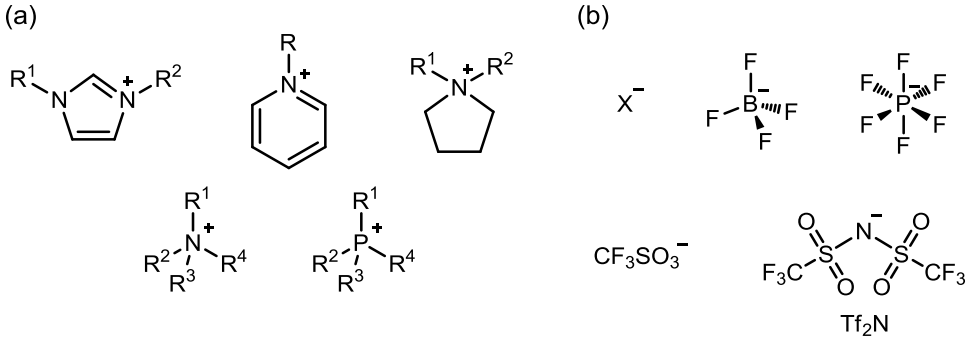

Figure 1. (a) Cations and (b) anions commonly used as components of ionic liquids.

Decreasing the melting point of ILs is critical for designing these interesting materials. The introduction of alkyl chains on the cations is a major approach for lowering the melting points of the ILs. This design reduces the molecular symmetry of the cation and increases the motional freedom. In the imidazolium salts shown in Figure 1a, the introduction of different alkyl chains into R^1 and R^2 leads to lower melting points.[3] The melting point decreases on increasing the number of carbon atoms in the alkyl chain to about 8 carbons, while the melting point increases with alkyl chain lengths longer than 8 carbons.[3] Because the Tf_2N anion has low symmetry and rotational freedom, its inclusion in ILs is effective in lowering the melting points.

1.2 Metal-Containing Ionic Liquids

Development of functional ILs has been a focus of recent investigations. One method to obtain such ILs is to introduce metal ions on to the cations or anions. Functionalization of cations typically involves the introduction of metal-containing substituents on the onium cation and the use of cationic metal complexes. Examples of ILs with metal complexes on to the imidazolium cation are shown in Figure 2.[4] These salts are designed to be used as catalysts by the dissolution in ILs. Introduction of the ferrocenyl substituent on to the alkyl chain produces ILs with redox activities (Figure 2d).[5]

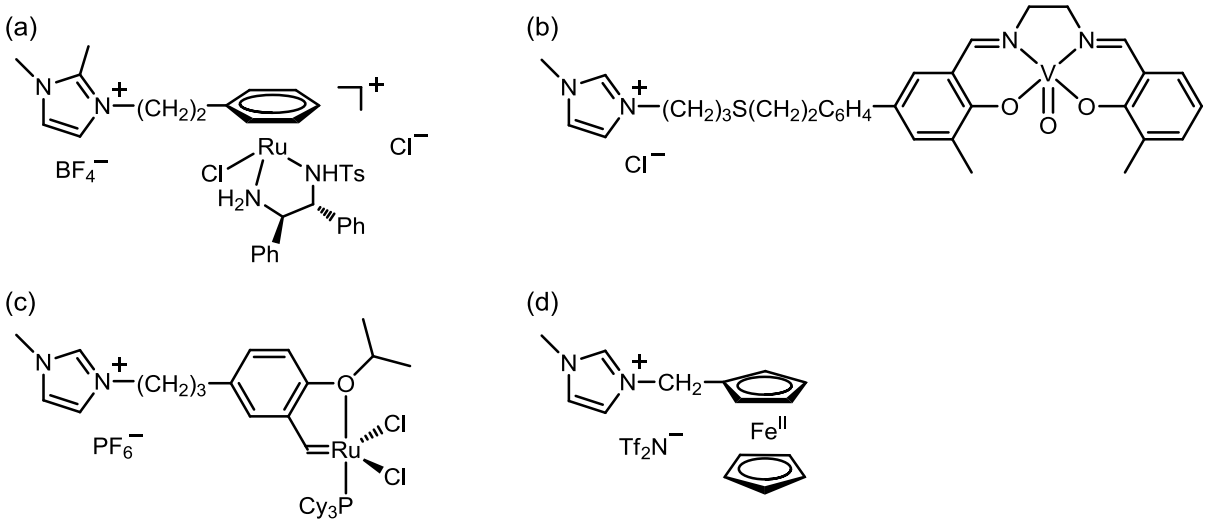

Figure 2. Catalytic ionic liquids (a–c) and redox-active ionic liquids (d) designed by introducing functional metal complexes on onium cations.

There are few examples of ILs employing cationic metal complexes. ILs containing Li–glyme complexes are produced by mixing glyme and Li[Tf_2N]. They are suitable as electrolytes for lithium ion batteries because they contain a high concentration of the lithium ion (Figure 3a).[6] These ILs show high thermal stabilities, wide electrochemical potential windows, high ionic conductivities, and high lithium ion transference numbers. ILs comprising Ag complexes (Figure 3b) generate uniformly sized Ag nanoparticles when reacted with reducing agents.[7] ILs containing Cu and Ag complexes with acetonitrile and benzonitrile ligands have been prepared (Figure 3c)[8] for use as metal-plating

electrolytes. ILs comprising Fe, Cu, Mn, and Zn complexes with $NH(CH_2CH_2OH)_2$ ligands (Figure 3d) are redox-active ILs.[9] Although such ILs contain a polyvalent cation, they are still considered as ILs. ILs comprising cationic metal complexes have attracted attention with regard to their applications in electrochemistry. However, further development of such ILs will lead to a much wider variety of applications.

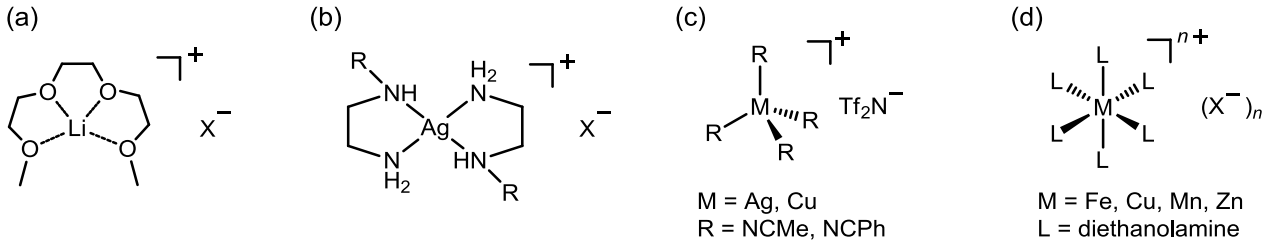

Figure 3. Example of ILs consisting of cationic complexes. (a) Li–glyme complex, (b) bis(alkylethylenediamine)silver(I) complexes, (c) tetrakis(nitrile)metal(I) complexes, (d) hexa(diethanolamine)metal(II) complexes.

Organometallic ILs with metallocenium cations were reported by our group (Figure 4). Simple cationic sandwich complexes bearing alkyl or halogen substituents yield ILs with the Tf_2N anion.[10] Ferrocenium and cobaltocenium ILs $[M(C_5H_4R^1)(C_5H_4R^2)][Tf_2N]$ (M = Fe, Co; Figure 4a) as well as arene-ferrocenium ILs $[Fe(C_5H_4R^1)(C_6H_5R^2)][Tf_2N]$ (Figure 4b) have been prepared and their physical properties have been investigated.[10] Ferrocenium ILs are deep-blue paramagnetic fluids, whereas cobaltocenium ILs and arene-ferrocenium ILs are orange and reddish-orange diamagnetic liquids, respectively. The ferrocenium ILs are readily prepared by a one-step, solvent-free reaction. Comparison of the physical properties of these ILs revealed the effects of molecular symmetry on their melting points. Simple cationic "piano-stool" half-metallocenium cations $[(C_5R_5)Fe(CO)_2L]^+$ also generate ILs with the Tf_2N anion (Figure 4c).[11] These ILs exhibit solvent-free ligand-exchange reactions associated with gas or vapor absorption to generate more thermally stable complexes. On

the basis of their reactivities, multistep solid-to-liquid and liquid-to-solid transformations have been reported. As related examples, ILs containing polyalkylated-ferrocenium cations with mesogenic anions (Figure 4d)[12] and cationic arene-ruthenium complexes (Figure 4e–f)[13] have been reported.

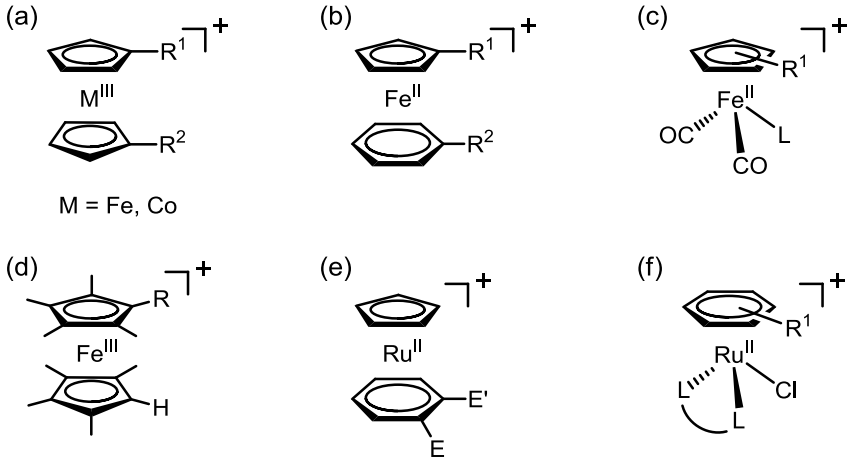

Figure 4. Metallocenium cations of ionic liquids. (a) Ferrocenium and cobaltocenium, (b) arene-ferrocenium, (c) half-ferrocenium, (d) polyalkylated-ferrocenium, (e) arene-ruthenocenium, and (f) arene-ruthenium cations.

The use of metal-containing anions represents another approach toward designing functional ILs. In particular, MX_n-type anions (M = transition metal ion; X = halogen, carbonyl) have been extensively studied. ILs containing such anions exhibit magnetism, fluorescence, and chemical reactivity.[1f,14] ILs containing $FeCl_4$ are magnetic fluids[15] and act as oxidizers. Polymerization reactions in [Bmim]$FeCl_4$ have been demonstrated, and ILs exhibit a morphological change when such reactions are carried out under a magnetic field.[16] ILs with lanthanide-containing anions $[Ln(SCN)_{8-x}(H_2O)_x]^{x-5}$ (Ln = La, Pr, Nd, Sm, Eu, Gd, Tb, Dy, Ho, Er, and Yb) exhibit considerable magnetic susceptibility and fluorescence.[17] ILs with $[M(CO)_x]^-$ (M = Fe, Co, Mn; x = 4, 5) exhibit catalytic abilities (Figure 5a).[18] In addition to MX_n-type anions, anions of EDTA complexes with Co, Cr, and Fe produce ILs (Figure 5b).[19] These ILs are also paramagnetic fluids and exhibit

electrochromism because of the redox properties of the metal atoms. ILs with anionic uranyl complexes have also been prepared.[20] This IL shows thermochromism because of the ligand-dissociation equilibrium. Air- and water-stable ILs containing Co, Cu, Mn, and Ni complexes with β-diketonate ligands have also been reported.[21] These ILs are effective, mild, and easily recyclable catalysts and can be used as solvents for the oxidation of cyclohexene.

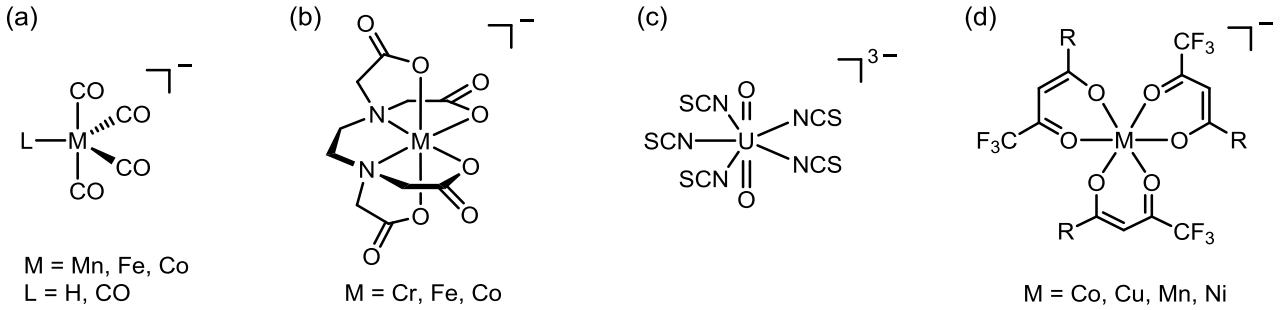

Figure 5. Ionic liquids containing anionic complexes. (a) Metal carbonyl and metal carbonyl hydride complex, (b) EDTA complexes, (c) pentakis(isothiocyanate)uranyl(IV) complex, and (d) tris(β-diketonate)metal(II) complexes.

1.3 Scope of this Thesis

The purpose of this research is to develop functional ILs with cationic metal complexes. Many ILs with metal-containing anions or with metals attached to the alkyl chains are known, but these ILs are onium salts and their properties are comparable to those of the solutions of metal complexes in ILs. ILs containing cationic complexes exhibit intrinsic functions; however, examples of such species are rare. In this research, I focused on metal-chelate complexes and metallocenes to be used as the cation for functional ILs.

In Chapter 2, the preparation and properties of ILs containing cationic metal-chelate complexes are described. Four-coordinate Cu or Ni complexes with diamine and β-diketone ligands bearing alkyl substituents rendered ILs with the Tf_2N anion. These ILs exhibited reversible color changes in response to organic vapors and gases. The color changes reflected the coordination ability or donor number of the vapor molecules. The vapor absorption also led to changes in the liquid properties such as melting point and viscosity. The Ni-containing IL exhibited a conversion between the paramagnetic and diamagnetic states by vapor absorption/desorption. After methanol absorption, the Ni-containing IL exhibited thermochromism and temperature-dependent magnetism.

Chapter 3 describes the preparation and properties of ILs comprising cationic five-coordinate Cu complexes bearing alkylimidazole-containing tripodal ligands and a Tf_2N anion. The cations with hexyl and propyl substituents produced ILs with high viscosities at room temperature. X-ray crystal structure determination and UV-vis absorption spectra revealed that the coordination geometry around the metal ion (trigonal bipyramidal or square pyramidal) in the solid state depended on the symmetry of the ligands and the packing effect.

In Chapter 4, the preparation, thermal properties, crystal structures, and magnetic properties of paramagetic alkyloctamethylferrocenium ILs are described. Salts comprising $[[Fe(C_5Me_4C_nH_{2n+1})(C_5Me_4H)]]^+$ and Tf_2N, PF_6, and NO_3 anions were synthesized. The melting points of the salts with the Tf_2N anion were near room temperature, whereas those with the PF_6 and

NO_3 anions were higher than 100 °C. X-ray crystal structure determinations revealed that the thermal properties of these salts depended on the packing structures in the solid state, influenced by the alkyl chain lengths of the cations. Among them, the Tf_2N salt bearing a butyl substituent on the cation exhibited magnetic orientation when solidified under magnetic fields. The magnetic orientation was shown to be a bulk phenomenon and the importance of the magnetic anisotropy of the crystal structure was suggested in comparison with the response of the other Tf_2N salts.

References

(1) (a) *Ionic Liquid: Industrial Applications to Green Chemistry* ACS Symposium Series 818, (Eds.: R. D. Rogers, K. R., Seddon) American Chemical Society, Washington DC, 2002; (b) A. Stark, K. R. Seddon, *Kirk-Othmer Encyclopedia of Chemical Technology, 5th ed.*, Wiley-Interscience, New York, 2007, Vol. 26, pp. 836–919; (c) M. Armand, F. Endres, D. R. MacFarlane, H. Ohno, B. Scrosati, *Nat. Mater.* **2009**, *8*, 621–629; (d) I. Krossing, J. M. Slattery, C. Daguenet, P. J. Dyson, A. Oleinikova, H. Weingärtner, *J. Am. Chem. Soc.* **2006**, *128*, 13427–13434; (e) H. Weingärtner, *Angew. Chem., Int. Ed.* **2008**, *47*, 654–670; (f) Y. Yoshida, G. Saito, *Phys. Chem. Chem. Phys.* **2010**, *12*, 1675–1684; (g) M. Freemantle, *An Introduction to Ionic Liquids*; RSC Publishing: Cambrige, 2010.

(2) J. H. Davis Jr., *Chem. Lett.* **2004**, *33*, 1072–1077.

(3) (a) P. Bonhôte, A. -P. Dias, N. Papageorgiou, K. Kalyanasundaram, M. Grätzel, *Inorg. Chem.* **1996**, *35*, 1168–1178; (b) S. V. Dzyuba, R. A. Bartsch, *ChemPhysChem* **2002**, *3*, 161–166.

(4) (a) I. J. B. Lin, C. S. Vasam, *J. Organomet. Chem.* **2005**, *690*, 3498–3512; (b) S. -g. Lee, *Chem. Commun.* **2006**, 1049–1063; (c) T. J. Geldbach, *Organomet. Chem.* **2008**, *34*, 58–73; (d) M. Pucheault, M. Vaultier, *Top. Curr. Chem.* **2010**, 1049–1063.

(5) (a) Y. Miura, F. Shimizu, T. Mochida, *Inorg. Chem.* **2010**, *49*, 10032–10040; (b) W. Wang, R. Balasubramanian, W. R. Murray, *J. Phys. Chem. C* **2008**, *112*, 18207–18216; (c) Y. Gao, B. Twamley, J. M. Shreeve, *Inorg. Chem.* **2004**, *43*, 3406–3412.

(6) T. Tamura, T. Hachida, K. Yoshida, N. Tachikawa, K. Dokko, M. Watanabe, *J. Power Sources* **2010**, *195*, 6095–6100.

(7) (a) M. Iida, C. Baba, M. Inoue, H. Yoshida, E. Taguchi, H. Furusho, *Chem. Eur. J.* **2008**, *14*, 5047–5056; (b) M. Iida, S. Kawakami, E. Syouno, H. Er, E. Taguchi, *J. Colloid Interface Sci.* **2011**, *356*, 630–638.

(8) (a) N. R. Brooks, S. Schaltin, K. Van Hecke, L. Van Meervelt, K. Binnemans, J. Fransaer, *Chem.*

Eur. J. **2011**, *17*, 5054–5059; (b) S. Schaltin, N. R. Brooks, K. Binnemans, J. Fransaer, *J. Electrochem. Soc.* **2011**, *158*, D21–D27; (c) S. Schaltin, N. R. Brooks, L. Stappers, K. Van Hecke, L. Van Meervelt, K. Binnemans, J. Fransaer, *Phys. Chem. Chem. Phys.* **2012**, *14*, 1706–1715.

(9) (a) T. M. Anderson, D. Ingersoll, A. J. Rose, C. L. Staiger, J. C. Leonard, *Dalton Trans.* **2010**, *39*, 8609–8612; (b) H. D. Pratt III, A. J. Rose, C. L. Staiger, D. Ingersoll, T. M. Anderson, *Dalton Trans.* **2011**, *40*, 11396-11401; (c) H. D. Pratt III, J. C. Leonard, L. A. M. Steele, C. L. Staiger, T. M. Anderson, *Inorg. Chim. Acta* **2013**, *396*, 78–83.

(10) (a) T. Inagaki, T. Mochida, *Chem. Lett.* **2010**, *39*, 572–573; (b) T. Inagaki, T. Mochida, M. Takahashi, C. Kanadani, T. Saito D. Kuwahara, *Chem. Eur. J.* **2012**, *18*, 6795–6804; (c) A. Chakraborty, T. Inagaki, M. Banno, T. Mochida, K. Tominaga, *J. Phys. Chem. A* **2011**, *115*, 1313–1319.

(11) T. Inagaki, T. Mochida, *Chem. Eur. J.* **2012**, *18*, 8070–8075.

(12) S. Hamada, T. Mochida, *J. Organomet. Chem.* **2013**, *725*, 34–36.

(13) (a) S. Mori, T. Mochida, *Organometallics*, **2013**, *32*, 283–288. (b) S. Mori, T. Mochida, *Organometallics* **2013**, *32*, 780–787.

(14) (a) Y. Yoshida, G. Saito, Progress in Paramagnetic Ionic Liquids, *Ionic Liquids: Theory, Properties, New Approaches*, (Ed.: A. Kokorin) InTech, Croatia, **2011**; Chapter 29; (b) L. -J. Wang, C. -H. Lin, *Mini-Rev. Org. Chem.*, **2012**, *9*, 223–236.

(15) Y. Yoshida, A. Otsuka, G. Saito, S. Natsume, E. Nishibori, M. Takata, M. Sakata, M. Takahashi, T. Yoko, *Bull. Chem. Soc. Jpn.* **2005**, *78*, 1921-1928; (b) S. Hayashi, H. Hamaguchi, *Chem. Lett.* **2004**, *33*, 1590–1591.

(16) J. -Y. Kim, J. -T. Kim, E. -A. Song, Y. -K. Min, H. Hamaguchi, *Macromelecules* **2008**, *41*, 2886–2889.

(17) (a) P. Nockemann, B. Thijs, N. Postelmans, K. Van Hecke, L. Van Meervelt, K. Binnemans, *J.*

Am. Chem. Soc **2006**, *128*, 13658–13589; (b) B. Mallick, B. Balke, C. Felser, A. -V. Mudring, *Angew. Chem. Int. Ed.* **2008**, *47*, 7635–7638.

(18) (a) R. J. C. Brown, T. Welton, P. J. Dyson, D. J. Ellis, *Chem. Commun.* **2001**, 1862–1863; (b) F. G. Deng, B. Hu, W. Sun, J. Chen, C. G. Xia, *Dalton Trans.* **2007**, 4262–4267; (c) J. E. Dengler, A. Doroodian, B. Rieger, *J. Organomet. Chem.* **2011**, *696*, 3831–3835.

(19) A. Branco, L. C. Branco, F. Pina, *Chem. Commun.* **2011**, 2300–2302.

(20) N. Aoyagi, K. Shimojo, N. R. Brooks, R. Nagaishi, H. Naganawa, K. Van Hecke, L. Van Meervert, K. Binnemans, T. Kimura, *Chem. Commun.* **2011**, *47*, 4490–4492.

(21) P. Zhang, Y. Gong, Y. Lv, Y. Guo, Y. Wang, C. Wang, H. Li, *Chem. Commun.* **2012**, *48*, 2334–2336.

CHAPTER 2

Vapochromic Ionic Liquids Containing Cationic Metal-Chelate Complexes

2.1 Introduction

The salts of chelate complexes with diamine and diketonate ligands, [M(acac)(Me_4en)]X (M = Cu, Ni; acac = acetylacetonate; Me_4en = *N*,*N*,*N*′,*N*′-tetramethylethylenediamine; X = BPh_4, ClO_4, etc.), are well known solvatochromic compounds.[1] They have different colors in crystalline and dissolved states. The color of the solution depends on the donor ability (donor number, *DN*) of the solvent. Indeed, the solvatochromism of such metal complexes or dyes dissolved in an IL is used to evaluate the IL's polarity.[2] In these complexes, the coordination of two solvent molecules changes the structure of the cation from square planar to octahedral, (Scheme 1), and this results in the color changes via changes in the *d*–*d* transition energy. For Ni^{II} complexes, the structural change accompanies a change from diamagnetic to paramagnetic, whereas both structures of the Cu^{II} complexes are paramagnetic. In addition, the solutions of the Ni^{II} complexes in alcohol or acetone also exhibit thermochromism.[1a] We expected these metal complexes would exhibit changes of physical properties in response to vapors of solvents or gases when used as the cations of an IL. Although many functional IL have been reported to date, pure IL that exhibit color changes are limited, such as those exhibiting luminescence change by exposure to amine vapors,[3] and thermochromic IL containing a uranyl complex.[4]

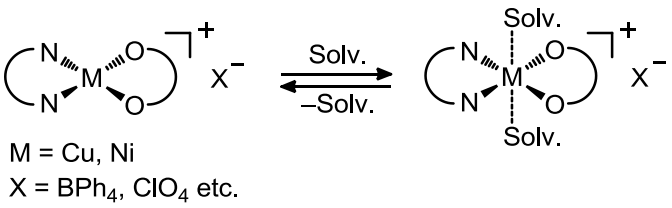

Scheme 1. Coordination changes in solvatochromic complexes [M(acac)(Me_4en)]X.

In this study, IL of cationic chelate complexes with diamine and diketonate ligands were developed (Scheme 2), namely [Cu(acac)(BuMe$_3$en)][Tf$_2$N] (**1a**), [Cu(Bu-acac)(BuMe$_3$en)][Tf$_2$N] (**1b**), [Cu(C$_{12}$-acac)(Me$_4$en)][Tf$_2$N] (**1c**), [Cu(acac)(Me$_4$en)][Tf$_2$N] (**1d**), and [Ni(acac)(BuMe$_3$en)][Tf$_2$N] (**2a**) (Bu-acac = 3-*n*-butyl-2,4-pentanedionate, C$_{12}$-acac = 3-dodecyl-2,4-pentanedionate, BuMe$_3$en = *N*-butyl-*N*,*N*′,*N*′-trimethylethylenediamine, and Tf$_2$N = bis(trifluoromethanesulfonyl)imide).[5] Recently, solid materials that exhibit color changes by vapor- or gas-absorption have attracted much attention.[6–8] The materials prepared in this study are liquid materials that exhibit reversible changes in color, thermal properties, and magnetic properties by the absorption and desorption of organic vapors and gases.

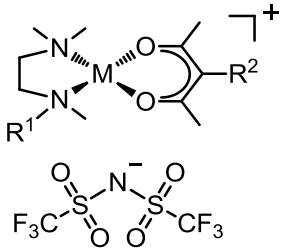

	M	R^1	R^2
1a	Cu	^{n}Bu	H
1b	Cu	^{n}Bu	^{n}Bu
1c	Cu	Me	$C_{12}H_{25}$
1d	Cu	Me	H
2a	Ni	^{n}Bu	H

Scheme 2. Structural formulae of the vapochromic IL.

2.2 Results and Discussion

Preparation, Melting Points, and Colors of the IL. The Cu^{II}- and Ni^{II}-containing IL shown in Scheme 2 were synthesized by the reaction of a nitrate salt of copper or nickel with the diamine and diketonate ligands in ethanol, followed by anion exchange using lithium bis(trifluoromethanesulfonyl)imide. The melting points (T_m), melting entropies (ΔS_m), and glass transition temperatures (T_g) of these salts as determined by differential scanning calorimetry (DSC) analysis are listed in Table 1. [**1a**][Tf$_2$N] was a dark purple liquid, which did not crystallize upon cooling and exhibited a glass transition at T_g = −49 °C. [**1b**][Tf$_2$N] was obtained as a liquid, which crystallized to form a solid (T_m = 59.6 °C) after standing for a few days. This salt also exhibited a

glass transition (T_g = –39.5 °C) when cooled from the liquid state. Both [**1c**][Tf_2N] and [**1d**][Tf_2N] were obtained as dark purple solids, whose melting points were T_m = 41.4 °C and 94.7 °C, respectively. The high melting point of the latter compound is ascribed to the lack of the alkyl chain in the cation. The Ni^{II}-containing IL [**2a**][Tf_2N] was a dark red liquid, which showed only a glass transition upon cooling (T_g = −58 °C). The Cu^{II}-containing salts were stable under air, whereas the Ni^{II}-containing salt was less stable. They were all soluble in polar organic solvents such as diethyl ether, dichloromethane, alcohols and acetone, and insoluble in water and hexane.

Table 1. Melting points (T_m), melting entropies (ΔS_m), and glass transition temperatures (T_g) of [**1a**][Tf_2N], [**1b**][Tf_2N], [**1c**][Tf_2N], [**1d**][Tf_2N], and [**2a**][Tf_2N]. Values after absorption of DMSO are also shown for [**1a**][Tf_2N] and [**1b**][Tf_2N].

	T_m (°C)	ΔH_m (kJ mol^{-1})	ΔS_m (J K^{-1} mol^{-1})	T_g (°C)
[**1a**][Tf_2N]				–49
[**1a**(dmso)][Tf_2N]	24.4	32.5	105.7	–70
[**1a**$(dmso)_2$][Tf_2N]	18.1	31.0	102.7	–78
[**1a**$(dmso)_2$][Tf_2N]·2(DMSO)	5.6	27.8	95.6	–91
	–30.3[a]	8.4[a]	33.3[a]	–128[a]
[**1b**][Tf_2N]	59.6	38.3	114.5	–40
[**1b**(dmso)][Tf_2N]				–58
[**1b**$(dmso)_2$][Tf_2N]				–67
[**1b**$(dmso)_2$][Tf_2N]·2(DMSO)				–78
				–126[a]
[**1c**][Tf_2N]	41.4	31.2	98.4	–49
[**1d**][Tf_2N]	94.7	22.9	62.0	
[**2a**][Tf_2N]				–58
[**2a**][Tf_2N]·2(MeOH)				–72
DMSO	18.5[b]	14.4[b]	49.3[b]	

[a]DMSO fraction, [b]From reference 9.

The color of the Cu^{II} containing complexes was mostly deep purple in both the solid and liquid states. The color suggests that the Tf_2N anions are very weakly coordinated to the metal center of the cation. Indeed, the *d–d* transition energies in the crystals of [Cu(acac)(Me_4en)]X depend on the interaction between the metal center and the anion,[10] and are lower for anions, which coordinate more strongly. For example, the *d–d* transitions (λ_{max}) of [Cu(acac)(Me_4en)][BPh_4] and

[Cu(acac)(Me_4en)][ClO_4] in the solid state appear at 500 nm[11] and 553 nm[12] respectively. The *d–d* transition energy in [**1a**][Tf_2N] (λ_{max} = 551 nm) was close to that in the latter complex, which reflects that Tf_2N anion (*DN* = 5.4[13]) is more weakly coordinating than ClO_4 (*DN* = 8.4), resulting in a deeper purple color. The liquid [**1c**][Tf_2N] was, however, an exception. This salt has a long alkyl chain in the cation and exhibited a reversible color change between a dark purple solid and a brown liquid at T_m = 41.4 °C (Figure 1). The *d–d* transition in the liquid state occurs at λ_{max} =536 nm, which suggests that the anion do not interact with the metal center. This is probably due to the excluded volume effect of the alkyl chain in the liquid state, which disappears in the solid state.

Color Changes in Cu^{II}-containing IL by Vapor Absorption. The liquid [**1a**][Tf_2N] exhibited color changes on absorption of various organic vapors. The photographs of [**1a**][Tf_2N] before and after the absorption of two equimolar amounts of vapors are shown in Figure 2 (upper). [**1a**][Tf_2N] was a purple liquid, which turned blue-purple when exposed to the vapor of acetonitrile or acetone, blue under the vapor of methanol, DMF, or DMSO, and green under the vapor of pyridine. The vapor absorption and color change occurred from the surface of the liquids, followed by gradual diffusion. The color change was fully reversible; the vapor molecules desorbed when the liquids were left under air, accompanied by recovery of the original color. The IL exhibited no response towards moisture despite of the comparable *DN* values of water and methanol. This is probably due to the hydrophobicity of the liquid. Films of an ion gel could be formed by addition of a gelator, PVdF(HFP),[14] to [**1a**][Tf_2N], which also responded to organic vapors (Figure 3).

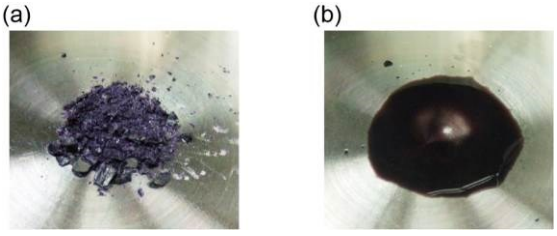

Figure 1. Photographs of [**1c**][Tf_2N] (a) in the solid state (20 °C), and (b) in the liquid state (60 °C).

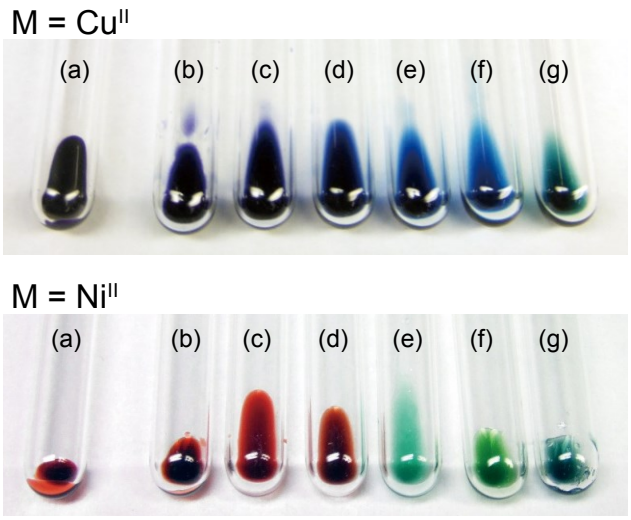

Figure 2. Photographs of [**1a**][Tf_2N] (upper) and [**2a**][Tf_2N] (lower), (a) before exposure to vapor, and after absorption of two equimolar amounts of (b) acetonitrile, (c) acetone, (d) methanol, (e) DMF, (f) DMSO, and (g) pyridine.

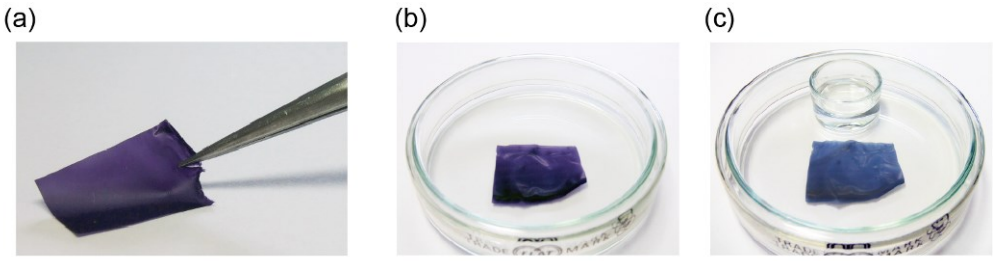

Figure 3. (a) Photograph of [**1a**][Tf_2N]–PVdF(HFP) gel films (50wt%). Figures (b) and (c) are photographs of the film before and after exposure to methanol vapor, respectively.

The UV-vis spectra of [**1a**][Tf_2N] before and after absorption of various vapors are shown in Figure 4. The *d–d* transition (λ_{max}) of pure [**1a**][Tf_2N] appeared at 551 nm, whereas the peak shifts to longer wavelengths after vapor absorption, varying from 573 nm under acetonitrile to 625 nm under pyridine. The *d–d* transition energies were lower for the vapor molecules with higher *DN* values (Table 2). There was a linear correlation between the *d–d* transition energies and the *DN* values (Figure 5). The *d–d* transition energies were comparable to [Cu(acac)(Me_4en)][ClO_4] dissolved in the corresponding solvents.[11]

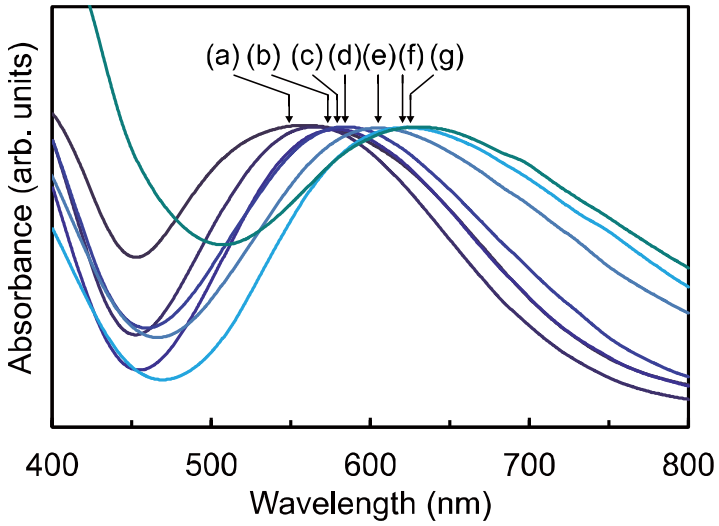

Figure 4. UV-vis absorption spectra of [**1a**][Tf_2N], (a) before, and after absorption of two equimolar amounts of (b) acetonitrile, (c) acetone, (d) methanol, (e) DMF, (f) DMSO, and (g) pyridine. The arrows indicate the absorption maxima of the *d–d* transition of each sample.

Table 2. Absorption maxima and colors of liquid samples of [**1a**(solvent)$_2$][Tf_2N]. Donor numbers (*DN*) of the solvent molecules are also shown.

Solvent	λ_{max} (nm)	Color	*DN*[a]
Acetonitrile	573	purple	14.1
Acetone	579	blue-purple	17.0
Methanol	584	dark blue	19.0
DMF	605	blue	26.6
DMSO	620	blue	29.8
Pyridine	625	dark green	33.1

[a]From reference 15.

The time needed to absorb two equimolar amounts of vapor molecules depended on the vapor pressure of the solvents, varying from a few seconds for acetone to half a day for DMSO at saturation. The vapor adsorption of [**1a**][Tf_2N] under a saturated vapor pressure of DMSO was monitored over time (Figure 6). The absorption occurred at a constant rate until two equimolar amounts of DMSO were absorbed. An IL with a six-coordinated cation was fully formed at this point, which further absorbed DMSO at a slower rate to form a mixture of the IL and free DMSO, as revealed by thermal measurements (*vide infra*).

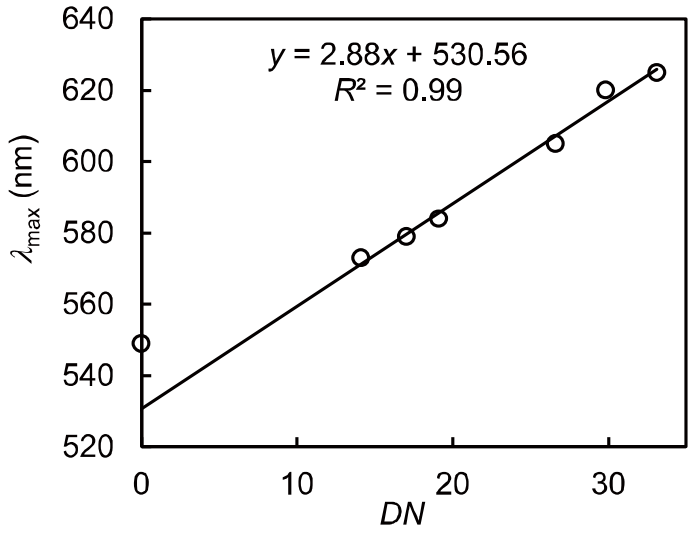

Figure 5. Correlation between λ_{max} of [**1a**(solvent)$_2$][Tf_2N] and the *DN* of the solvent molecules.

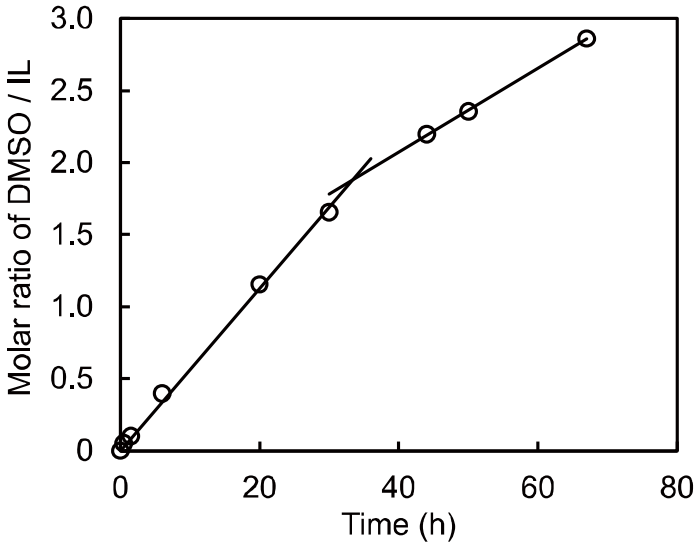

Figure 6. Molar ratio of DMSO absorbed in [**1a**][Tf_2N] under saturated DMSO vapor pressure, plotted against exposure time.

Color Changes in Cu^{II}-containing IL by Gas Absorption. The gas absorption ability of [**1a**][Tf_2N] was investigated. Exposure of [**1a**][Tf_2N] to ammonia gas (1 atm) caused a color change from dark purple to green within a few seconds, and returned to the original color when the IL was left under air or purging with nitrogen gas. The absorption spectra and photographs of the liquid,

before and after the absorption of ammonia, are shown in Figure 7. The absorption maximum of the *d–d* transition shifted from 551 nm to 642 nm on exposure to ammonia. [**1a**][Tf_2N] also responded to the gases of NO, NO_2, and SO_2, but they caused decomposition of the salt, resulting in irreversible color changes. No change was observed on exposure to dimethyl sulfide, carbon monoxide, and formaldehyde. The lack of the coordination ability of dimethyl sulfide and carbon monoxide may be ascribed to the softness of their donor atoms under the HSAB theory.[16]

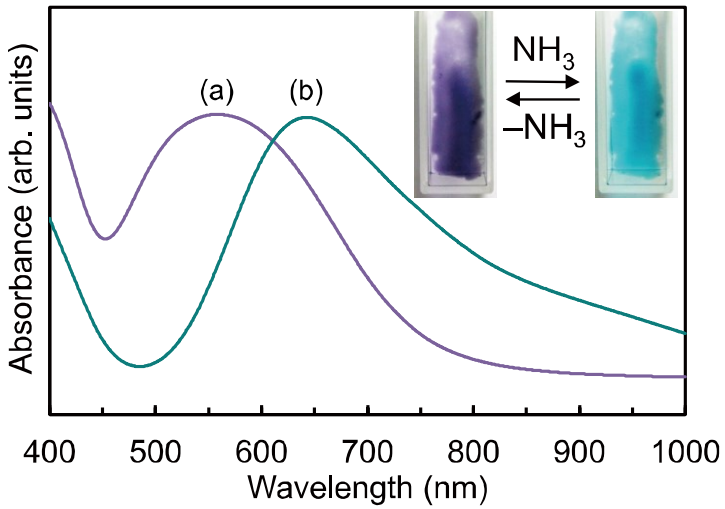

Figure 7. UV-vis absorption spectra of [**1a**][Tf_2N], (a) before and (b) after exposure to an ammonia gas. The inset shows photographs of the liquids.

Thermal Property Changes in Cu^{II}-containing IL by Vapor Absorption. The thermal properties of [**1a**][Tf_2N] and [**1b**][Tf_2N] before and after absorption of DMSO vapor were investigated. Thermal data obtained by DSC analyses are included in Table 1. In these salts, the phase can be controlled by vapor absorption; transformation from liquid to solid was possible for [**1a**][Tf_2N], and a reverse change was possible for [**1b**][Tf_2N]. The values of T_m/T_g were in good agreement with the empirical rule ($T_g/T_m = 2/3$)[17] in all cases.

DSC traces of [**1a**][Tf_2N] containing 0–4 equimolar amounts of DMSO are shown in Figure 8. Pure [**1a**][Tf_2N] showed only a glass transition on both the cooling and heating runs (T_g = –48.8 °C). [**1a**(dmso)$_n$][Tf_2N] also exhibited glass transitions upon cooling at –69.8 °C (n = 1) and –77.8 °C (n = 2), whereas they crystallized in the heating run at –27.8 °C (n = 1) and –28.6 °C (n = 2), and then melted at 24.4 °C (n = 1) and 18.1 °C (n = 2). Thus, a liquid-solid phase transformation was possible by vapor absorption in a certain temperature range (Figure 9). This phase behavior change is probably correlated with the change in viscosity (*vide infra*). Namely, IL with high viscosities undergo glass transitions at low temperatures, whereas a reduction in the viscosity enables crystallization.[18] The melting entropies of [**1a**(dmso)$_n$][Tf_2N] (n = 1 and 2) were comparable (~ 10^2 J K^{-1} mol^{-1}), which suggests that the coordinated dmso do not dissociated in the liquid state.

In the DSC curve of a sample containing four equimolar amounts of DMSO, the glass transition and melting of the excess DMSO were observed at –127.7 °C and –30.3 °C, respectively, together with those of [**1a**(dmso)$_2$][Tf_2N]. This observation indicates that the liquid was a mixture of [**1a**(dmso)$_2$][Tf_2N] and two equimolar amounts of free DMSO. The melting entropies of each component were in agreement with the values for the pure compounds. The lower glass transition temperatures and melting points are due to the coexistence of the two components.

When solid [**1b**][Tf_2N] (T_m = 59.6 °C) was exposed to the vapor of DMSO, it gradually turned into a liquid from the surfaces (Figure 9). The liquids of [**1b**(dmso)$_n$][Tf_2N] (n = 1, 2) thus formed showed glass transitions at low temperature (T_g = –57.8 °C for n = 1, –67.2 °C for n = 2). In the liquid that contains four equimolar amounts of DMSO, the glass transition of the excess DMSO (T_g = –125.9 °C) as well as that of the dmso-coordinated species (T_g = –78.1 °C) was observed, similar to [**1a**][Tf_2N] as shown above. This result again indicates that liquids containing more than two equimolar amounts of solvent molecules are the mixtures of the IL component and free solvent molecules.

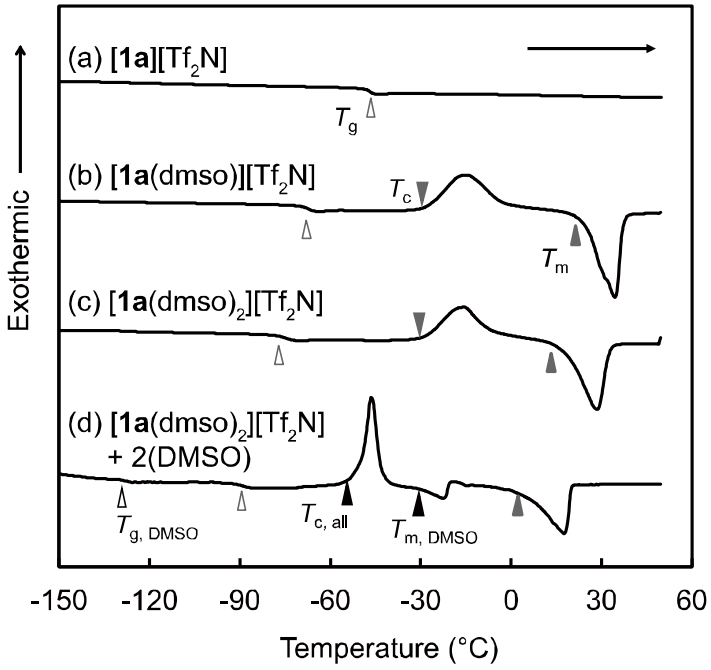

Figure 8. DSC traces of [**1a**][Tf_2N] (a) before, and after absorption of (b) 1.0, (c) 2.0, and (d) 4.0 equimolar amounts of DMSO, recorded on the heating runs.

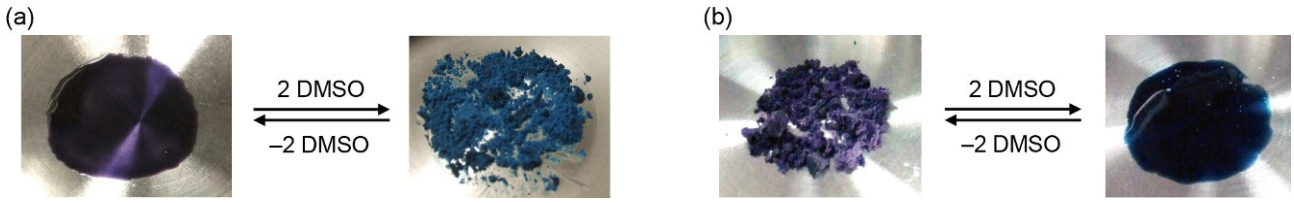

Figure 9. Photographs of (a) [**1a**][Tf_2N] at 0°C, and (b) [**1b**][Tf_2N] at 25°C, before and after the absorption of two equimolar amounts of DMSO.

Viscosities Changes in Cu^{II}-containing IL by Vapor Absorption. The temperature dependence of the viscosities of [**1a**][Tf_2N] and [**1a**(dmso)$_n$][Tf_2N] (n = 1, 2) were measured (Figure 10). The viscosities and relevant parameters of these liquids are listed in Table 3. The viscosity of [**1a**][Tf_2N] at 25 °C was 1188 mPa s, indicating that the IL was more viscous than comparable alkylimidazolium IL (e.g., 49 mPa s for [1-butyl-3-methylimidazolium][Tf_2N][19]). However, the viscosity decreased dramatically after the absorption of DMSO vapor; the viscosities of [**1a**(dmso)$_n$][Tf_2N] at 25 °C were 191.3 mPa s (n = 1) and 119.5 mPa s (n = 2). The activation energies (E_a) derived from the Arrhenius

approximation of the temperature dependence were comparable or slightly larger than those of the imidazolium IL[19] (E_a = 30–40 kJ mol^{-1}), and these values increased after vapor absorption (Table 3). The temperature dependence was also fitted using a Vogel-Fulcher-Tammann (VFT) approximation ($\eta = \eta_0 \exp[DT_0/(T-T_0)]$)[20], where T_0 and D are the ideal glass transition temperature and the degree of deviation from Arrhenius behavior, respectively. Thus, absorption of DMSO resulted in a decrease in the D value, which corresponds to the increase in the fragility of the liquid.

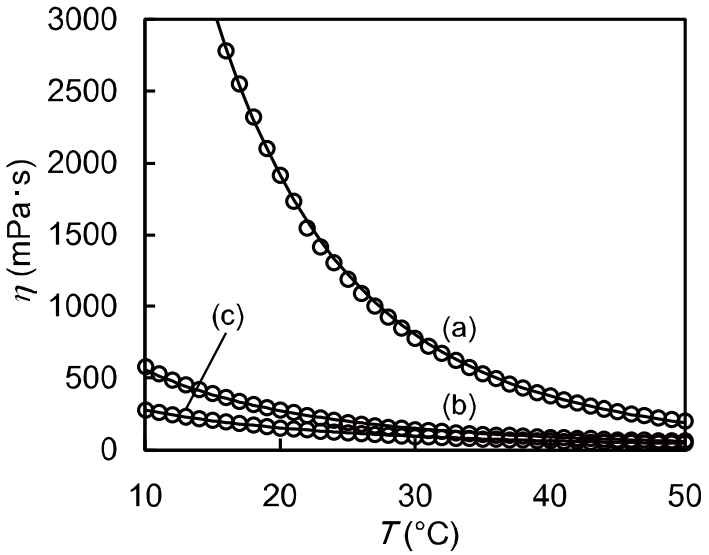

Figure 10. Temperature dependence of the viscosities of; (a) [**1a**][Tf_2N], (b) [**1a**(dmso)][Tf_2N], and (c) [**1a**$(dmso)_2$][Tf_2N]. Solid lines are the fitting curves by the VFT equation.

Table 3. Viscosities, activation energies, and D values of [**1a**$(dmso)_n$][Tf_2N] (n = 0, 1, and 2).

	$\eta_{25\,°C}$ (mPa s)	E_a (kJ mol^{-1})	D
[**1a**][Tf_2N]	1188	8.5	19.8
[**1a**(dmso)][Tf_2N]	191.3	44.7	4.6
[**1a**$(dmso)_2$][Tf_2N]	119.5	35.8	2.9

Color Changes in Ni^{II}-containing IL by Vapor Absorption. [**2a**][Tf_2N] was a dark reddish liquid, which turned green after absorbing organic vapors with high *DN* such as DMF, DMSO, and pyridine. The color was unchanged when exposed to organic vapors with low *DN* values such as acetonitrile, acetone, and methanol (Figure 2, lower). Unlike the Cu^{II}-containing liquids, the different equilibrium ratios of the four-, five-, and six-coordinated species cause the color variation. This is because the coordination geometry change of Ni complexes is accompanied by a change in the spin state.[1c]

The UV-vis absorption spectra of [**2a**][Tf_2N] before and after absorption of two equimolar amounts of DMSO or methanol were measured (Figure 11). In [**2a**][Tf_2N], the *d–d* transition characteristic of the square planar complex[19] was observed at 490 nm. After the absorption of DMSO, this peak disappeared and new peaks, which are characteristic of the octahedral complex,[21] appeared at 638 nm and 1067 nm, indicating the formation of [**2a**$(dmso)_2$][Tf_2N]. After the absorption of methanol, which has much lower *DN*, the square planar complex (λ_{max} = 491 nm) was still the dominant compound, together with a weak peak of the octahedral species (λ_{max} = 1038 nm). This indicates that most of the methanol molecules are not coordinated to the cation but are present as solvent, which is consistent with the absence of color change on absorption of methanol. Interestingly, the methanol absorbed liquid showed thermochromism, turning from red at RT to yellowish green at –80 °C. In the temperature dependent UV-Vis absorption spectra (Figure 12), a reduction in the peak intensity of the four-coordinated species (λ_{max} = 490 nm) was observed at low temperature, from which the ratios of the four-coordinated species at 20 °C and –80 °C were estimated to be 71% and 32%, respectively. Thus, the thermochromism is associated with the coordination of methanol to the metal center at low temperatures, which results in an increase in the IL component [**2a**$(MeOH)_2$][Tf_2N]. This temperature-dependent composition change was also confirmed by the magnetic measurements shown below.

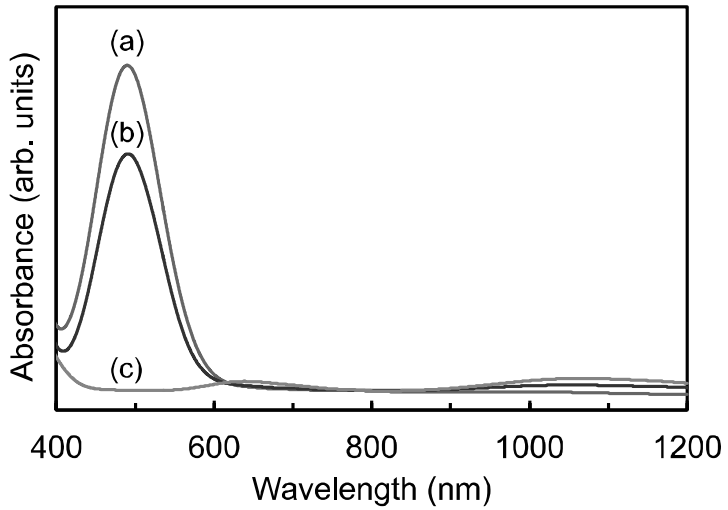

Figure 11. UV-vis absorption spectra of [**2a**][Tf_2N] (a) before, and after absorption of two equimolar amounts of (b) methanol, and (c) DMSO.

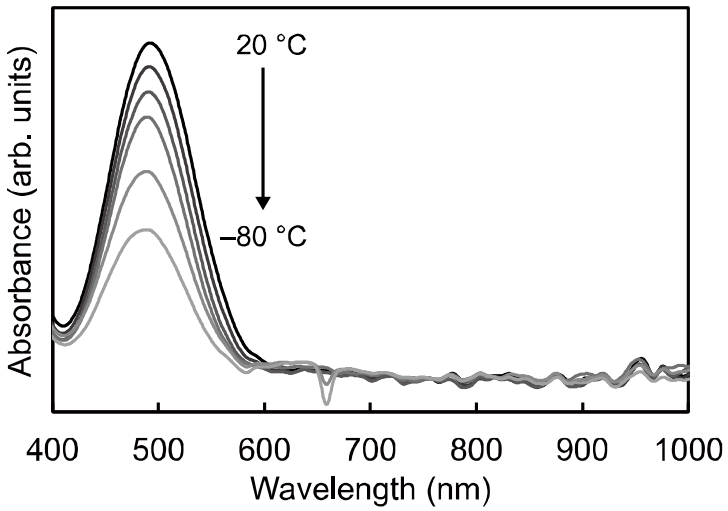

Figure 12. UV-vis absorption spectra of [**2a**][Tf_2N] after absorbing two equimolar amounts of methanol, recorded between 20 °C and –80 °C at 20 K intervals.

Magnetic Properties of Ni^{II}-containing IL. The magnetic susceptibility of [**2a**][Tf_2N] before and after the absorption of organic vapors was investigated, which demonstrated that the magnetic properties of the IL can be controlled by vapor absorption. The χT values of [**2a**][Tf_2N] and [**2a**$(dmso)_2$][Tf_2N] at 300 K were 0.07 emu K mol^{-1} and 0.97 emu K mol^{-1}, respectively. This change is consistent with a structural change from the diamagnetic square planar cation to the paramagnetic octahedral cation ($S = 1$).

The composition of the liquid after absorbing an equimolar amount of DMSO was estimated based on the magnetic susceptibility. The χT value of this sample at 300 K was 0.68 emu K mol^{-1}, which does not agree with the value expected for a five-coordinated complex (0.97 emu K mol^{-1}, the same as for a six-coordinated complex) nor a 1:1 mixture of the four- and six-coordinated complexes (0.45 emu K mol^{-1}). This result is, however, consistent with an equilibrium between the four-, five-, and six-coordinated complexes in the liquid, as seen in earlier results.[1c] Based on the amount of the absorbed DMSO and the resultant χT value, the ratio of these three species at 300 K was estimated to be 0.31:0.38:0.31. In the UV-Vis absorption spectra, the absorption intensity of the four-coordinated species decreased by about 80% after absorbing an equimolar amount of DMSO (Figure 13), which agrees with the magnetic measurements within experimental error.

The temperature dependence of the magnetic susceptibilities of [**2a**][Tf_2N] before and after absorption of one and two equimolar amounts of DMSO is shown in Figure 14. These samples showed simple paramagnetic behavior over the temperature range 2–300 K. For the sample containing an equimolar amount of DMSO, a very slight increase in the χT value was observed between 300 K and 215 K as the temperature decreased. This probably reflects a slight shift of the equilibrium toward the five-coordinated species due to an entropy gain. The χT value was constant below the glass transition temperature (T_g = 215 K), which has been ascribed to the freezing of the equilibrium. A slight increase was also observed in pure [**2a**][Tf_2N] with decreasing temperature, which possibly originates from increased cation-anion interactions.

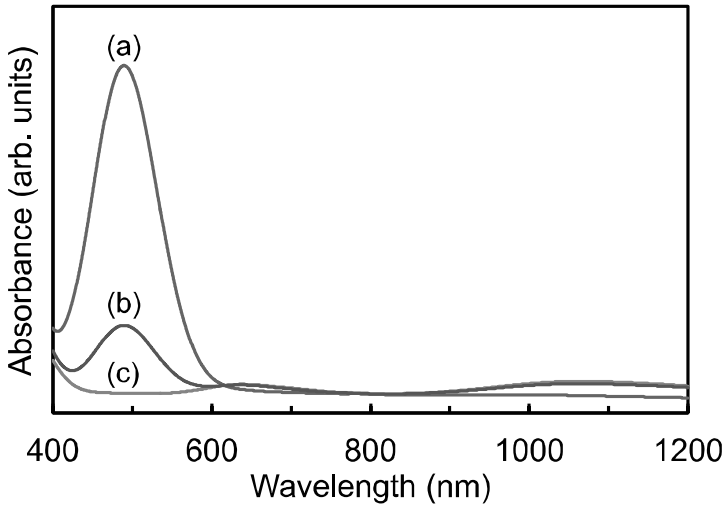

Figure 13. UV-vis absorption spectra of (a) [**2a**][Tf_2N], (b) [**2a**][Tf_2N] with one equimolar amount of DMSO, and (c) [**2a**][Tf_2N] with two equimolar amounts of DMSO.

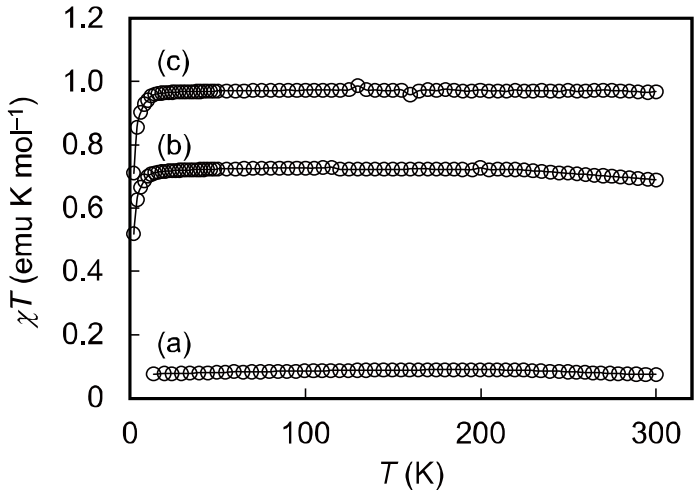

Figure 14. Temperature dependence of the magnetic susceptibilities of (a) [**2a**][Tf_2N], (b) [**2a**][Tf_2N] with an equimolar amount of DMSO, and (c) [**2a**][Tf_2N] with two equimolar amounts of DMSO.

As shown in the previous section, [**2a**][Tf_2N] that has absorbed methanol exhibits thermochromism, indicating an increase in the proportion of five- or six-coordinated paramagnetic species at lower temperatures. A consistent change was observed in the magnetic susceptibility. The temperature dependences of the magnetic susceptibility of [**2a**][Tf_2N]·*n*MeOH (*n* = 2.3 and 0.7) are shown in Figure 15. For the sample with *n* = 2.3, the χT value was 0.30 emu K mol^{-1} at 300 K, which increased upon cooling to reach 0.60 emu K mol^{-1} at 180 K. From these values, the ratios of the four-coordinated species at 300 K and 180 K were calculated to be 75% and 41%, respectively. The ratio at room temperature is consistent with the absorption spectrum of the liquid as shown above. The χT value was temperature independent below 180 K, which is ascribed to the freezing of the equilibrium below the glass transition temperature. For the sample with *n* = 0.7 (Figure 15b), the χT values at 300 K and 180 K were 0.08 emu K mol^{-1} and 0.29 emu K mol^{-1}, respectively. The ratios of the four-coordinated species at respective temperatures were estimated to be 98% and 76%. The χT value was temperature independent below 195 K.

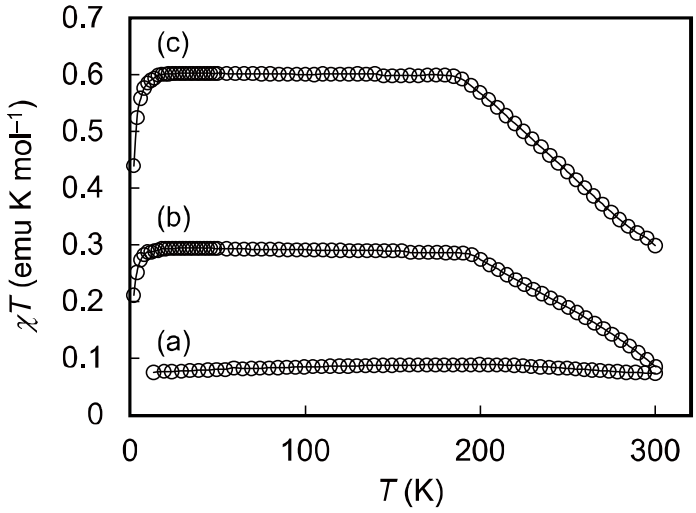

Figure 15. Temperature dependence of the magnetic susceptibilities of; a) [**2a**][Tf_2N], b) [**2a**][Tf_2N] with 0.7 equimolar amount of methanol, and c) [**2a**][Tf_2N] with 2.3 equimolar amounts of methanol.

2.3 Conclusion

Metal containing IL were developed that exhibit reversible changes in color, thermal properties, viscosities, and magnetic properties in response to organic vapors or gases. These IL exhibit color changes that reflect the coordination ability, or donor number, of the vapor molecules. The vapor absorption also leads to changes in the phase behavior. The Ni^{II}-containing IL exhibits a conversion between the paramagnetic and diamagnetic states by vapor absorption/desorption. After methanol absorption, the Ni^{II}-containing IL exhibits thermochromism and temperature dependent magnetism. These functions were accomplished by using the solvatochromic metal complexes as the cation of IL, and it is worth mentioning that the liquids are not only vapochromic but also have the advantageous features of IL, such as low volatility and ionic conductivity. Recently, solid materials that exhibit color changes by vapor- or gas-absorption have attracted much attention In contrast to solids, the liquid materials developed here are paintable and also immobilized as films, and will lead to novel applications, such as liquid vapor sensors, controlled-release material, and gas separation films.

2.4 Experimental Section

General. *N*-butyl-*N*,*N*′,*N*′-trimethylethylenediamine ($BuMe_3en$)[22] and 3-dodecyl-2,4-pentane dione (C_{12}-acacH)[23] were prepared according to literature. Other chemicals were purchased from commercial sources. Elemental analyses were performed with a Yanaco CHN coder MT5. ESI-MS spectra were recorded on a Thermo Fisher Scientific LTQ-Orbitrap Discovery. UV-vis absorption spectra were recorded on a JASCO V-570 UV/VIS/NIR spectrometer, using a quartz cell, where a thin layer of the IL was placed on one side. Variable temperature absorption spectra were recorded on an Ocean Optics HR2000CG-UV-NIR spectrometer with a Linkam LTS350 hot stage from –80 °C to 20 °C. DSC measurements were performed using a TA Instruments Q100 differential scanning calorimeter over the temperature range 110–380 K at a rate of 10 K min^{-1}. Viscosities were measured by using a Toki Sangyo TV-22 viscometer with a 3° × R7.7 cone rotor from –15 °C to 60 °C.

Magnetic susceptibilities were measured using a Quantum Design MPMS-XL7 SQUID susceptometer over the temperature range 2–300 K under a magnetic field of 0.1 T. An aluminum pan or a sealed NMR tube was used for liquid samples.

[Cu(acac)(BuMe$_3$en)][Tf$_2$N] ([1a][Tf$_2$N]). Acetylacetone (0.10 mL, 1.0 mmol), sodium carbonate (53 mg, 0.5 mmol), and BuMe$_3$en (0.19 mL, 1.0 mmol) were added to a solution of Cu(NO$_3$)·3H$_2$O (242 mg, 1.0 mmol) in ethanol (10 mL) with stirring. After stirring for 30 min, the solution was filtered to remove the unreacted sodium carbonate and precipitated sodium nitrate. Lithium bis(trifluoromethanesulfonyl)imide (430 mg, 1.5 mmol) was added to the filtrate and stirred for a further 30 min. After evaporation, dichloromethane (20 mL) was added to the residue, and the solution was washed with water (25 mL × 3). The organic layer was dried over magnesium sulfate, and evaporation of the solvent gave the desired product as a dark purple liquid, which was dried under vacuum at 70 °C for 24 h. 83% yield. Anal. Calcd. for $C_{16}H_{29}CuF_6N_3O_6S_2$ (601.08): C, 31.97; H, 4.86; N, 6.99. Found: C, 32.03; H, 4.89 N, 7.24. ESI-MS. calcd. for [Cu(acac)(BuMe$_3$en)]$^+$: 320.1525. Found: 320.1526.

[Cu(Bu-acac)(BuMe$_3$en)][Tf$_2$N] ([1b][Tf$_2$N]). This salt was prepared by the same method as [**1a**][Tf$_2$N] except that 3-butyl-2,4-pentanedione (Bu-acacH) was used instead of acetylacetone. The product was obtained as a dark purple supercooled liquid, which crystallized after standing for a few days. 78% yield. Anal. Calcd. for $C_{20}H_{37}CuF_6N_3O_6S_2$ (657.19): C, 36.55; H, 5.67; N, 6.39. Found: C, 36.41; H, 5.67; N, 6.45. ESI-MS. calcd. for [Cu(Bu-acac)(BuMe$_3$en)]$^+$: 278.1056. Found: 278.1049.

[Cu(C$_{12}$-acac)(Me$_4$en)][Tf$_2$N] ([1c][Tf$_2$N]). This salt was prepared by the same method for [**1a**][Tf$_2$N] except that 3-dodecyl-2,4-pentanedione (C$_{12}$-acacH) and tetramethylethylenediamine (Me$_4$en) were used instead of acetylacetone and BuMe$_3$en. Dark purple solid, 38% yield. Anal. Calcd. for $C_{25}H_{47}CuF_6N_3O_6S_2$ (727.33): C, 41.28; H, 6.51; N, 5.78. Found: C, 41.30; H, 6.55; N, 5.79.

[Cu(acac)(Me$_4$en)][Tf$_2$N] ([1d][Tf$_2$N]). This salt was prepared by the same method as [**1a**] [Tf$_2$N] except that tetramethylethylenediamine (Me$_4$en) was used instead of BuMe$_3$en. Dark purple

solid, 81% yield. Anal. Calcd. for $C_{13}H_{23}CuF_6N_3O_6S_2$ (559.00): C, 27.93; H, 4.15; N, 7.52. Found: C, 28.17; H, 4.23; N, 7.56. ESI-MS. calcd. for $[Cu(acac)(Me_4en)]^+$: 278.1056. Found: 278.1049.

[Ni(acac)(BuMe$_3$en)][Tf$_2$N] ([2a][Tf$_2$N]). This salt was prepared by the same method as [**1a**][Tf_2N], except that $Ni(NO_3)\cdot 6H_2O$ was used as the metal source and the crude product was dissolved in diethyl ether instead of dichloromethane during the workup procedure. Dark red liquid, 95% yield. Anal. Calcd. for $C_{16}H_{29}NiF_6N_3O_6S_2$ (596.23): C, 32.23; H, 4.90; N, 7.05. Found: C, 31.63; H, 5.07 N, 7.32. ESI-MS. calcd. for $[Ni(acac)(BuMe_3en)]^+$: 315.1582. Found: 315.1573.

Preparation of polymer gels of [1a][Tf$_2$N]. A solution of poly(vinylidene fluoride-co-hexafluoropropene) [= PVdF(HFP)] (200 mg) in acetone (20 mL) was added to [**1a**][Tf_2N] (200 mg, 0.33 mmol) and stirred for a few minutes. The mixture was poured into a petri dish and left to dry at room temperature. A purple film containing 50wt% of the polymer (thickness: 0.07 mm) was obtained. A film containing 20wt% of the polymer (thickness: 0.10 mm) was prepared by the same method.

Examination of vapor/gas absorption properties. For vapor absorption experiments, a small glass vial containing the IL (30–50 mg) was placed in a sealed glass bottle that was filled with the vapor of an organic solvent at room temperature. Acetonitrile, acetone, methanol, DMF, DMSO, pyridine, and Me_2S were used as the organic solvent. After exposure to the vapor, the resulting liquid was mixed until uniform. The rate of vapor absorption was determined by weighing the samples. Samples for the magnetic measurement and the viscosity measurement were prepared by adding a desired amount of solvent to the IL. For gas absorption experiments, [**1a**][Tf_2N] was painted on the inner wall of a quartz cell, which was capped with a septum. After purging the cell with nitrogen gas through a needle, gases (1 atm) of NH_3, NO, NO_2, SO_2, CO, and formaldehyde were introduced into the cell. NH_3 was prepared by the reaction of ammonium chloride and 2M NaOH aqueous solution, SO_2 by the reaction of $NaHSO_3$ and diluted sulfuric acid, and formaldehyde by heating of paraformaldehyde at 70–120 °C. Other gases were purchased from commercial sources.

References

(1) (a) Y. Fukuda, K. Sone, *Bull. Chem. Soc. Jpn*. **1970**, *43*, 2282; (b) Y. Fukuda, K. Sone, *Bull. Chem. Soc. Jpn*. **1972**, *45*, 465–469; (c) W Linert, Y. Fukuda, A. Camard, *Coord. Chem. Rev.* **2001**, *218*, 113–152.

(2) (a) M. J. Muldoon, C. M. Gordon, I. R. Dunkin, *J. Chem. Soc., Perkin Trans.* **2001**, *2*, 433–435; (b) J. Bartosil, A. -V. Mudring, *Phys. Chem. Chem. Phys.* **2010**, *12*, 4005–4011; (c) X. Wei, L. Yu, X. Jin, G. Z. Chen, *Green. Chem.* **2008**, *10*, 296–305; (d) X. Wei, L. Yu, X. Jin, D. Wang, G. Z. Chen, *Adv. Mater.* **2009**, *21*, 776–780; (e) K. Takeo, Y. Tone, C. Hennig, S. Inoue, T. Tsubomura, *Inorg. Chem.* **2012**, *51*, 4850–4854; (f) P. De Vreese, N. R. Brooks, K. Van Hecke, L. Van Meervelt, E. Matthijs, K. Binnemans, R. Van Deun, *Inorg. Chem.* **2012**, *51*, 4972–4981.

(3) K. Y. Yung, A. J. Schadock-Hewitt, N. P. Hunter, F. V. Bright, G. A. Baker, *Chem. Commun.* **2011**, *47*, 4775–4777.

(4) N. Aoyagi, K. Shimojo, N. R. Brooks, R. Nagaishi, H. Naganawa, K. Van Hecke, L. Van Meervert, K. Binnemans, T. Kimura, *Chem. Commun.* **2011**, *47*, 4490–4492.

(5) T. Mochida, Y. Funasako, JP. Patent 203806, 2011.

(6) (a) L. G. Beauvais, M. P. Shores, J. R. Long, *J. Am. Chem. Soc.* **2000**, *122*, 2763–2772; (b) M. Ohba, K. Yoneda, G. Agustí, M. C. Muñoz, A. B. Gaspar, J. A. Real, M. Yamasaki, H. Ando, Y. Nakao, S. Sakaki, S. Kitagawa, *Angew. Chem., Int. Ed.* **2009**, *48*, 4767–4771; (c) J. J. Gassensmith, H. Furukawa, R. A. Smaldone, R. S. Forgan, O. M. Yaghi, J. F. Stoddart, *J. Am. Chem. Soc.* **2011**, *133*, 15312–15315.

(7) (a) C. L. Exstrom, J. R. Sowa Jr., C. A. Daws, D. Janzen, K. R. Mann, G. A. Moore, F. F. Stewart, *Chem. Mater.* **1995**, *7*, 15–17; (b) T. J. Wadas, Q. -M. Wang, Y. -j. Kim, C. Flaschenreim, T. N. Blanton, R. Eisenberg, *J. Am. Chem. Soc.* **2004**, *126*, 16841–16849; (c) A. Cingolani, S. Galli, N. Masciocchi, L. Pandolfo, C. Pettinari, A. Sironi, *J. Am. Chem. Soc.* **2005**, *127*, 6144–6145; (d) A. Kobayashi, M. -A. Dosen, M. Chang, K. Nakajima, S. Noro, M. Kato, *J.*

Am. Chem. Soc. **2010**, *132*, 15286–15298.

(8) (a) E. Takahashi, H. Takaya, T. Naota, *Chem. Eur. J.* **2010**, *16*, 4793–4802; (b) K. Fujii, A. Sakon, A. Sekine, H. Uekusa, *Cryst. Growth Des.* **2011**, *11*, 4305–4308.

(9) H. L. Clever, E. F. Jr. Westrum, *J. Phys. Chem.* **1970**, *74*, 1309−1317.

(10) S. Noro, N Yanai, S. Kitagawa, T. Akutagawa, T. Nakamura, *Inorg. Chem.* **2008**, *47*, 7360–7365.

(11) Y. Fukuda, A. Shimura, M. Mukaida, E. Fujita, K. Sone, *J. Inorg. Nucl. Chem.* **1974**, *36*, 1265–1270.

(12) W. Linert, R. F. Jameson, A. Taha, *J. Chem. Soc., Dalton Trans.* **1993**, 3181–3186.

(13) W. Linert, A. Camard, M. Armand, C. Michot, *Coord. Chem. Rev.* **2002**, *226*, 137–141.

(14) (a) J. Fuller, A. C. Breda, R. T. Carlin, *J. Electrochem. Soc.* **1997**, *144*, L67–L70; (b) J. Fuller, A. C. Breda, R. T. Carlin, *J. Electroanal. Chem.* **1998**, *459*, 29–34.

(15) V. Gutmann, *Coord. Chem. Rev.* **1976**, *18*, 225–255.

(16) I. Persson, *Pure Appl. Chem.* **1986**, *58*, 1153–1161.

(17) D. Turnbull, M. H. Cohen, *Modern Aspect of the Vitreous State*, Butterworth, Vol. *1* (Ed.: J. D. Mackenzie), London, **1960**, p 38.

(18) T. Inagaki, T. Mochida, M. Takahashi, C. Kanadani; T. Saito, D. Kuwahara, *Chem. Eur. J.* **2012**, *18*, 6795–6804.

(19) A. Paul, A. J. Samanta, *J. Phys. Chem. B* **2008**, *112*, 16626–16632.

(20) G. S. Fulcher, *J. Am. Ceram. Soc*. **1925**, *8*, 339–355.

(21) Y. Fukuda, K. Sone, *J. Inorg. Nucl. Chem.* **1972**, *34*, 2315–2328.

(22) H. Shirase, M. Saito, M. Arakawa-Itoh, Y. Fukuda, *Bull. Chem. Soc. Jpn.* **2009**, *82*, 230–235.

(23) C. Cativiela, J. L. Serrano, M. M. Zurbano, *J. Org. Chem.* **1995**, *60*, 3074–3083.

CHAPTER 3

Ionic Liquids Containing Cationic Copper Complexes with Tripodal Ligands

3.1 Introduction

Tris(2-dimethylaminoethyl)amine (abbreviated as Me_6tren) and its analogs are highly versatile tripodal ligands[1] that may be used to produce a variety of metal complexes. Among them, [Cu(Me_6tren)]X (X = anion) and related complexes are bioinorganically important complexes, and are the model compounds for the active sites of metalloenzymes.[2] Many five-coordinate complexes [Cu(Me_6tren)L]X (L = halogens, etc.) have been prepared and their structures and properties have been investigated.[3] Copper complexes with tripodal ligands catalyze various chemical reactions.[2d,4] In this study, we aimed to prepare copper-containing ILs with tripodal ligands. Liquefaction of these complexes may lead to functional fluids exhibiting chemical reactivities and catalytic activities. For this purpose, we designed novel ligands bis(2-dimethylaminoethyl)-((1-R-imidazol-2-yl)methyl) amine, where R = hexyl (**L**^{1}), propyl (**L**^{2}), and methyl (**L**^{3}) groups. We introduced the alkylimidazole moiety because alkylimidazolium cations produce ILs. Using these ligands, [Cu(L)Cl][X] (L = **L**^{1}–**L**^{3}, X = bis(trifluoromethanesulfonyl)amide (Tf_2N) and PF_6) were prepared (Scheme 1), and their thermal properties and coordination structures were investigated. In addition, [Cu(Me_6tren)Cl][Tf_2N] was prepared and structurally characterized for comparison.

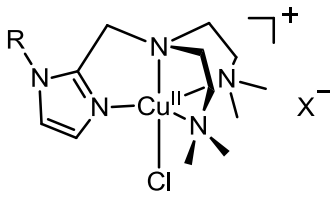

	R
[**1**][Tf_2N]	hexyl
[**2**][Tf_2N]	propyl
[**3**][Tf_2N]	methyl
[**2**][PF_6]	propyl

Scheme 1. Structural formulae of salts prepared in this study.

3.2 Results and Discussion

Preparation and properties. The tripodal ligands **L**^{1}–**L**^{3} were prepared by reductive amination of alkylimidazolecarbaldehydes with bis(2-dimethylaminoethyl)amine.[5] The copper(II) complexes [**1**][Tf_2N]–[**3**][Tf_2N] and [Cu(Me_6tren)Cl][Tf_2N] were prepared by the reaction of the ligands with Cu^{II} salts, followed by anion exchange using lithium bis(trifluoromethanesulfonyl)amide. [**1**][Tf_2N]

and [**2**][Tf_2N] were obtained as green ionic liquids, although [**2**][Tf_2N] crystallized over a few weeks. [**3**][Tf_2N] and [Cu(Me_6tren)Cl][Tf_2N] were obtained as blue crystals, and exhibited high melting points because of the absence of alkyl chains in the ligands. All of the salts were stable in air. Our efforts to obtain [Cu^I(**L1**)][Tf_2N] failed because of disproportionation, as has been observed in [Cu^I(Me_6tren)]$^+$ and related complexes.[2b–d]

We measured the temperature dependence of the viscosity of [**1**][Tf_2N]. This was a Newtonian liquid with a very high viscosity (55.1 Pa s at 25 °C), which is larger than those of typical imidazolium ILs (e.g., [butylmethylimidazolium][Tf_2N]: 49 mPa s)[6] by an order of 10^3. The activation energy (E_a) derived from the Arrhenius plot of viscosity was 99.5 kJ mol^{-1}, which is three times larger than the corresponding values for imidazolium ILs (E_a = 30–40 kJ mol^{-1}).[6] These tendencies probably reflect the high molecular weight and large molecular volume of the bulky cation. The temperature dependence was also fitted using the Vogel–Fulcher–Tammann (VFT) approximation ($\eta = \eta_0 \exp[DT_0/(T–T_0)]$),[7] where T_0 and D are the ideal glass-transition temperature and the degree of deviation from Arrhenius behavior, respectively (Figure 1). The best-fit parameters of the fitting were T_0 = 139.5 K (= −133.7 °C) and D = 25.4.

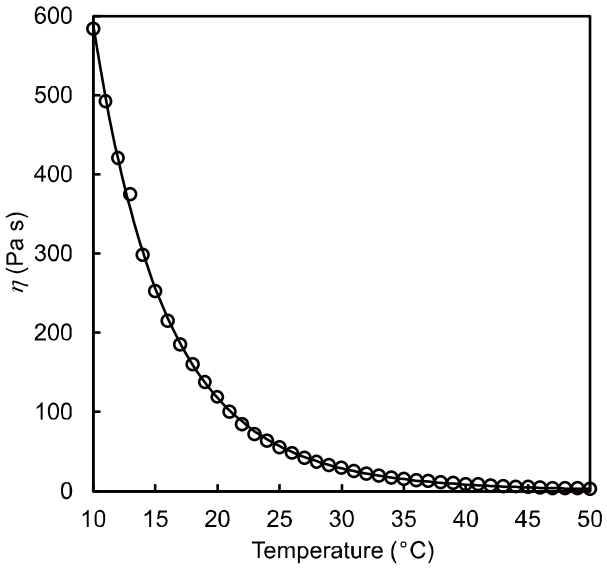

Figure 1. Temperature dependence of the viscosity of [**1**][Tf_2N] measured at 10–50 °C. Solid lines are the fitting curves using the VFT equation.

Thermal properties. Thermal properties of [**1**][Tf_2N]–[**3**][Tf_2N] were investigated by differential scanning calorimetry (DSC). Values of the melting point (T_m) and glass-transition temperature (T_g) of these salts are listed in Table 1. DSC traces of the salts are shown in Figure 2. [**1**][Tf_2N] did not crystallize upon cooling and showed a glass transition at –31 °C. The solid of [**2**][Tf_2N] melted at 71.3 °C on heating, and the liquid showed only a glass transition at –16 °C on cooling. [**3**][Tf_2N] melted at 108.4 °C, and on cooling the melt, partial crystallization occurred at around 75 °C and the residual liquid underwent a glass transition at 16 °C (Figure 2c). The values of T_g/T_m were 0.75 ([**2**][Tf_2N]) and 0.76 ([**3**][Tf_2N]), which are larger than those predicted by the empirical relationship for molecular and ionic liquids (T_g/T_m = 0.67).[8] The melting point of [Cu(Me_6tren)Cl][Tf_2N] was 198 °C.

[**2**][Tf_2N] and [**3**][Tf_2N] exhibited phase transitions in the solid state at –95.8 °C (ΔS = 1.6 J K^{-1} mol^{-1}) and –15.9 °C (ΔS = 1.3 J K^{-1} mol^{-1}), respectively. These small transition entropies indicate that structural changes at these transitions are only slight. Indeed, no structural change was detected for [**3**][Tf_2N] by X-ray crystallography.

Table 1. Values of the melting point (T_m), melting enthalpy (ΔH_m), melting entropy (ΔS_m), and glass-transition temperature (T_g) of the salts prepared in this study.

Compound	T_m (°C)	ΔH_m (kJ mol^{-1})	ΔS_m (J K^{-1} mol^{-1})	T_g (°C)
[**1**][Tf_2N]	–	–	–	–31
[**2**][Tf_2N]	71.3	14.1	40.0	–16
[**3**][Tf_2N]	108.4	28.5	74.3	16
[Cu(Me_6tren)Cl][Tf_2N]	198[a]			

[a]Observed under a microscope.

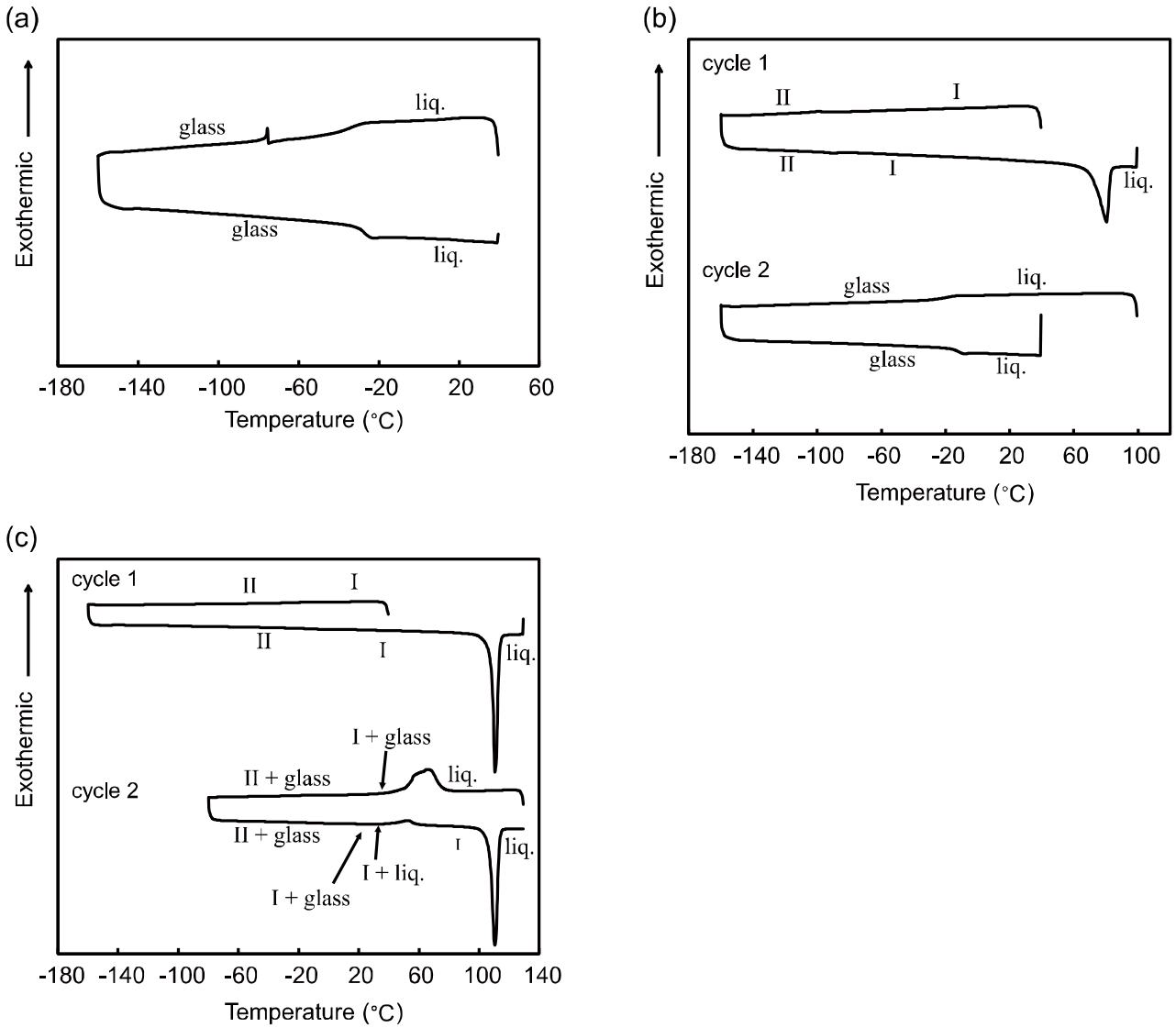

Figure 2. DSC traces of (a) [**1**][Tf_2N], (b) [**2**][Tf_2N], and (c) [**3**][Tf_2N]. The first and second cooling-heating cycles are shown in Figures (b) and (c). I and II denote different crystal phases.

Crystal structures. Crystal structures of [**2**][PF_6], [**3**][Tf_2N], and [Cu(Me_6tren)Cl][Tf_2N] were determined at 100 K. Molecular structures of the cations in [**2**][PF_6] and [**3**][Tf_2N] are shown in Figure 3. In [**3**][Tf_2N], the two dimethylaminoethyl groups in the cation were disordered over two sites. In [**3**][Tf_2N] and [Cu(Me_6tren)Cl][Tf_2N], the anions adopted the transoid conformation, as often found in salts with Tf_2N.[9] The central nitrogen and oxygen atoms and the terminal trifluoromethyl groups were disordered over two sites (Figure 4).

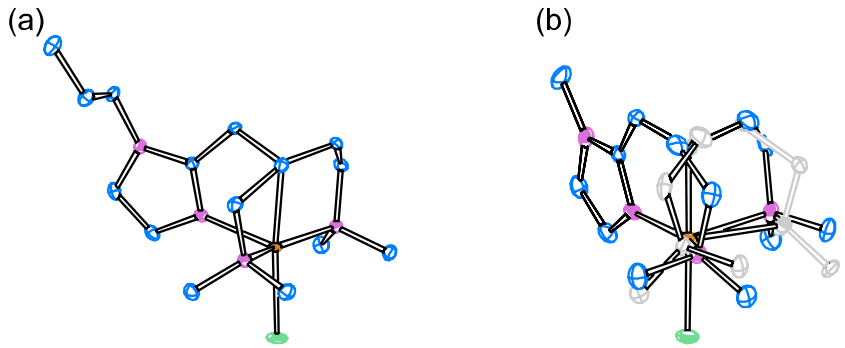

Figure 3. ORTEP diagrams of the cations in (a) [**2**][PF_6] and (b) [**3**][Tf_2N]. The dimethylaminoethyl moieties are disordered over two sites in (b).

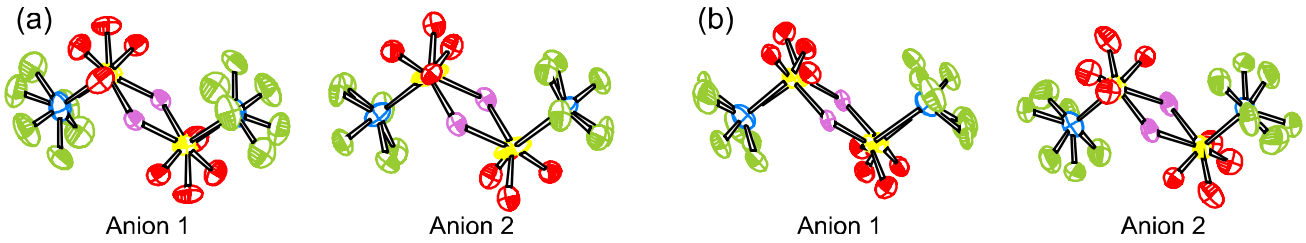

Figure 4. ORTEP drawings of the anions in (a) [**3**][Tf_2N] and (b) [Cu(Me_6tren)Cl][Tf_2N].

Five-coordinate complexes usually adopt trigonal bipyramidal, square pyramidal, or intermediate coordination geometries.[10] The structural parameter $\tau = (\beta - \alpha)/60$, where α and β are the first and the second largest coordination angles, is an indicator of the geometry[11]; τ is equal to zero for a perfectly square pyramidal geometry, while it is unity for a perfectly trigonal bipyramidal geometry. The coordination geometry of [**2**][PF_6] was nearly square pyramidal (τ = 0.31), exhibiting a large N_{NMe2}–Cu–N_{NMe2} angle (154.3°). [**3**][Tf_2N] exhibited a distorted trigonal bipyramidal geometry (τ = 0.72). The coordination geometry in [Cu(Me_6tren)Cl][Tf_2N] was trigonal bipyramidal (τ = 0.98), probably because of the high ligand symmetry. These results are consistent with the general tendency of symmetric tripodal ligands having the same three ligating units to produce trigonal bipyramidal complexes ($\tau \approx 1$),[2b,3d-e,12] and the tendency of asymmetric ligands to produce complexes closer to square pyramidal geometries ($\tau < 0.4$).[13] Packing effects may also be responsible for the distorted

structures in [**2**][PF_6] and [**3**][Tf_2N].

The Cu–N bond lengths in [**3**][Tf_2N] (Cu–N_{apical} = 2.08 Å, Cu–$N_{imidazole}$ = 2.00 Å, Cu–N_{NMe2} = 2.14 and 2.27 Å) and those in [**2**][PF_6] (Cu–$N_{imidazole}$ = 2.15 Å, Cu–N_{amine} = 2.11, 2.07, and 2.06 Å) are comparable to those in typical trigonal bipyramidal copper(II) complexes[2b,3d-e,12,14] and tetragonal copper(II) complexes[12] with similar τ values, respectively. In the latter salt, the Cu–$N_{imidazole}$ bond involving the axial nitrogen is longer than the Cu–N_{amine} bond.

Crystal structures of [**2**][PF_6] and [**3**][Tf_2N] were also determined at 298 K, but no significant differences were observed compared with those at 100 K.

UV–vis–NIR spectra. The UV–vis–NIR absorption spectrum of [**1**][Tf_2N] in the liquid state and those of [**2**][Tf_2N], [**3**][Tf_2N], and [**2**][PF_6] in the solid state were measured to obtain information on their coordination structures. All of the complexes exhibited an intense peak at around 300 nm and two broad peaks at around 740 and 940 nm (Figure 5 and Table 2). The former peak is assigned to the ligand-to-metal charge transfer transition,[15] whereas the latter peaks are ascribed to the d–d transitions.[3b–c,11–13a] It is reasonable that d–d transitions in [**1**][Tf_2N]–[**3**][Tf_2N] were observed between those in [Cu(Me_6tren)Cl][Cl] (725 and 926 nm) and [Cu(tris((1-methylimidazol -2-yl)methyl)amine)Cl][PF_6] (830 and 1123 nm). The relative intensities of the two d–d transition peaks reflect the coordination geometries of the five-coordinate copper(II) complexes.[11–13a] The comparable peak heights observed for [**2**][PF_6] suggest that it had a square-pyramidal geometry, whereas the stronger peaks at around 940 nm in [**1**][Tf_2N]–[**3**][Tf_2N] suggest that they had trigonal bipyramidal geometries. The molecular structures determined crystallographically for [**2**][PF_6] and [**3**][Tf_2N], shown above, are fully consistent with these spectral features.

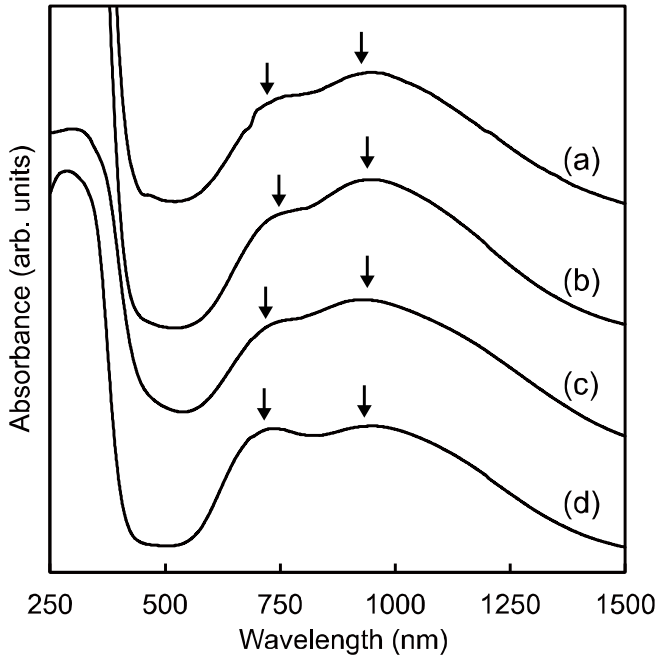

Figure 5. UV–vis–NIR absorption spectra of (a) [**1**][Tf_2N] in the liquid state, and (b) [**2**][Tf_2N], (c) [**3**][Tf_2N], and (d) [**2**][PF_6] in the solid state. The arrows indicate absorption maxima of the d–d transitions.

Table 2. Absorption maxima in the UV–vis–NIR spectra of [**1**][Tf_2N] (liquid), [**2**][Tf_2N], [**3**][Tf_2N], and [**2**][PF_6] (solids).

	λ_{LMCT} (nm)	λ_{d-d} (nm)
[**1**][Tf_2N]	302	743, 930
[**2**][Tf_2N]	312	751, 944
[**3**][Tf_2N]	289	735, 944
[**2**][PF_6]	307	734, 943

3.3 Conclusion

To develop metal-containing ILs with tripodal ligands, we designed alkylimidazole-containing tetradentate ligands and prepared their copper(II) complexes. The Tf_2N salts with hexyl and propyl substituents in the ligands were ILs with high viscosity at room temperature. The coordination structures of the crystalline complexes were found to be consistent with the UV–vis–NIR absorption spectra.

3.4 Experimental Section

General. Bis(2-dimethylaminoethyl)amine,[16] $[Cu(Me_6tren)Cl][ClO_4]$,[2b] and 1-propylimidazole-2-carbaldehyde[17] were synthesized according to procedures described in the literature. 1-Hexylimidazole-2-carbaldehyde was synthesized similarly to 1-propylimidazole-2-carbaldehyde, using formylimidazole and iodohexane. Other reagents were commercially available. ^{1}H NMR spectra were recorded on a JEOL JNM-ECL-400 spectrometer. Elemental analyses were performed using a Yanaco CHN MT5 analyzer. DSC measurements were performed in the temperature range –160 to 130 °C at a rate of 10 K min^{-1}, using a TA Instrument Q100 calorimeter. Infrared spectra were recorded using KBr plates analyzed on a Thermo Nicolet Avatar 360 spectrometer. UV–vis–NIR absorption spectra of the neat IL and crystalline salts as KBr pellets were measured on a JASCO V-570 UV/VIS/NIR spectrometer equipped with an integrating sphere (ISM–470). The viscosity was measured under a nitrogen atmosphere using a Toki Sangyo TV-22 viscometer with a 3° × R7.7 cone rotor, in the temperature range 10–50 °C.

Bis(2-dimethylaminoethyl)-((1-hexylimidazol-2-yl)methyl)amine (L^1). Under a nitrogen atmosphere, 1-hexylimidazole-2-carboxaldehyde (0.71 g, 3.94 mmol) was added dropwise to a solution of bis(2-dimethylaminoethyl)amine (0.620 g, 3.94 mmol) and $NaBH(OAc)_3$ (1.22 g, 5.75 mmol) in dichloromethane (50 mL). The reaction mixture turned into a pale brown suspension and evolved gas. The suspension was stirred for 24 h at 50 °C, and then cooled to room temperature. A saturated aqueous solution of NaOH was added to the cooled suspension. The organic phase was separated, and the aqueous phase was extracted with dichloromethane. The organic phase and the extract were combined, dried over magnesium sulfate, and concentrated under reduced pressure. The crude product was dissolved in concentrated hydrochloric acid (10 mL) and washed with dichloromethane. The aqueous phase was basified by adding small portions of NaOH, and then extracted with diethyl ether. The organic phase was dried over magnesium sulfate and concentrated under reduced pressure. The product was obtained as a yellow oil (0.471 g, yield 37%). ^{1}H NMR

(400 MHz, $CDCl_3$, TMS): δ = 0.89 (t, 3H, J = 6.8 Hz), 1.21 (br, 6H), 1.72 (m, 2H), 2.20 (s, 12H), 2.34 (t, 4H, J = 7.2 Hz), 2.60 (t, 4H, J = 7.2 Hz), 3.73 (s, 2H), 4.04 (t, 2H, J = 7.6 Hz), 6.86 (d, 1H, J = 1.2 Hz), 6.91 (d, 1H, J = 1.6 Hz).

Bis(2-dimethylaminoethyl)-((1-propylimidazol-2-yl)methyl)amine (L^2). This ligand was prepared as described for $\mathbf{L^1}$, using 1-propylimidazole-2-carboxaldehyde (0.48 g, 3.47 mmol) instead of 1-hexylimidazole-2-carboxaldehyde. The product was obtained as a yellow oil (0.278 g, yield 29%). ^{1}H NMR (400 MHz, $CDCl_3$, TMS): δ = 0.94 (t, 3H, J = 6.8 Hz), 1.79 (m, 2H), 2.17 (s, 12H), 2.35 (t, 4H, J = 7.2 Hz), 2.60 (t, 4H, J = 7.2 Hz), 3.74 (s, 2H), 4.04 (t, 2H, J = 7.2 Hz), 6.86 (d, 1H, J = 1.2 Hz), 6.92 (d, 1H, J = 1.6 Hz).

Bis(2-dimethylaminoethyl)-((1-methylimidazol-2-yl)methyl)amine (L^3). This ligand was prepared as described for $\mathbf{L^1}$, using 1-methylimidazole-2-carboxaldehyde (0.67 g, 4.25 mmol) instead of 1-hexylimidazole-2-carboxaldehyde. The reaction mixture was stirred for 35 h at 50 °C, and then a saturated aqueous solution of $NaHCO_3$ was added to quench the reaction. The product was obtained as a yellow oil (0.22 g, yield 23%). ^{1}H NMR (400 MHz, $CDCl_3$, TMS): δ = 2.23 (s, 12H), 2.43 (t, 4H, J = 6.8 Hz), 2.67 (t, 4H, J = 7.0 Hz), 3.71 (s, 3H), 3.76 (s, 2H), 6.84 (d, 1H, J = 1.2 Hz), 6.90 (d, 1H, J = 0.8 Hz).

[Cu(L^1)Cl][Tf_2N] ([1][Tf_2N]). An aqueous solution (2 mL) of $CuCl_2{\cdot}2H_2O$ (48 mg, 0.28 mmol) and $Cu(ClO_4)_2{\cdot}6H_2O$ (105 mg, 0.28 mmol) was added to a solution of $\mathbf{L^1}$ (165 mg, 0.50 mmol) in methanol (2 mL), and the reaction mixture was stirred for 5 min. Methanol (5 mL) and Li[Tf_2N] (0.20 g, 0.75 mmol) were then added successively to the solution and the resulting mixture was stirred for 15 min. The reaction mixture was then concentrated under reduced pressure, and the obtained crude product was dissolved in dichloromethane and washed with water. When an emulsion was formed, brine was added to the solution and the mixture was allowed to stand for a few minutes. The organic phase was separated, dried over magnesium sulfate, and concentrated under reduced pressure. The residual liquid was dissolved in methanol and washed repeatedly with hexane. The

methanol phase was separated, concentrated under reduced pressure, and washed repeatedly with diethyl ether. The obtained liquid was dried under vacuum at room temperature, and then dried by repeated freeze–pump–thaw cycles to completely remove residual solvents. The product was obtained as a viscous turquoise-blue liquid (366 mg, yield 63%). Anal. Calcd. for $C_{20}H_{37}ClCuF_6N_6O_4S_2$ (702.66): C, 34.19; H, 5.31; N, 11.96. Found: C, 34.39; H, 5.33; N, 11.88. The color of the product changed from turquoise-blue to green when stored for over a week at room temperature under a nitrogen atmosphere. The IR and UV spectra and elemental analysis results were identical before and after this change. The reason for this change is unknown but it may be ascribed to a change in the coordination environment or partial elimination of the axial chloride ligands in the cation.

[Cu(L^2)Cl][Tf_2N] ([2][Tf_2N]). This salt was prepared as described for [**1**][Tf_2N], using $\mathbf{L^2}$. The product was obtained as a viscous green liquid, which solidified over several weeks at room temperature under a nitrogen atmosphere. The product was obtained as a green solid (140 mg, yield 42%). Anal. Calcd. for $C_{17}H_{31}ClCuF_6N_6O_4S_2$ (660.59): C, 30.91; H, 4.73; N, 12.72. Found: C, 30.93; H, 4.71; N, 12.68.

[Cu(L^3)Cl][Tf_2N] ([3][Tf_2N]). This salt was prepared as described for [**1**][Tf_2N], using $\mathbf{L^3}$. The product was obtained as a viscous green liquid, which was recrystallized by slow diffusion of diethyl ether into an acetone solution of the crude product. Turquoise-blue prismatic crystals were obtained (7 mg, yield 17%), together with green solids. Anal. Calcd. for $C_{15}H_{27}ClCuF_6N_6O_4S_2$ (632.53): C, 28.48; H, 4.30; N, 13.29. Found: C, 28.42; H, 4.25; N, 13.26.

[Cu(L^2)Cl][PF_6] ([2][PF_6]). An aqueous solution (2 mL) of $CuCl_2{\cdot}2H_2O$ (86 mg, 0.47 mmol) and an aqueous solution (5 mL) of KPF_6 (110 mg, 0.60 mmol) were successively added to $\mathbf{L^2}$ (130 mg, 0.46 mmol), and the reaction mixture was stirred for 30 min. The resultant mixture was extracted with dichloromethane, and the organic phase was washed with water, dried over magnesium sulfate, and concentrated under reduced pressure. The residual turquoise-blue liquid was recrystallized by

slow diffusion of diethyl ether and hexane into an acetone solution. The product was obtained as light-blue block crystals (87.8 mg, yield 36%). Anal. Calcd. for $C_{15}H_{31}ClCuF_6N_5P$ (525.40): C, 34.29; H, 5.95; N, 13.33. Found: C, 33.17; H, 5.76; N, 12.87.

[Cu(Me$_6$tren)Cl][Tf$_2$N]. Li[Tf$_2$N] (72 mg, 0.25 mmol) was added to an aqueous solution (7 mL) of [Cu(Me$_6$tren)Cl]ClO$_4$ (71 mg, 0.17 mmol) under stirring, and the solution was further stirred for 5 min. The reaction mixture was then extracted with dichloromethane and the organic phase was washed with water, dried over magnesium sulfate, and concentrated under reduced pressure. The obtained light-green powder was recrystallized by slow diffusion of diethyl ether and hexane into an acetone solution. The product was obtained as light-green plate crystals (43 mg, yield 42%). Anal. Calcd. for $C_{14}H_{30}ClCuF_6N_5O_4S_2$ (609.54): C, 27.61; H, 4.99; N, 11.52. Found: C, 27.59; H, 4.96; N, 11.49.

X-ray structure determination. Single crystals of [**2**][PF$_6$], [**3**][Tf$_2$N], and [Cu(Me$_6$tren)Cl][Tf$_2$N] were obtained by slow diffusion of diethyl ether and hexane into a dichloromethane solution, ether into an acetone solution, and diethyl ether and hexane into an acetone solution, respectively. XRD data were collected on a Bruker APEX II Ultra CCD diffractometer at 100 K, using Mo Kα radiation (λ = 0.71073 Å). Crystal data, data collection parameters, and analysis statistics for these compounds are listed in Table 3. All calculations were performed using SHELXL.[18] The nonhydrogen atoms were refined anisotropically, and the hydrogen atoms were inserted at calculated positions. Empirical absorption corrections (SADABS)[19] were applied. The packing diagrams were drawn using ORTEP 3 for Windows.[20] CCDC 930374 ([**2**][PF$_6$]), 930375 ([**3**][Tf$_2$N]), and 930376 ([Cu(Me$_6$tren)Cl][Tf$_2$N]) contain the supplementary crystallographic data for this chapter. These data can be obtained free of charge from the Cambridge Crystallographic Data Centre via www.ccdc.cam.ac.uk/data_request/cif.

Table 3. Crystallographic parameters for [**2**][PF_6], [**3**][Tf_2N], and [Cu(Me_6tren)Cl][Tf_2N].

	[**2**][PF_6]	[**3**][Tf_2N]	[Cu(Me_6tren)Cl][Tf_2N]
Empirical formula	$C_{15}H_{31}ClCuF_6N_5P$	$C_{15}H_{27}ClCuF_6N_6O_4S_2$	$C_{14}H_{30}ClCuF_6N_5O_4S_2$
Formula weight	525.41	632.54	609.54
Temperature (K)	100	100	100
Crystal system	Triclinic	Triclinic	Monoclinic
Space group	*P*–1 (No. 2)	*P*–1 (No. 2)	$P2_1/c$ (No. 14)
a (Å)	8.4294(14)	8.1069(14)	12.236(5)
b (Å)	10.0642(16)	8.5666(15)	15.751(5)
c (Å)	13.427(2)	20.655(4)	16.495(5)
α (°)	102.327(2)	87.973(2)	
β (°)	99.113(2)	79.639(2)	128.831(19)
γ (°)	90.022(2)	63.172(2)	
Volume (Å^3)	1098.1(3)	1257.5(4)	2476.5(15)
Z	2	2	4
d_{calcd} (g cm^{-3})	1.589	1.671	1.635
μ (mm^{-1})	1.251	1.220	1.234
Reflections collected	5303	5996	11662
Independent reflections	3803	4318	4375
Parameters	267	525	412
R_1[a], wR_2[b] ($I > 2\sigma(I)$)	0.0229, 0.0584	0.0486, 0.1173	0.0610, 0.1482
R_1[a], wR_2[b] (all data)	0.0244, 0.0596	0.0518, 0.1204	0.0687, 0.1511
Goodness-of-fit on F^2	1.037	1.031	1.050

[a] $R_1 = \Sigma||F_o| - |F_c||/\Sigma |F_o|$. [b] $wR_2 = [\Sigma w(F_o^2 - F_c^2)^2/\Sigma w(F_o^2)^2]^{1/2}$.

References

(1) (a) A. G. Blackman, *Polyhedron*, **2005**, *24*, 1–39; (*b*) A. G. Blackman, *Eur. J. Inorg. Chem.*, **2008**, 2633–2647.

(2) (a) L. M. Mirica, X. Ottenwaelder, T. D. P. Stack, *Chem. Rev.*, **2004**, *104*, 1013–1045; (b) M. Becker, F. W. Heinemann, S. Schindler, *Chem.–Eur. J.*, **1999**, *5*, 3124–3129; (c) M. Weitzer, S. Schindler, G. Brehm, E. Hörmann, B. Jung, S. Kaderli, A. D. Zuberbühler, *Inorg. Chem.*, **2003**, *42*, 1800–1806; (d) C. Würtele, O. Sander, V. Lutz, T. Waitz, F. Tuczek, S. Schindler, *J. Am. Chem. Soc.*, **2009**, *131*, 7544–7545.

(3) (a) M. Ciampolini, N. Nardi, G. P. Speroni, *Coord. Chem. Rev.,* **1966**, *1*, 222–233; (b) M. Ciampolini, N. Nardi, *Inorg. Chem.*, **1966**, *5*, 41–44; (c) R. Barbucci, A. Mastroianni, *Inorg. Chim. Acta*, **1975**, *15*, L15–L16; (d) U. Baisch, R. Poli, *Polyhedron*, **2008**, *27*, 2175–2185; (e) W. T. Eckenhoff, T. Pintauer, *Dalton Trans.*, **2011**, *40*, 4909–4917.

(4) (a) J. E. Hein, V. V. Fokin, *Chem. Soc. Rev.*, **2010**, *39*, 1302–1315; (b) K. Matyjaszewski, *Macromolecules*, **2012**, *45*, 4015–4039; (c) F. D. Campo, D. Lastecoueres, J. M. Vincent, J. B. Verlhac, *J. Org. Chem.*, **1999**, *64*, 4969–4971.

(5) (a) G. J. P. Britovsek, J. England, A. J. P. White, *Inorg. Chem.*, **2005**, *44*, 8125–8134; (b) M. Balamurugan, R. Mayilmurugan, E. Suresh, M Palaniandavar, *Dalton Trans.*, **2011**, *40*, 9413–9424.

(6) A. Paul, A. J. Samanta, *J. Phys. Chem. B*, **2008**, *112*, 16626–16632.

(7) (a) G. S. Fulcher, *J. Am. Ceram. Soc.*, **1925**, *8*, 339–355; (b) C. A. Angell, *J. Non-Cryst. Solids*, **1999**, *131–133*, 13–31.

(8) (a) D. Turnbull, M. H. Cohen, *Modern Aspect of the Vitreous State*, Butterworth, London, **1960**, Vol. *1*, p. 38. (b) O. Yamamuro, Y. Minamimoto, Y. Inamura, S. Hayashi, H. Hamaguchi, *Chem. Phys. Lett.*, **2006**, *423* 371–375.

(9) W. A. Henderson, M. Herstedt, V. G. Young, Jr., S. Passerini, H. C. De Long, P. C. Trulove,

Inorg. Chem., **2006**, *45*, 1412–1414.

(10) L. Sacconi, *Pure Appl. Chem.*, **1968**, *17*, 95–128.

(11) A. W. Addison, T. N. Rao, J. Reedjik, J. V. Rijn, G. C. Verschoor, *J. Chem. Soc., Dalton Trans.*, **1984**, 1349–1356.

(12) K. J. Oberhausen, R. J. O'Brien, J. F. Richardson, R. M. Buchanan, *Inorg. Chim. Acta*, **1990**, *173*, 145–154.

(13) (a) N. Wei, N. N. Murthy, K. D. Karlin, *Inorg. Chem.*, **1994**, *33*, 6093–6100; (b) A. M. Dittler-Klingemann, F. E. Hahn, *Inorg. Chem.*, **1996**, *35*, 1996–1999; (c) M. Scarpellini, A. Neves, E. E. Castellano, E. F. de Almeida Neves, D. W. Franco, *Polyhedron*, **2004**, *23*, 511–518.

(14) A. Schiller, R. Scopelliti, K. Severin, *Dalton Trans.*, **2006**, 3858–3867.

(15) E. Bernarducci, P. K. Bharadwaj, K. Krogh-Jespersen, J. A. Potenza, H. J. Schugar, *J. Am. Chem. Soc.*, **1983**, *105*, 3860–3866.

(16) H. Luitjes, M. Schakel, G. W. Klumpp, *Synth. Commun.*, **1994**, *24*, 2257–2261.

(17) M. Seto, N. Miyamoto, K. Aikawa, Y. Aramaki, N. Kanzaki, Y. Iizawa, M. Baba, M. Shiraishi, *Bioorg. Med. Chem.*, **2005**, *13*, 363–386.

(18) G. M. Sheldrick, *SHELXL: Program for the Solution for Crystal Structures*, University of Göttingen, Germany, **1997**.

(19) G. M. Sheldrick, *SADABS: Program for Semi-empirical Absorption Correction*, University of Göttingen, Germany, **1997**.

(20) L. J. Farrugia, *J. Appl. Crystallogr.*, **1999**, *32*, 837–838.

CHAPTER 4

Magnetic-Field Responsive Ionic Liquids Containing Ferrocenium Cations

4.1 Introduction

Ferrocenium cations are interesting from the viewpoint of magnetism,[1] and they are suitable as components of ionic liquids because of their bulkiness and charge delocalization. However, ferrocenium ionic liquids are highly sensitive to air.[2] In this study, alkyloctamethylferrocenium cations were used to achieve air-stable ferrocenium ionic liquids. There are a few examples of liquid-like peralkylated ferrocenium salts, such as alkali metal podates with ether substituents[3] and liquid crystal salts with mesogenic substituents.[4]

In this chapter, the preparation and physical properties of alkyloctamethylferrocenium salts with the Tf_2N anion ($[Fe(C_5Me_4C_nH_{2n+1})(C_5Me_4H)][Tf_2N]$, Scheme 1), which are air-stable paramagnetic ionic liquids are described. 1-Pentenyloctamethylferrocene was also used as the cation, and several nitrate (NO_3) and hexafluorophosphate (PF_6) salts were prepared for comparison. Discussion of the crystal structure is useful in elucidating the nature of ionic liquids.[5] Although structural data were not available for the ferrocenium ionic liquids, structural determination of the present salts was possible.

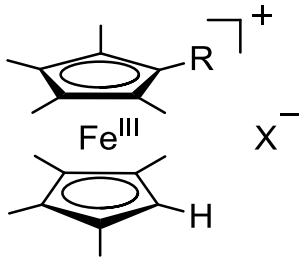

X = Tf_2N, PF_6, NO_3

	R
[**C3Fc**][X]	*n*-propyl
[**C4Fc**][X]	*n*-butyl
[**C5Fc**][X]	*n*-pentyl
[**C6Fc**][X]	*n*-hexyl
[**C8Fc**][X]	*n*-octyl
[**C10Fc**][X]	*n*-decyl
[**C12Fc**][X]	*n*-dodecyl
[**C17Fc**][X]	*n*-heptadecyl
[**C5'Fc**][X]	1-pentenyl

Scheme 1. Structural formulae of alkyloctamethylferrocenium salts prepared in this study. Abbreviations for the salts are also shown.

4.2 Results and Discussion

Preparation and properties. The alkyloctamethylferrocenium salts were prepared according to Scheme 2. Octamethylformylferrocene was reacted with Grignard reagents, and the resultant alcohols were reduced to give alkyloctamethylferrocenes as yellow-orange oils, which were further reacted with Ag[X] (X = Tf_2N, PF_6, and NO_3) to give the desired salts. The Tf_2N salts ([**C3Fc**][Tf_2N]–[**C17Fc**][Tf_2N]) were obtained as dark-green oils or solids, which were stable under air. The 1-pentenyl derivative [**C5'Fc**][Tf_2N] was prepared similarly. The melting points (T_m) of the Tf_2N salts were in the range 15–70 °C. The PF_6 salts ([**C4Fc**][PF_6], [**C6Fc**][PF_6], and [**C10Fc**][PF_6]) and NO_3 salts ([**C6Fc**][NO_3] and [**C10Fc**][NO_3]) were obtained as dark-green solids. The melting points of these salts were above 100 °C except for [**C10Fc**][NO_3], which melted at about 80 °C.

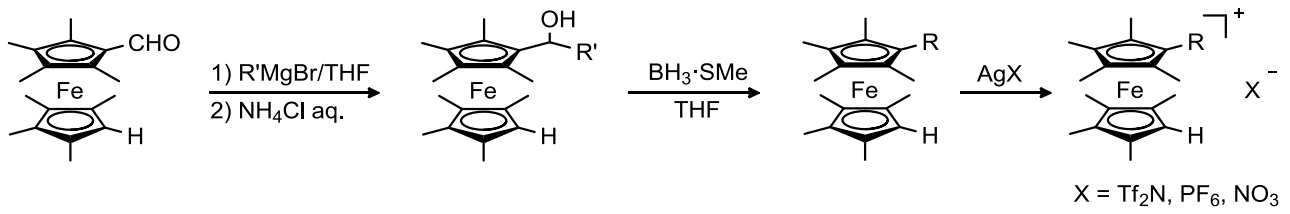

Scheme 2 Scheme for preparation of alkyloctamethylferrocenium salts.

Melting points of Tf_2N salts and their precursors. The melting points, melting entropies, and glass transition temperatures of the Tf_2N salts are listed in Table 1. The melting points are plotted in Figure 1 as a function of the alkyl chain length. Compared with [$Fe(C_5Me_4H)_2$][Tf_2N] (T_m = 213 °C),[6] introduction of alkyl chains significantly decreased the melting points. The melting points decreased with increasing chain length up to n = 8 and then increased, where n is the number of carbon atoms in the chain. This tendency is similar to that observed in ionic liquids of alkylimidazolium salts.[7] The melting points of the present salts are higher by 10–30 °C than those of [Rmim][Tf_2N] (Rmim = 1-alkyl-3-methylimidazolium)[7b] and [$Fe(C_5H_4R)(C_5H_5)$][Tf_2N][2] with the same alkyl chain lengths, which is consistent with the larger molecular weights and volumes of the

cations. The melting point of the alkenyl derivative [**C5'Fc**][Tf_2N] (T_m = 56.9 °C) was higher than that of the alkyl derivative [**C5Fc**][Tf_2N] (T_m = 30.0 °C and 20.2 °C, vide infra) as a result of the decreased flexibility of the substituent.

Table 1. Melting points (T_m), melting entropies (ΔS_m), phase transition temperatures (T_{c1}, T_{c2}), phase transition entropies (ΔS_{c1}, ΔS_{c2}), and the sums of the phase transition entropies (ΔS_{total}) of the Tf_2N, PF_6, and NO_3 salts.

	T_m (°C)	ΔS_m (J K^{-1} mol^{-1})	T_{c1} (°C)	ΔS_{c1} (J K^{-1} mol^{-1})	T_{c2} (°C)	ΔS_{c2} (J K^{-1} mol^{-1})	ΔS_{total}[a] (J K^{-1} mol^{-1})
[**C3Fc**][Tf_2N]	67.4	16.6	45.4	90.5			107.1
[**C4Fc**][Tf_2N]	34.4	86.3					86.3
[**C5Fc**][Tf_2N]	30.0	98.5					98.5
	20.2[b]	20.4	0.5[b]	44.0[b]			–
[**C5'Fc**][Tf_2N]	56.9	80.7					80.7
[**C6Fc**][Tf_2N]	27.7	27.4	21.4	55.2			84.6
			–1.6[b]	39.7[b]			
[**C8Fc**][Tf_2N]	16.9	12.5	1.7	19.9	11.5	2.5	34.9
[**C10Fc**][Tf_2N]	17.5	12.5	11.0	14.7			27.2
[**C12Fc**][Tf_2N]	26.2	18.0	8.7	36.5			54.5
[**C17Fc**][Tf_2N]	56.8	97.3					93.6
[**C4Fc**][PF_6]	166.8	26.1	–53.8	4.4	108.1	28.6	59.1
[**C6Fc**][PF_6]	142.1	26.7	109.9	1.1	132.2	7.3	35.1
[**C10Fc**][PF_6]	201.4	39.8	–44.5	20.5	49.2	7.0	64.3
			54.2[b]	32.9[b]			
[**C6Fc**][NO_3]	109.4	26.6					26.6

[a] $\Delta S_{total} = \Delta S_m + \Delta S_{c1} + \Delta S_{c2}$. [b] Phase transitions in metastable polymorphs.

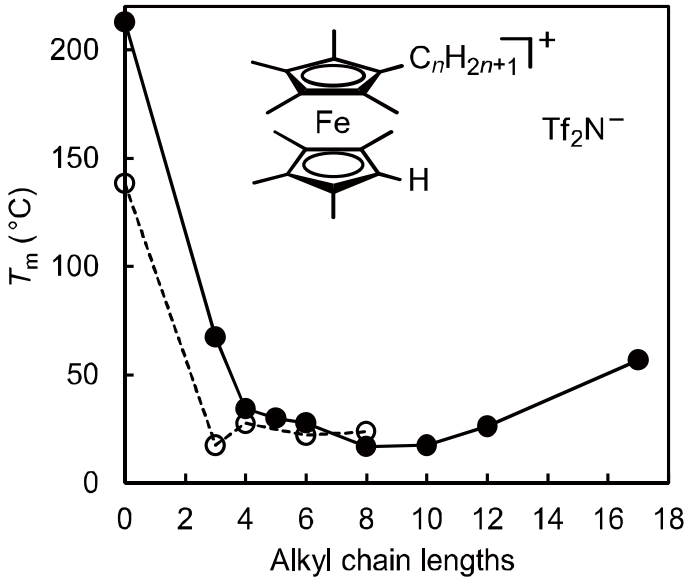

Figure 1. Melting points of Tf_2N salts (●) and alkyloctamethylferrocenes (○) plotted as a function of the alkyl-chain length. The values for octamethylferrocene and its Tf_2N salt (n = 0) are also shown.

The thermal properties of alkyloctamethylferrocenes, which are the precursors of the salts, were also examined (Table 2). They melted at around 20 °C, and exhibited glass transitions at around –85 °C when cooled from the liquid state. Crystallization was observed in the heating process from the glassy state, except for the pentyl and 1-pentenyl derivatives. It is interesting that the melting points of alkyloctamethylferrocenes (open circles) and their Tf_2N salts (filled circles) are comparable (Figure 1).

Table 2. Melting points (T_m), melting entropies (ΔS_m), and glass transition temperatures (T_g) of alkyloctamethylferrocenes.

	T_m / °C	ΔS_m / J K^{-1} mol^{-1}	T_g / °C
C3Fc	17.5	68.9	–97
C4Fc	27.6	80.6	–88
C5Fc	–	–	–86
C5'Fc	–	–	–84
C6Fc	22.1	84.7	–83
C8Fc	23.8	34.7	–84

The ratios of the melting points and glass transition temperatures (T_g/T_m) for the alkyloctamethylferrocenes were 0.61–0.65. In the Tf_2N salts, the glass transition was only observed in the pentenyl derivative [**C5'Fc**][Tf_2N] (T_g = –67 °C) when the liquid was cooled at a rate faster than 10 K min^{-1}. The T_g/T_m ratio for this salt was 0.62. These ratios are consistent with the empirical relationship ($T_g/T_m \approx 2/3$) known for general molecular compounds[8] and also for alkylimidazolium ionic liquids.[9]

Phase transitions in the Tf_2N salts. The phase sequences of the Tf_2N salts are shown in Figure 2. [**C4Fc**][Tf_2N], [**C5'Fc**][Tf_2N], and [**C17Fc**][Tf_2N] exhibited no phase transitions in the solid state (Figure 2a). [**C3Fc**][Tf_2N], [**C10Fc**][Tf_2N], and [**C12Fc**][Tf_2N] exhibited one phase transition and [**C8Fc**][Tf_2N] exhibited two phase transitions in the solid state (Figure 2b). The large values of ΔS indicate that extensive molecular motions occur above the phase transition temperatures, not merely rotational and/or conformational disorder of anions.

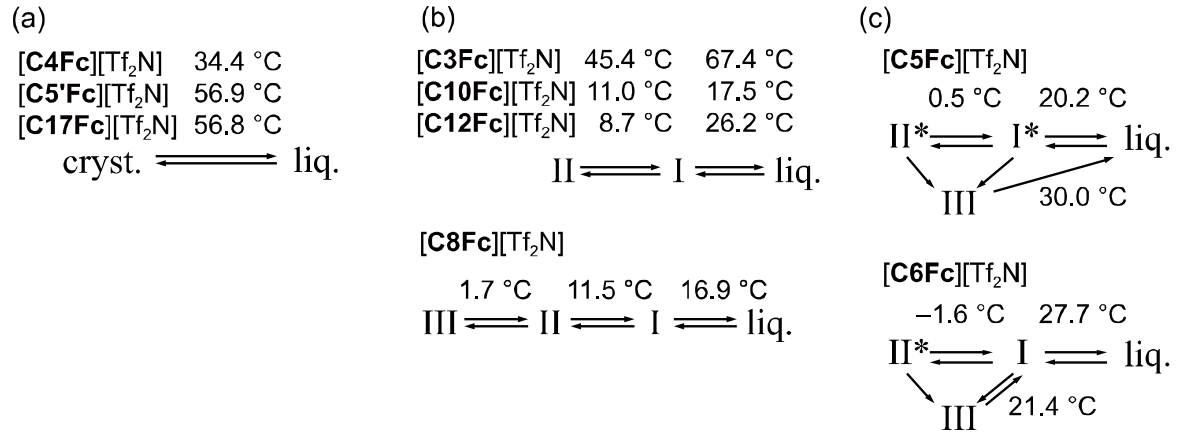

Figure 2. Phase sequences of Tf_2N salts. Different crystal phases are represented as I–III. The asterisks indicate metastable phases.

The high-temperature phases in these salts are orientationally disordered phases with small melting entropies (ΔS < 20 J K^{-1} mol^{-1}).[10] Among them, [**C10Fc**][Tf_2N] showed a glass transition in the crystal phase (phase II) at –40 °C, where the motions of the alkyl chains are probably frozen to form a glassy crystal. [**C5Fc**][Tf_2N] and [**C6Fc**][Tf_2N] exhibited three crystal phases, including metastable phases (Figure 2c). The differential scanning calorimetry (DSC) traces for [**C5Fc**][Tf_2N] are shown in Figure 3a. The Gibbs free energy diagram for this salt derived from the data is shown in Figure 4a. The melting points of the stable phase (phase III) and the metastable phase (phase I) were 30.0 °C and 20.2 °C, respectively, and their melting entropies (ΔS_m) were 98.5 J K^{-1} mol^{-1} and 20.4 J K^{-1} mol^{-1}, respectively. The latter small entropy indicates that phase I is a highly disordered phase. When cooled from the melt, crystallization occurred at around –2.3 °C to give phase I, and with further cooling, a phase transition to phase II occurred at around –11.5 °C (ΔS = 44.2 J K^{-1} mol^{-1}). In the heating run, phase I melted at 20.2 °C (Figure 3a, cycle 3), but an unprecedented, exothermal transition to phase III often occurred (Figures 3a, cycles 1–2). In the heating run, a transition from phase II to III occurred at –8.5 °C (Figures 3a, cycle 1). In the cycle 2 shown in Figure 3a, a transition from phase II to I occurred at 0.4 °C, followed by an exothermal transition to phase III, which melted at 30.0 °C. [**C6Fc**][Tf_2N] showed a similar but slightly different behavior. The DSC traces and Gibbs free energy diagram of the [**C6Fc**][Tf_2N] are shown in Figure 3b and Figure 4b, respectively. In this salt, a reverse phase sequence was often traced, but the transformation to phase III occurred occasionally. Upon cooling at 10 K min^{-1} from the liquid state, crystallization to phase I occurred at –10.6 °C, which was immediately followed by a transition to phase II (Figure 3b, cycle 1). Upon cooling at 1 K min^{-1}, these peaks could be separated, and upon heating at 1 K min^{-1} from phase II, a reverse phase sequence was observed. However, as noted above, heating phase II at 10 K min^{-1} occasionally gave rise to an exothermic transition to phase III, as can be seen in Figure 3b (cycle 1, heating run). In this figure, the transition occurred at –10 °C, which was followed by a transition to phase I at 21.4 °C and melting at 27.7 °C. A DSC pattern as shown in cycle 2 of Figure

3b was also observed several times, which revealed phase transitions from phase II to phase I at –1.6 °C (ΔS = 39.7 J mol^{-1} K^{-1}), from phase I to phase III with a broad exothermic peak at 10 °C, and again back to phase I, and subsequent melting. This re-entrant behavior was often observed when the compound was heated directly after crystallization. Cooling from phase I at 2 K min^{-1} gave phase III, as shown in Figure 3b, cycle 3.

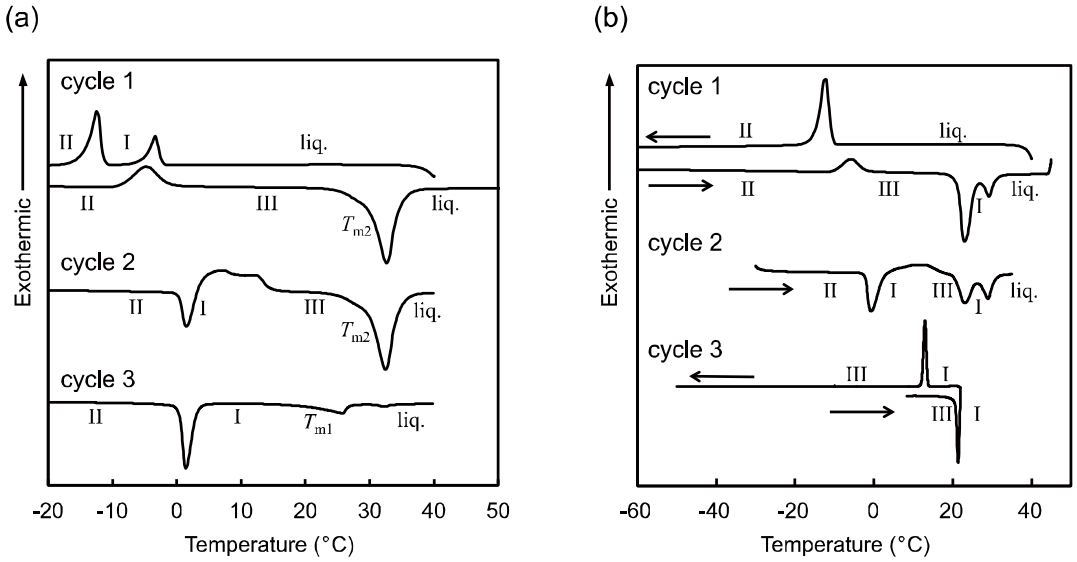

Figure 3. DSC traces of (a) [**C5Fc**][Tf_2N] and (b) [**C6Fc**][Tf_2N].

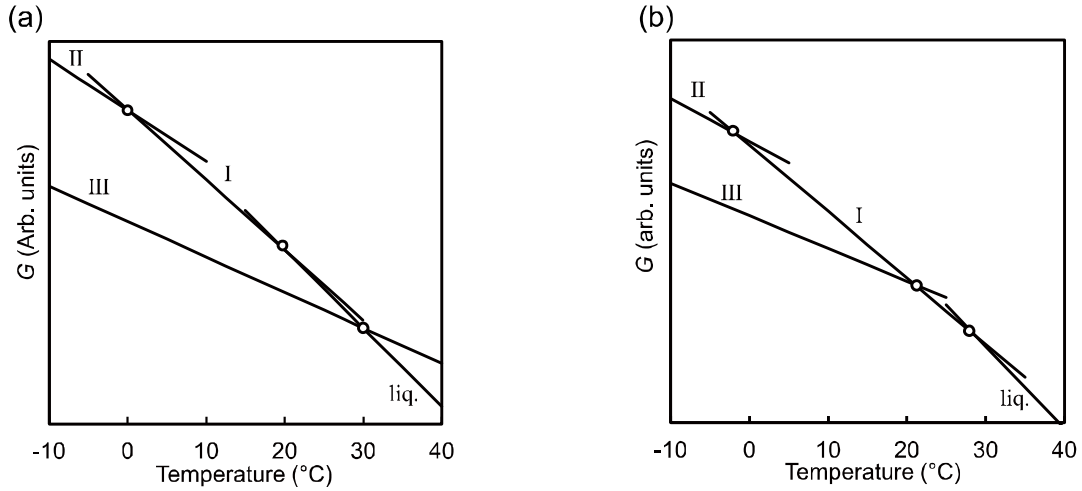

Figure 4. Schematic Gibbs free energy diagrams for (a) [**C5Fc**][Tf_2N] and (b) [**C6Fc**][Tf_2N]. The free energy curves are approximated by straight lines for simplicity.

The sums of the entropies of the melting and solid phase transitions for the Tf_2N salts (ΔS_{total}) are shown in Figure 5. The values for the salts with n = 3, 4, 5, and 6 were comparable (80–110 J K^{-1} mol^{-1}), whereas the salt with n = 8 exhibited a much smaller value, and the salts with $n \geq 10$ displayed an increase with elongation of the alkyl chain. For molecules consisting of a rigid core and alkyl chains, such as mesogens and alkylimidazolium ionic liquids, conformational changes of the alkyl chains provide an entropy change of about 10 J K^{-1} mol^{-1} per methylene unit.[11] The Tf_2N salts with $n \geq 10$ followed this tendency well, which indicates that the motion of the alkyl groups dominates the phase change entropies in these salts. The absence of such a tendency in the salts with $n \leq 6$ is partly because the entropy contributions from the alkyl moieties are small in the short chain salts, and, moreover, is probably the result of different packing structures (vide infra). The total phase transition entropy in [**C5'Fc**][Tf_2N] (80.7 J K^{-1} mol^{-1}) was smaller by about 20 J K^{-1} mol^{-1} than that in [**C5Fc**][Tf_2N] (98.5 J K^{-1} mol^{-1}), which is consistent with the loss of rotational freedom of two methylene groups.

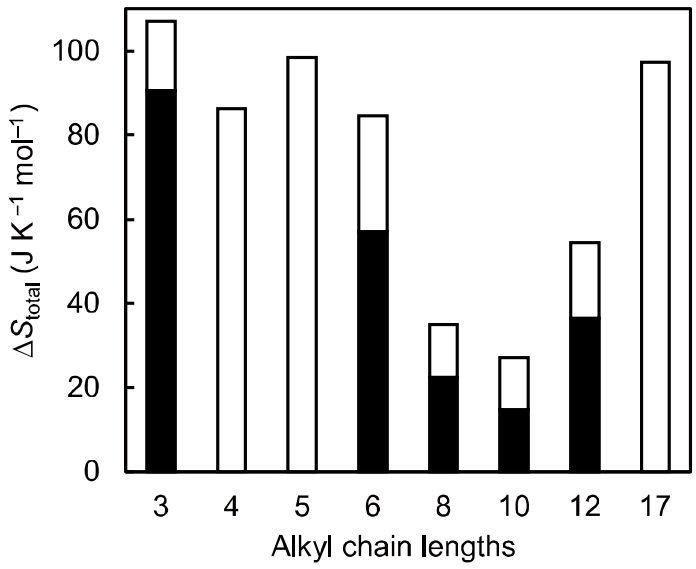

Figure 5. Sums of phase transition entropies of Tf_2N salts. The dark-gray areas are the entropies of solid phase transitions, and the others are the melting entropies.

It is interesting to note that the total phase transition entropies of alkyloctamethylferrocenes and the Tf_2N salts are comparable (Figure 5 and Table 2), as well as the melting points, as noted above. A linear correlation between the melting points of the salts and the precursors has also been observed in alkylferrocenium Tf_2N salts.[2b] These results demonstrate that the thermodynamic properties of the Tf_2N salts reflect those of their precursors.

Thermal properties of PF_6 and NO_3 salts. The melting points of [**C4Fc**][PF_6], [**C6Fc**][PF_6], and [**C10Fc**][PF_6] were 166.8 °C, 142.1 °C, and 201.4 °C respectively, and they first decreased and then increased with increasing chain length. The melting points of the PF_6 salts were higher by 100–150 °C than those of the corresponding Tf_2N salts. The PF_6 salts exhibited two phase transitions in the solid state, showing three stable crystalline phases (phase I–III). Their phase transition data are shown in Table 1. [**C10Fc**][PF_6] was obtained as a metastable glassy crystal, which was transformed to the stable phase (phase I) by heating (Figure 6). The sums of the phase transition entropies for the salts with n = 4, 6, and 10 were 59.1 J K^{-1} mol^{-1}, 35.1 J K^{-1} mol^{-1}, and 64.3 J K^{-1} mol^{-1}, respectively. The dependence on n is similar to that observed in the Tf_2N salts shown above. The increase in the value for the last salt is accounted for by the increased alkyl chain length, and the different tendency for the salt with n = 4 is ascribed to different packing structures, as shown below.

The melting point of [**C6Fc**][NO_3] was 109.4 °C (ΔS = 26.6 J K^{-1} mol^{-1}), which is much higher than that of the corresponding Tf_2N salt ([**C6Fc**][Tf_2N]: T_m = 27.7 °C). Crystallization from the melt occurred at 23.5 °C when cooled at 2 K min^{-1}, but a glass transition (T_g = –35 °C) was observed when the cooling rate was faster than 10 K min^{-1}. [**C10Fc**][NO_3] and [**C17Fc**][NO_3] melted at around 80–82 °C and 112–120 °C, respectively, but these are not precise melting points because of small amounts of remaining solvate molecules.

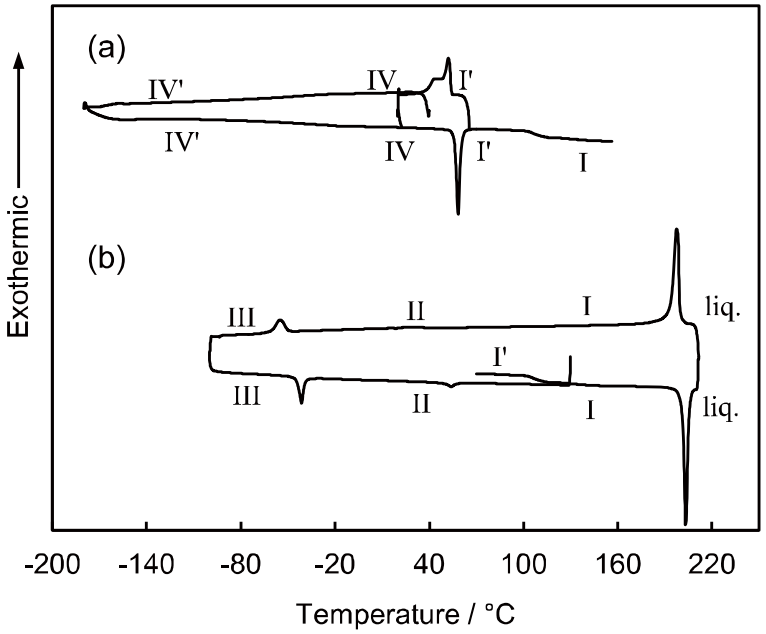

Figure 6. DSC traces of [**C10Fc**][PF_6] measured at 10 °C min^{-1}. Cycles (a) before and (b) after experiencing glass transition from phase I' to phase I are shown.

Viscosities. The viscosities of [**C6Fc**][Tf_2N] and [**C10Fc**][Tf_2N] at 25 °C were 752 mPa s and 746 mPa s, respectively, and they were comparable. Both were Newtonian liquids, and they were much more viscous than the imidazolium ionic liquids (e.g., [bmim][Tf_2N]: 49 mPa s, bmim = 1-butyl-3-methylimidazolium)[12] and ferrocenium ionic liquids (e.g., [Fe($C_5H_4{}^nBu$)(C_5H_5)][Tf_2N]: 112.3 mPa s).[2] The temperature dependences of the viscosities were fitted using the Arrhenius plot, from which activation energies (E_a) of 43.1 kJ mol^{-1} and 44.9 kJ mol^{-1}, respectively, were derived. These values are comparable to those of [bmim][Tf_2N] (31.3 kJ mol^{-1})[12] and [Fe($C_5H_4{}^nBu$)(C_5H_5)][Tf_2N] (38.8 kJ mol^{-1}).[2] The Vogel–Tammann–Fulcher (VTF) equation ($\eta = \eta_0 \exp[DT_0/(T–T_0)]$)[13] was also used to fit the data, where T_0 is the ideal glass transition temperature and D is a parameter that shows deviation from Arrhenius behavior. The values T_0 and D obtained for [**C6Fc**][Tf_2N] were –57.2 °C and 1.76, and those for [**C10Fc**][Tf_2N] were –53.6 °C and 1.63, respectively. The small D values, which are even smaller than that of [bmim][Tf_2N] (D = 4.65),[14] suggest that they are strongly fragile liquids.[15]

Crystal structures. The crystal structures of [**C3Fc**][Tf_2N], [**C4Fc**][PF_6], [**C6Fc**][X], and [**C10Fc**][X] (X = PF_6, NO_3) were determined at 173 K. Their packing diagrams are shown in Figure 7. [**C3Fc**][Tf_2N] belongs to space group $C2/c$, [**C4Fc**][PF_6] and [**C10Fc**][NO_3] belong to $P\bar{1}$, and the others belong to $P2_1/c$. In the alkyl chains of the salts, the C–C bond adjacent to the Cp ring exhibited the *gauche* conformation, whereas the other bonds exhibited the *trans* conformation. [**C4Fc**][PF_6] exhibited disorder in the alkyl chains. The intramolecular Fe–C(Cp) bond lengths, of which Fe–C_H was the shortest, were comparable to those of substituted octamethylferrocenium cations.[16] In all the salts, the C_5 axes of the ferrocenium moieties were aligned in nearly the same direction in the crystal. Weak hydrogen bonds were formed in the NO_3 and PF_6 salts between the ring hydrogen of the cation and the oxygen or fluorine atom in the anion (Figure 8). The CH...X (X = O or F) distances were shorter than the van der Waals distances by 0.15–0.36 Å. The Tf_2N salts exhibited no such contacts.

The packing arrangements of the salts depended on the alkyl chain length in the cation. In the salts with short alkyl chains ([**C3Fc**][Tf_2N] and [**C4Fc**][PF_6]), the anions and cations are packed alternately in the unit cell (Figures 7a–b). [**C4Fc**][Tf_2N] also exhibited a similar structure (*vide infra*). In contrast, lamellar structures are formed in the salts with longer alkyl chains ([**C6Fc**][X] and [**C10Fc**][X]; X = PF_6, NO_3) (Figures 7c–f). In these crystals, the anions and cations are arranged alternately to form layers, which are stacked with their alkyl chains extending outside the layers. The alkyl chains are in contact with each other between the layers and there are no direct π–π interactions between the cations. The interlayer distances in [**C10Fc**][X] are longer than those in [**C6Fc**][X] as a result of the longer alkyl chains. In the salts, except for [**C10Fc**][NO_3], the C_5 axes of the ferrocenium moieties are aligned parallel to the stacking direction of the layers. The difference between the packing patterns of the long chain and short chain salts, giving different lattice entropies, accounts for the observed different tendencies of the phase change entropies. A similar phenomenon has been observed in cobaltocenium salts.[17] Although the crystal structures of the Tf_2N salts with

long alkyl chains were not determined, it is likely that the Tf_2N salts with $n \geq 8$ form lamellar structures, considering the tendency of the phase transition entropies in Figure 5.

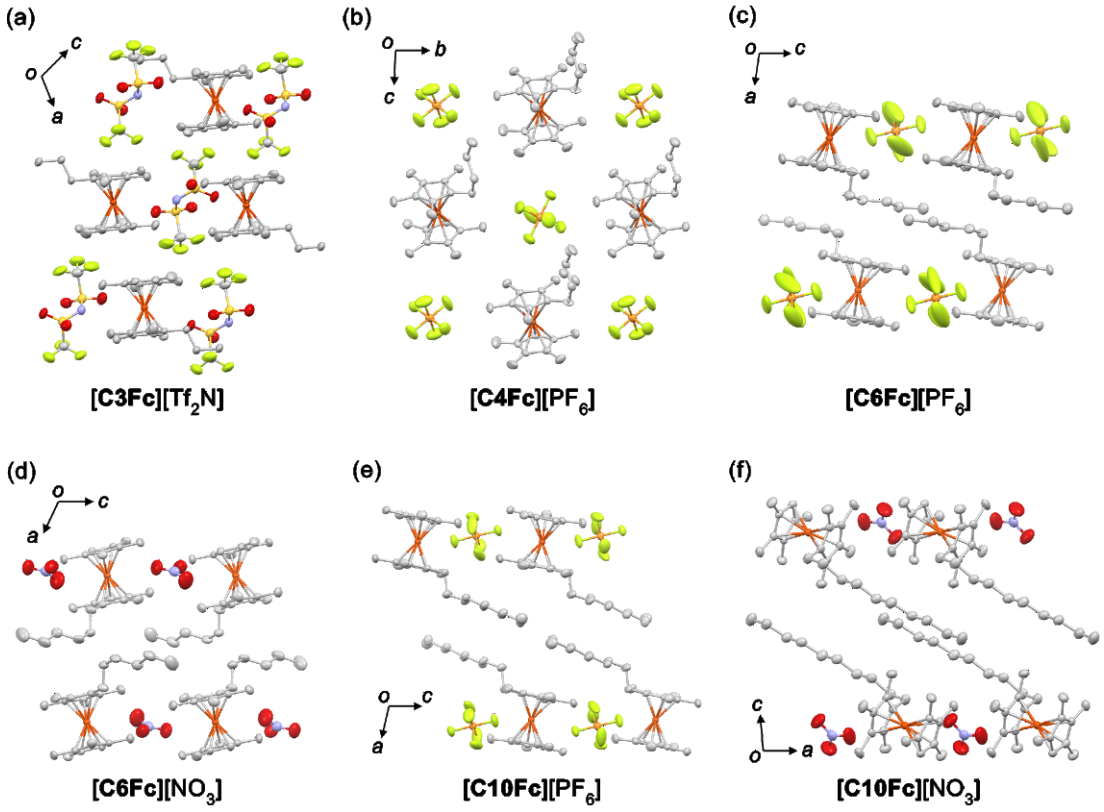

Figure 7. Packing diagrams of (a) [**C3Fc**][Tf_2N], (b) [**C4Fc**][PF_6], (c) [**C6Fc**][PF_6], (d) [**C6Fc**][NO_3], (e) [**C10Fc**][PF_6], and (f) [**C10Fc**][NO_3]. Hydrogen atoms have been omitted for clarity.

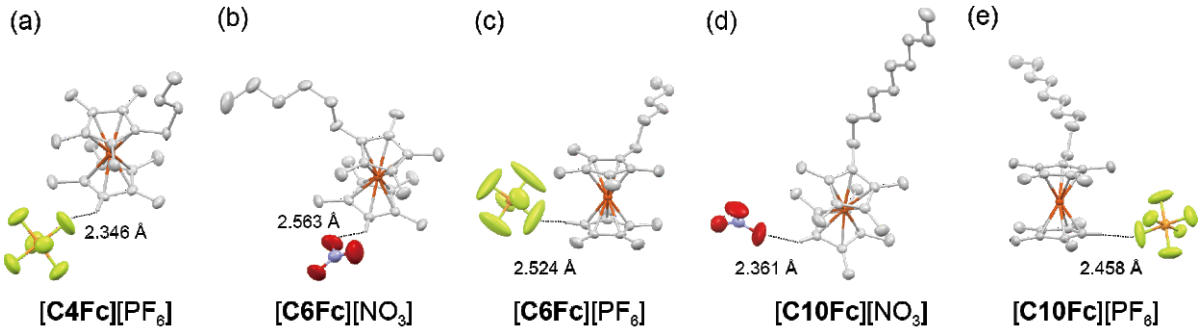

Figure 8. Molecular structures of (a) [**C4Fc**][PF_6], (b) [**C6Fc**][NO_3], (c) [**C6Fc**][PF_6], (d) [**C10Fc**][NO_3], and (e) [**C10Fc**][PF_6]. C–H...X contacts are indicated by dotted lines.

Magnetic properties of [C4Fc][Tf_2N]. The Tf_2N salts are paramagnetic ionic liquids containing magnetically anisotropic paramagnetic cations. We investigated the effects of magnetic fields on their crystallization. A remarkable effect was found in [**C4Fc**][Tf_2N]. This salt was paramagnetic in the measured temperature range of 2–330 K. The susceptibility around room temperature is shown in Figure 9. The χT value in the liquid state (0.78 emu K mol^{-1}), which is typical of ferrocenium cations, is larger than the spin-only value because of the orbital contribution.[18] When the liquid was cooled under 0.5 T (Figure 9, open circles), a significant increase in the susceptibility was observed in association with solidification at 299 K. Heating the solid led to melting at a higher temperature, 309 K, where the magnetic susceptibility decreased and returned to the initial value. Thus, the magnetic response accompanies the thermal hysteresis based on phase changes. Under 0.1 T, however, only a small change was observed at the phase change (Figure 9, filled circles). A similar magnetic response was also found in a ferrocenium ionic liquid [$Fe(C_5H_4Et)_2$][Tf_2N],[2b] albeit with less reproducibility and controllability.

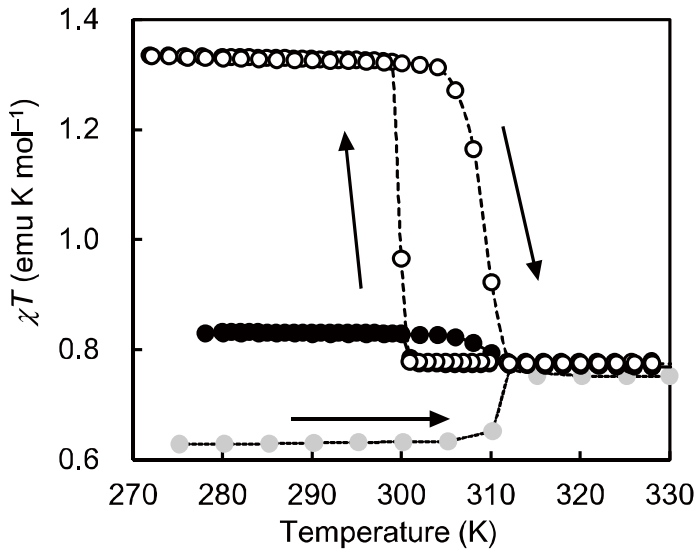

Figure 9. Temperature dependence of the magnetic susceptibilities of [**C4Fc**][Tf_2N] in the form of a χT–T plot. The data measured under 0.1 T and 0.5 T are shown by filled circles and open circles, and those for a sample crystallized under a perpendicular field of 0.59 T are shown by gray circles (heating run).

To confirm the magnetic orientation of the field-cooled sample, we investigated the details of the phenomenon. First, the detailed field dependence of the magnetic susceptibility changes was investigated, the results of which are plotted in Figure 10 (open circles). The value increases as a function of the magnetic field, exhibiting saturation above 2 T. Therefore, the material can record the applied magnetic field up to about 1 T. The dependencies of the magnetic susceptibility on the temperature and magnetic field were independent of the scan rate in the range of 0.5–10 K min^{-1}. When quartz wool (14 wt.%) was added to the liquid sample to inhibit magnetic orientation during solidification, the susceptibility change $\Delta\chi T$ was effectively suppressed (Figure 10, filled circles). The magnetic field affected the susceptibility increase, which increased with increasing field strength, but not the phase transition temperature.

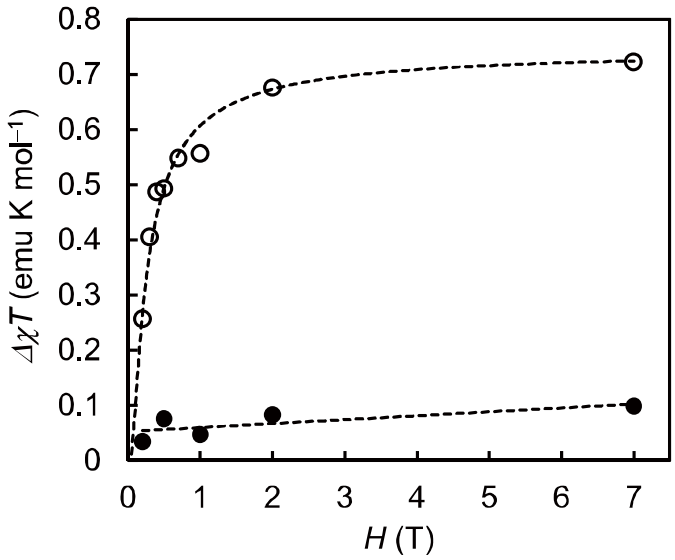

Figure 10. Magnetic susceptibility changes of **1** ($\Delta\chi T = \chi T_{270\ K} - \chi T_{310\ K}$) plotted as a function of magnetic field strength (open circles). Data are also shown for a sample filled with quartz wool (filled circles).

We next measured the anisotropy of the magnetic susceptibility. A liquid sample of [**C4Fc**][Tf_2N] was crystallized under a magnetic field of 0.59 T, and the magnetic susceptibility (χT value) of this sample measured under a perpendicular field was 0.63 emu K mol^{-1} (Figure 9, gray circles), which was smaller than that in the liquid state, whereas the value measured under the parallel field increased. This result directly demonstrates that the orientation of the crystal is controlled by the direction of the magnetic field.

The magnetic susceptibility of [**C4Fc**][Tf_2N] solidified under a field of 0.8 T was 1.36 emu K mol^{-1} when measured under a parallel field, whereas the value for a fully oriented sample is calculated to be 1.73 emu K mol^{-1}, using $\chi T = [g^2 S(S+1)]/8$, where $g_{//} = 4.3$ (*vide infra*) and $S = 1/2$. Assuming that there are only two components in the sample, fully oriented fraction and non-oriented isotropic fraction, the ratio of the former fraction was calculated to be 0.61 from the susceptibility values.

The magnetic orientation was further investigated using ESR spectroscopy. In the ESR spectra of an oriented polycrystalline sample crystallized under 0.8 T, a sharp, symmetrical peak was observed below 40 K for a parallel orientation of the magnetic fields for crystallization and ESR measurements (Figure 11a). In contrast, asymmetric peaks typical of a non-oriented material were observed for the sample crystallized without magnetic fields (Figure 11b). Furthermore, a clear angular dependence was observed in the ESR spectra of the oriented sample recorded at 3.8 K, as shown in Figure 12a. An upfield shift and broadening of the peak were observed with increasing angle (θ) between the magnetic fields for the measurement and crystallization. The $g_{//}$ component along the C_5 axis of the cation is observed for $\theta = 0°$, and the $g_{\perp}$ component appears with sample rotation. The small residual peak of the $g_{//}$ component observed even for $\theta = 90°$ is a non-oriented fraction. Thus, the spectrum for each rotation angle contains the angular-dependent component of the oriented fraction and angular-independent component of the isotropic fraction (Figure 13). The *g*-values obtained by fitting the angular dependence (Figure 12b) were $g_{//} = 4.3$, $g_{\perp} = 1.7$, and g_{av} =

2.84, which are comparable to the typical values for ferrocenium salts such as $[Fe(C_5Me_5)_2][PF_6]$ ($g_{//}$ = 4.43, $g_{\perp}$ = 1.35, $g_{av.}$ = 2.78) and $[Fe(C_5Me_4H)_2][BF_4]$ ($g_{//}$ = 4.11, $g_{\perp}$ = 1.42, $g_{av.}$ = 2.64).[18] The average *g*-value calculated form the χT value in the liquid state (0.78 emu K mol^{-1}) was 2.87, which is in good agreement with the analysis. The linewidths and intensities of the $g_{//}$ and $g_{\perp}$ peaks were obtained by fitting the spectra, and then the peak areas of the angle-dependent and independent components were calculated from the simulated spectra for θ = 0° and θ = 90°, respectively. The ratio of the former component, which corresponds to the ratio of the oriented fraction, was 0.6. The value is again in good agreement with that estimated from the magnetic susceptibility data (0.61) as shown above.

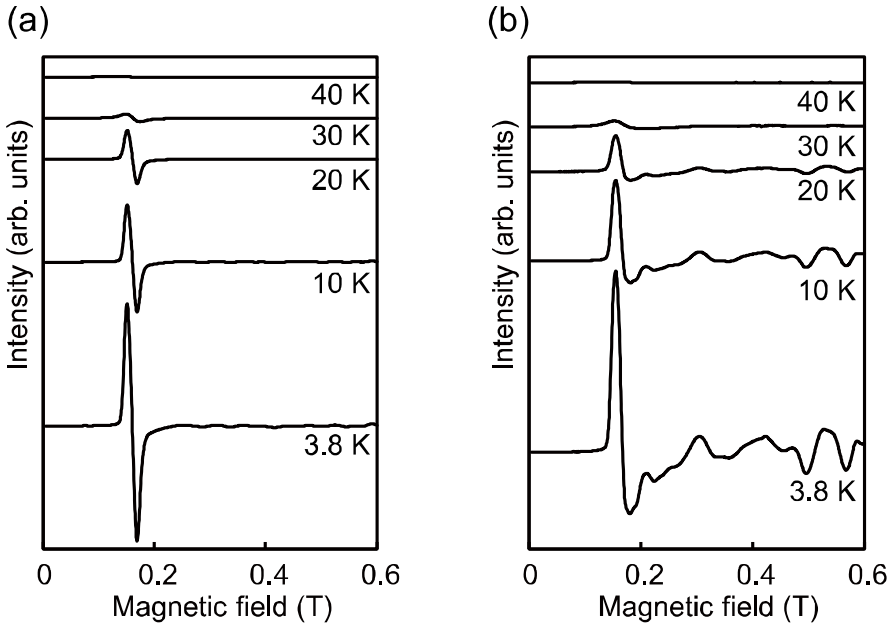

Figure 11. Temperature dependences of ESR spectra of [**C4Fc**][Tf_2N] crystallized (a) under a magnetic field of 0.8 T and (b) without a magnetic field.

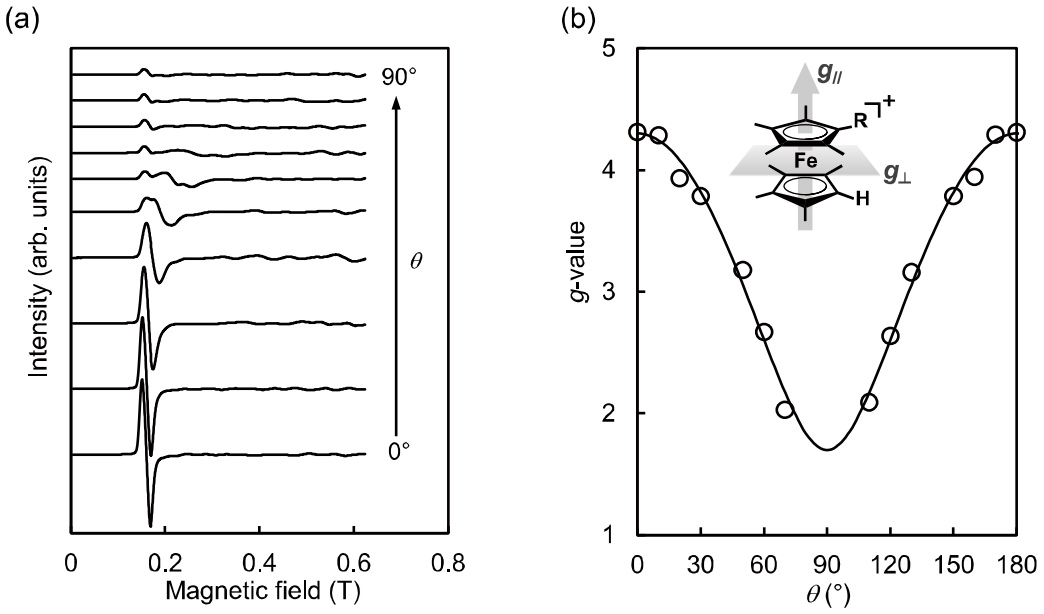

Figure 12. (a) Angular dependence of ESR spectra recorded at intervals of 10° and (b) the angular dependences of *g*-value at 3.8 K, measured on a sample of [**C4Fc**][Tf_2N] crystallized under a magnetic field of 0.8 T. θ is defined as the angle between the magnetic fields used for crystallization and ESR measurements.

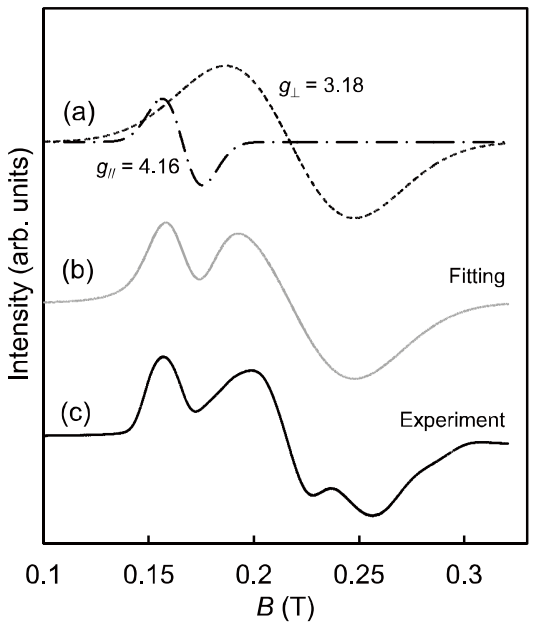

Figure 13. (a) ESR spectra of [**C4Fc**][Tf_2N] crystallized under a magnetic field of 0.8 T recorded at 3.8 K (θ = 50°). (b), (c) Simulated spectra (dotted line: oriented component; broken line: nonoriented component).

Mechanism of magnetic orientation in [C4Fc][Tf_2N]. For magnetic orientation to occur, it is important that the crystal structure is magnetically anisotropic. Therefore, the molecular arrangement of [**C4Fc**][Tf_2N] in the solid state was determined at 100 K (Figure 14). In the unit cell, the C_5 axes of ferrocenium cations are aligned parallel to the *c*-axis. Given that the largest principal value of the *g*-tensor of a ferrocenium cation is along its C_5 axis,[19] this arrangement produces the largest magnetic susceptibility along the *c*-axis. The direction of the magnetic orientation was further investigated using powder X-ray diffraction (XRD) measurements. A liquid sample of [**C4Fc**][Tf_2N] was placed on a glass plate and crystallized under the magnetic field (0.36 T) of a neodymium magnet placed below the plate. The XRD patterns showed a significant increase in the intensity of the peaks at $2\theta =$ 13°, 14.5°, and 23° for the out-of-plane measurement compared with that of an unoriented sample (Figure 15), but the crystal structure was unchanged by the magnetic field. The peak at $2\theta =$ 14.5° was indexed as (200), which shows that the *a*-axis, along which the C_5 axis of the cation is oriented, is oriented along the magnetic field, in agreement with the magnetic anisotropy of the crystal. In repeated experiments on the oriented samples, differences were observed in the relative peak intensities; this results from an in-plane distribution of the growth direction.

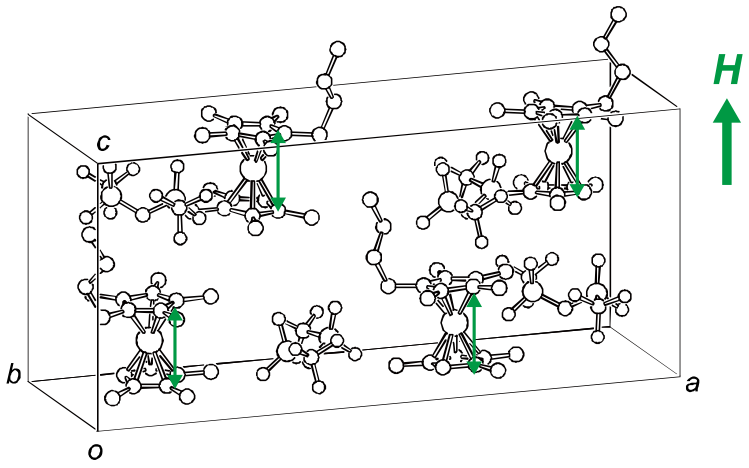

Figure 14. Crystal structure of [**C4Fc**][Tf_2N] at 100 K. This figure also illustrates the direction of the field orientation of the crystal with respect to the external field (*H*) indicated by a large arrow. Directions of the largest magnetic susceptibility component of the ferrocenium cations are indicated by small arrows on each molecule.

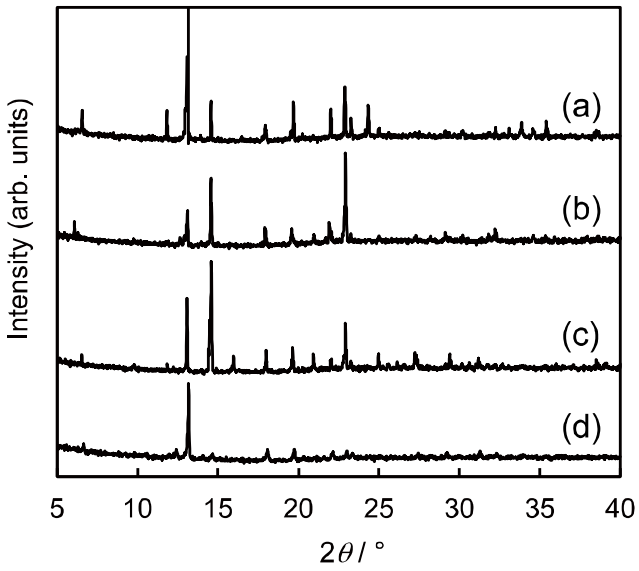

Figure 15. Powder XRD patterns of [**C4Fc**][Tf_2N] crystallized under a magnetic field of 0.36 T (a–c) and without a magnetic field (d).

The crystal growth pattern on the surface accompanying radial distribution was visually observable under a polarized optical microscope. Figure 16a shows the POM image of a liquid of [**C4Fc**][Tf_2N] on a glass plate at room temperature. Solidification of the liquid in the absence of magnetic fields resulted in the formation of microscopic domains (Figure 16b). However, under a magnetic field of permanent magnets (0.6 T), the liquid crystallized into needles arranged perpendicular to the field (Figure 16c).

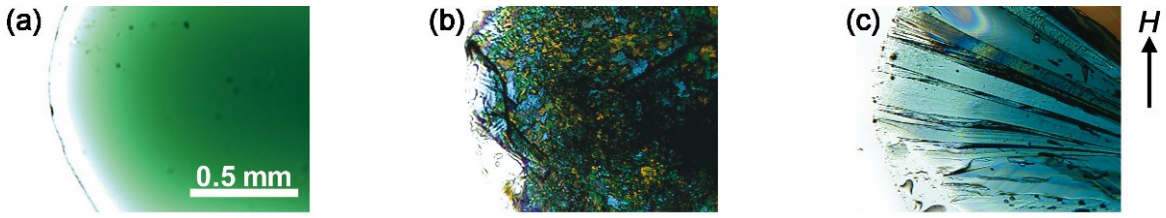

Figure 16. Polarized optical microscopy images of [**C4Fc**][Tf_2N] under plain-polarized light on a glass plate at RT. (a) Liquid state, (b) after solidification without magnetic field, and (c) after solidification under a magnetic field of 0.6 T applied parallel to the surface.

The effect of sample shape on the magnetic response was also investigated. For liquid samples in fine tubes (inner diameter 0.2 mm) or in the form of thin layers (thickness 0.5 μm), no magnetic orientations were observed, even under 7 T. Magnetic orientation was also inhibited by adding quartz wool to the liquid (*vide ante*). In these circumstances, the orientation of the crystal growth may be affected largely by the surface rather than by the external fields. These results indicate that magnetic orientation is a bulk property, and that the phenomenon is not attributable to the orientation of independent molecules, but is more likely a result of orientation of the crystal nucleus or crystal growth direction during crystallization. This seems to be consistent with the less controllable response in a ferrocenium ionic liquid, $[Fe(C_5H_4Et)_2][Tf_2N]$, with a much lower viscosity than the present salt,[2b] because the slower crystallization of high-viscosity liquids may lead to better magnetic-field orientation. There might be a critical size of crystal nucleus for magnetic orientation, and further investigations may be needed to explore its microscopic mechanism. The above results unfortunately suggest that the fabrication of thin-layer magnetic memory devices based on this mechanism is unfeasible.

Magnetic properties of [C5'Fc][Tf_2N] and [C12Fc][Tf_2N]. In contrast to [**C4Fc**][Tf_2N], no significant magnetic orientation was observed in [**C5'Fc**][Tf_2N] and [**C12Fc**][Tf_2N]. The magnetic susceptibility of [**C5'Fc**][Tf_2N] increased by only 0.05 emu K mol^{-1} (0.73 emu K mol^{-1}) upon crystallization at −16 °C under 2 T (Figure 17), and, with heating, the value returned to the liquid value at 57 °C. Although the crystal structure is unknown, the negligible magnetic change can probably be ascribed to the small magnetic anisotropy of the crystal, if any.

When [**C12Fc**][Tf_2N] was cooled from the liquid phase, it crystallized into a disordered phase at 25 °C, which further exhibited a phase transition in the solid state at around 7 °C. The temperature dependences of the magnetic susceptibility upon cooling under 0.5 T, 1 T, and 7 T are shown in Figure 18. Repeated experiments showed that this salt exhibited small, random changes of the χT

values at the phase transitions, but the direction of the change was random, indicating that no orientation is caused by the magnetic fields. The χT value in the liquid state was 0.76 emu K mol^{-1}, which increased or decreased by less than 0.05 emu K mol^{-1} upon crystallization, and the value further increased or decreased by about 0.1 emu K mol^{-1} at the solid phase transition temperature. The absence of magnetic orientation in this salt is probably correlated with the rotational motion of the ferrocenium moiety, probably present in the disordered phase, which reduces the magnetic anisotropy of the crystal. The larger change in susceptibility observed at the solid phase transition is ascribed to the increased magnetic anisotropy of the crystal caused by ordering of the cation. In the solid phase transition, the orientations of the cations are fixed according to the crystal lattice, hence they are not affected by magnetic fields.

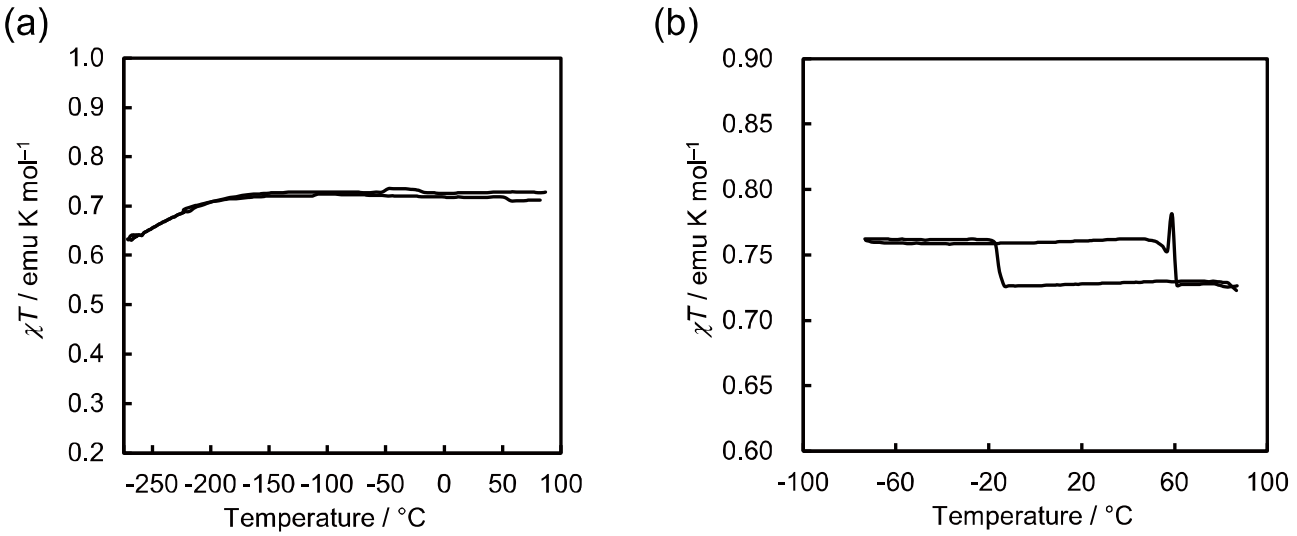

Figure 17. Temperature dependences of magnetic susceptibilities of [**C5'Fc**][Tf_2N] measured under (a) 0.1 T and (b) 2 T at a scan rate of 2 K min^{-1}.

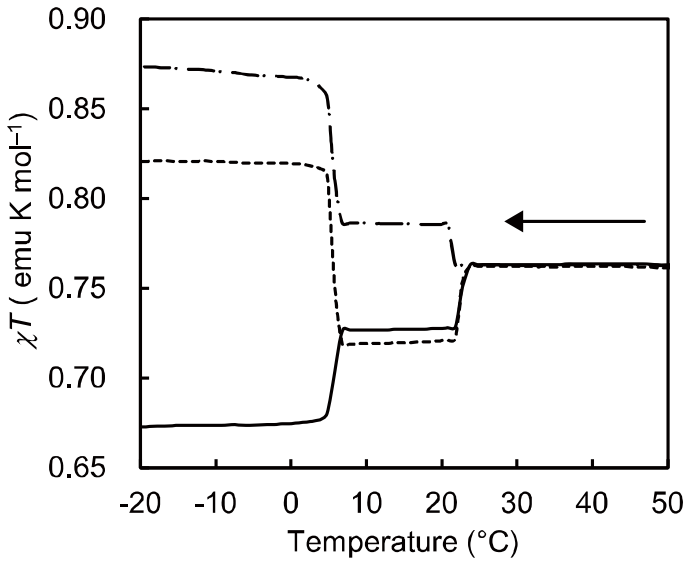

Figure 18. Temperature dependences of magnetic susceptibilities of [**C12Fc**][Tf_2N] in the form of χT–T plots, measured under 0.1 T (dotted line), 1 T (solid line), and 7 T (broken line) in the cooling processes.

These results show that not all ferrocenium ionic liquids show a magnetic orientation effect, despite the magnetic anisotropy of the molecule, and that the phenomenon is instead related to the crystal properties. The orientation mechanism is therefore significantly different from the well-known magnetic orientation of diamagnetic liquid crystal molecules. The magnetic-field alignments of materials upon solidification have attracted much interest,[20] and magnetic susceptibility changes coupled with a liquid–solid transformations have also been observed in several molecular materials such as paramagnetic ionic liquids[21] and a solid composed of radical dimers.[22] The magnetic orientation of metallomesogens coupled with a phase transition to a liquid crystalline phase is an interesting phenomenon.[23] In [**C4Fc**][Tf_2N], the magnetic orientation occurs near room temperature with hysteresis and with a large susceptibility change, the degree of which can be controlled by the strength of the applied field. These are unique magnetic switching properties not seen in other materials.

4.3 Conclusion

A series of alkyloctamethylferrocenium salts with Tf_2N, PF_6, and NO_3 anions ($[Fe(C_5Me_4C_nH_{2n+1})(C_5Me_4H)][X]$) were prepared. Investigation of their thermal properties, phase transition behaviors, and crystal structures revealed the following. The Tf_2N salts are ionic liquids that are stable under air. The alkyl chain length dependences of the melting points are similar to those observed for ionic liquids of alkylimidazolium salts. Most of the salts exhibit phase transitions in the solid state. In the salts with short alkyl chains, the sum of the phase change entropies is nearly constant, whereas the salts with longer alkyl chains display an entropy increase with elongation of the alkyl chain. Crystal structure determinations revealed that the short chain salts exhibit alternate stacking of cations and anions, whereas the long chain salts form lamellar structures, where the alkyl chains are aligned between the layers. The effect of magnetic fields on crystallization of the Tf_2N salts was investigated in detail. The magnetic orientation phenomenon in the salt with $n = 4$ upon crystallization originates from the magnetic anisotropy of the crystal structure, which is a bulk property. Further investigation of these functional liquids should lead to novel molecular electronic applications.

4.4 Experimental Section

General. Octamethylformylferrocene[24] and silver bis(trifluoromethylsulfonyl)amide ($Ag[Tf_2N]$)[25] were synthesized according to literature methods. Other reagents and solvents were commercially available. ^1H NMR spectra were recorded using a JEOL JNM-ECL-400 spectrometer. Elemental analyses were performed using a Yanaco CHN MT5 analyzer. DSC measurements were performed using a TA Instrument Q100 calorimeter in the temperature range –180 to 210 °C at a rate of 10 K min^{-1}. The viscosities of the liquids were measured under N_2 atmosphere using a Toki Sangyo TV-22 viscometer with a 3° × R7.7 cone rotor, in the temperature range 14–36 °C. XRD data for the powder samples were recorded on a Rigaku SmartLab diffractometer using Cu Kα radiation

(λ = 1.54056 Å). ESR spectra were recorded on an X-band JEOL TE-260 spectrometer in the temperature range 3.8 to 40 K. For the ESR measurements, a powder sample of [**C4Fc**][Tf_2N] was loaded into a quartz tube, which was sealed under nitrogen, and the sample was heated to melt it. The field-oriented samples were prepared by cooling the sample to crystallize under the magnetic field of the ESR magnet (0.8 T). The non-oriented samples were obtained by the same procedure, without applying magnetic fields.

Propyloctamethylferrocene (C3Fc). *(a) 1-Hydroxypropyloctamethylferrocene.* All the manipulations were carried out under a nitrogen atmosphere. Ethyl bromide (1.0 mL, 12.8 mmol) was added dropwise to a stirred mixture of magnesium turnings (0.330 g, 13.6 mmol) and ether (15 mL), and the solution was stirred until most of the magnesium dissolved. The Grignard reagent thus prepared was added slowly to a solution of octamethylformylferrocene (0.30 g, 1.0 mmol) in dry THF (20 mL) cooled at –78 °C, and the solution was stirred for 30 min. The reaction mixture was quenched at –78 °C with saturated NH_4Cl solution (20 mL) and extracted with ether. The organic layer was dried over magnesium sulfate and concentrated under reduced pressure. The crude product was purified by column chromatography (silica, CH_2Cl_2). The product was obtained as a yellow solid (0.324 g, 99.9% yield). ^{1}H NMR (400 MHz, $CDCl_3$, TMS): δ = 0.89 (t, 3H, J = 7.6 Hz), 1.69–1.89 (m., 26H), 2.33 (s, 2H), 3.55 (s, 1H), 4.28 (t, 1H, J = 7.0 Hz). *(b) Propyloctamethylferrocene.* A solution of $BH_3 \cdot SMe_2$ (6.3 mmol) in THF (3.0 mL, 2 m solution) was added to a stirred solution of 1-hydroxypropyloctamethylferrocene (0.320 g, 0.90 mmol) in THF (15 mL). After refluxing the solution for 1 h, the reaction was quenched with aqueous NH_4Cl (20 mL), and the solution extracted with CH_2Cl_2. The organic layer was dried over magnesium sulfate and concentrated under reduced pressure. The crude product was purified by column chromatography (alumina, pentane). The product was obtained as a yellow oil (0.253 g, yield 82.8%). ^{1}H NMR (400 MHz, $CDCl_3$, TMS): δ = 0.90 (t, 3H, J = 7.6 Hz), 1.29 (q, 4H, J = 7.5 Hz), 1.65–1.73 (br, 24H), 2.17 (t, 2H, J = 7.4 Hz), 3.21 (s, 1H).

The other alkyloctamethylferrocenes were prepared in a similar manner, and *trans*-1-pentenyl octamethylferrocene was obtained by dehydration of 1-hydroxypentyloctamethylferrocene.

Butyloctamethylferrocene (C4Fc). *(a) 1-Hydroxybutyloctamethylferrocene.* Yellow-orange solid, 78.4% yield. *(b) Butyloctamethylferrocene.* Yellow oil, 70.0% yield. ^{1}H NMR (400 MHz, $CDCl_3$, TMS); δ = 0.88 (t, 3H, *J* = 7.2 Hz), 1.25–1.30 (m, 4H), 1.65 (s, 3H), 1.72 (m, 18H), 2.18 (t, 2H, *J* = 7.6 Hz), 3.21 (s, 1H). Anal. Calcd (%) for $C_{22}H_{34}Fe$ (354.4): C, 74.57; H, 9.67. Found: C, 74.37; H, 9.77.

Pentyloctamethylferrocene (C5Fc). *(a) 1-Hydroxypentyloctamethylferrocene.* Yellow-orange solid, 72.6% yield. *(b) Pentyloctamethylferrocene.* Yellow oil, 64.5% yield. ^{1}H NMR (400 MHz, $CDCl_3$, TMS): δ = 0.88 (t, 3H, *J* = 6.8 Hz), 1.29 (br, 6H), 1.63–1.70 (br, 24H), 2.14 (s, 2H), 3.23 (s, 1H). Anal. Calcd (%) for $C_{23}H_{36}Fe$ (368.4): C, 74.99; H, 9.85. Found: C, 74.58; H, 9.96.

Hexyloctamethylferrocene (C6Fc). *(a) 1-Hydroxyhexyloctamethylferrocene.* Yellow solid, 90% yield. ^{1}H NMR (400 MHz, $CDCl_3$, TMS): δ = 0.87 (t, 3H, *J* = 6.8 Hz), 1.26 (br, 6H), 1.43 (br, 2H), 1.65–1.76 (m, 21H), 1.90 (s, 3H), 2.31 (s, 1H), 3.55 (s, 1H), 4.40 (br, 1H). *(b) Hexyloctamethylferrocene.* Yellow oil, 90% yield. ^{1}H NMR (400 MHz, $CDCl_3$, TMS): δ = 0.87 (t, 3H, *J* = 6.8 Hz), 1.29 (br, 8H), 1.65 (s, 6H), 1.73 (m, 18H), 2.17 (t, 2H, *J* = 7.2 Hz), 3.20 (s, 1H). Anal. Calcd (%) for $C_{24}H_{38}Fe$ (382.4): C, 75.38; H, 10.02. Found: C, 75.39; H, 10.13.

Octyloctamethylferrocene (C8Fc). *(a) 1-Hydroxyoctyloctamethylferrocene.* Yellow solid, 76.5% yield. ^{1}H NMR (400 MHz, $CDCl_3$, TMS): δ = 0.88 (t, 3H, *J* = 6.8 Hz), 1.25 (br, 8H), 1.43 (br, 2H), 1.68–1.76 (m, 21H), 1.89 (s, 3H), 2.31 (s, 1H), 3.55 (s, 1H), 4.35 (br, 1H). *(b) Octyloctamethyl ferrocene.* Yellow oil, 83% yield. ^{1}H NMR (400 MHz, $CDCl_3$, TMS): δ = 0.88 (t, 3H, *J* = 6.8 Hz), 1.26 (br, 12H), 1.66 (s, 6H), 1.73 (m, 18H), 2.18 (br, 2H), 3.21 (s, 1H). Anal. Calcd (%) for $C_{26}H_{42}Fe$ (382.4): C, 76.08; H, 10.31. Found: C, 76.01; H, 10.32.

Decyloctamethylferrocene (C10Fc). *(a) 1-Hydroxydecyloctamethylferrocene.* Yellow oil. ^{1}H NMR (400 MHz, $CDCl_3$, TMS): δ = 0.89 (t, 4.3H, *J* = 6.2 Hz), 1.26 (br, 18H), 1.43 (br, 2H),

1.69–1.76 (m, 21H), 1.89 (s, 3H), 2.31 (s, 1H), 3.55 (s, 1H), 4.35 (br, 1H). The crude product was used for the next step without purification. (*b) Decyloctamethylferrocene.* Yellow oil. ^{1}H NMR (400 MHz, $CDCl_3$, TMS): δ = 0.88 (t, 4.4H, J = 6.8 Hz), 1.26 (br, 22H), 1.68 (s, 6H), 1.73 (m, 18H), 2.18 (t, 2H, J = 7.4 Hz), 3.20 (s, 1H). The crude product was used for the salt preparation without purification.

Dodecyloctamethylferrocene (C12Fc) *(a) 1-Hydroxydodecyloctamethylferrocene.* Yellow solid, 48.5% yield (crude). The crude product was used for the next step without purification. *(b) Dodecyloctamethylferrocene.* Yellow oil, 71% yield (crude). ^{1}H NMR (400 MHz, $CDCl_3$, TMS): δ = 0.88 (t, 3.4H, J = 6.8 Hz), 1.25 (br, 22H), 1.63–1.70 (m, 24H), 2.14 (br, 2H), 3.22 (s, 1H). The crude product was used for the salt preparation without purification.

Heptadecyloctamethylferrocene (C17Fc). *(a) 1-Hydroxyheptadecyloctamethylferrocene.* Yellow solid. The crude product was used for the next step without purification. (*b) Heptadecyloctamethylferrocene.* Yellow oil. The crude product was used for the salt preparation without purification.

***trans*-1-Pentenyloctamethylferrocene (C5'Fc).** 1-Hydroxypentyloctamethylferrocene (0.531 g), prepared similarly, was distilled under vacuum at 130 °C to give the product within an hour as a dark-brown oil (0.268 g, 53%). ^{1}H NMR (400 MHz, $CDCl_3$, TMS): δ = 0.94 (m, 3H), 1.47 (m, 2H), 1.65 (s, 6H), 1.70 (s, 6H), 1.77 (s, 6H), 1.86 (s, 6H), 2.11 (m 2H), 3.55 (s, 1H), 5.87 (m, 1H), 6.04 (d, 1H, J = 16.0 Hz). Anal. Calcd (%) for $C_{23}H_{34}Fe$ (354.4): C, 75.40; H, 9.35. Found: C, 75.34; H, 9.44.

[C3Fc][Tf$_2$N]. In the dark, Ag[Tf$_2$N] (0.232 g, 0.60 mmol) was added to a solution of propyloctamethylferrocene (0.200 g, 0.59 mmol) in CH_2Cl_2 (10 mL). After stirring the solution for a few minutes, the mixture was filtered via a syringe equipped with a membrane filter to remove silver deposits and unreacted Ag[Tf$_2$N]. Removal of the solvent from the filtrate under reduced pressure gave the product as a dark-green solid (0.336 g, 92% yield), which was recrystallized from ethanol/hexane. Dark-green plate crystals. Anal. Calcd (%) for $C_{23}H_{32}F_6FeNO_4S_2$ (620.47): C, 44.52;

H, 5.20; N, 2.26. Found: C, 44.58; H, 5.23; N, 2.32. The other Tf_2N salts were prepared in a similar manner. For the purification of [**C10Fc**][Tf_2N] and [**C12Fc**][Tf_2N], they were dissolved in methanol and washed repeatedly with hexane to remove impurities. The solvents were evaporated under reduced pressure, and the residue was dried under vacuum at 80 °C for one day.

[C4Fc][Tf_2N]. Dark-green solid, 72% yield. ^{1}H NMR (400 MHz, $CDCl_3$, TMS): δ = 3.18 (s, 24H), 7.43 (br., 1H), 16.72 (br., 9H). Anal. Calcd (%) for $C_{24}H_{34}F_6FeNO_4S_2$ (634.5): C, 45.43; H, 5.40; N, 2.21. Found: C, 45.58; H, 5.50; N, 2.42.

[C5Fc][Tf_2N]. Dark-green oil, 99% yield. Anal. Calcd (%) for $C_{25}H_{36}F_6FeNS_2O_4$ (648.53): C, 46.30; H, 5.60; N, 2.16. Found: C, 46.51; H, 5.74; N, 2.13.

[C5'Fc][Tf_2N]. Dark-green powder, 79% yield. Anal. Calcd (%) for $C_{25}H_{34}F_6FeNO_4S_2$ (646.51): C, 46.44; H, 5.30; N, 2.17. Found: C, 46.54; H, 5.39; N, 2.26.

[C6Fc][Tf_2N]. Dark-green oil, 95% yield. Anal. Calcd (%) for $C_{26}H_{38}F_6FeNO_4S_2$ (662.55): C, 47.13; H, 5.78; N, 2.11. Found: C, 47.27; H, 5.87; N, 2.13.

[C8Fc][Tf_2N]. Dark-green oil, 98% yield. Anal. Calcd (%) for $C_{28}H_{42}F_6FeNO_4S_2$ (690.60): C, 48.70; H, 6.13; N, 2.03. Found: C, 48.52; H, 6.18; N, 2.13.

[C10Fc][Tf_2N]. Dark-green oil, 68.3% yield (total yield from octamethylferrocene). Anal. Calcd (%) for $C_{30}H_{46}F_6FeNO_4S_2$ (718.66): C, 50.14; H, 6.45; N, 1.95. Found: C, 49.91; H, 6.55; N, 2.02.

[C12Fc][Tf_2N]. Dark-green solid, 92% yield. Anal. Calcd (%) for $C_{32}H_{50}F_6FeNO_4S_2$ (746.71): C, 51.47; H, 6.75; N, 1.88. Found: C, 51.44; H, 6.58; N, 1.98.

[C17Fc][Tf_2N]. Dark-green solid, 38.3% yield (total yield from octamethylferrocene). Anal. Calcd (%) for $C_{37}H_{60}F_6FeNO_4S_2$ (816.84): C, 54.40; H, 7.40; N, 1.71. Found: C, 54.18; H, 7.46; N, 1.96.

[C4Fc][PF_6]. In the dark, a solution of Ag[PF_6] (51 mg, 0.20 mmol) in acetone (5 mL) was added to a solution of butyloctamethylferrocene (55 mg, 0.16 mmol) in acetone (10 mL). After stirring the solution for a few minutes, the mixture was filtered via a syringe equipped with a

membrane filter to remove silver deposits and unreacted $Ag[PF_6]$. Removal of the solvent from the filtrate under reduced pressure gave a solid, which was dissolved in CH_2Cl_2 (10 mL) and washed with water. After drying the organic phase over magnesium sulfate, removal of the solvent gave the product as a dark-green solid (57 mg, 74% yield), which was recrystallized from ethanol (–50 °C). Green plate crystals. Anal. Calcd (%) for $C_{22}H_{34}FeF_6P$ (499.31): C, 52.62; H, 6.72. Found: C, 52.92; H, 6.86. The other PF_6 salts were prepared in a similar manner to that described above.

[C6Fc][PF_6]. Green plate crystals, 93% yield. Anal. Calcd (%) for $C_{24}H_{38}FeF_6P$ (527.37): C, 54.66; H, 7.26. Found: C, 54.45; H, 7.26.

[C10Fc][PF_6]. Green plate crystals, 63.3% yield. To remove impurities, the product was dissolved in methanol and washed repeatedly with hexane. Anal. Calcd (%) for $C_{28}H_{46}FeF_6P$ (583.47): C, 57.67; H, 7.95. Found: C, 57.35; H, 7.79.

[C6Fc][NO_3]. In the dark, a solution of $Ag[NO_3]$ (32 mg, 0.18 mmol) in water (2 mL) was added to a solution of hexyloctamethylferrocene (50 mg, 0.13 mmol) in acetone (2 mL) under stirring. After stirring for a few minutes, silver deposits and unreacted $Ag[NO_3]$ were removed by filtration. The solvent was evaporated under reduced pressure, and the residue was dissolved in CH_2Cl_2 (50 mL) and washed with water (50 mL). The organic layer was dried over magnesium sulfate, and evaporation of the solvent under reduced pressure gave the product as a green powder in 85% yield; it was recrystallized from acetone/ether/pentane (1:30:70). Green plate crystals. Anal. Calcd (%) for $C_{24}H_{36}FeNO_3$ (444.22): C, 64.86; H, 8.62; N, 3.15. Found: C, 64.52; H, 8.62; N, 3.24. The other nitrate salts were prepared in a similar manner.

[C10Fc][NO_3]. Green powder, 48% yield from octamethylferrocene. To remove impurities, the product was dissolved in methanol and washed repeatedly with hexane. The solvent was evaporated under reduced pressure, and the residue was dried under vacuum at 80 °C for one day. Anal. Calcd (%) for $C_{28}H_{46}FeNO_3$ (500.51): C, 67.19; H, 9.26; N, 2.80. Found: C, 66.01; H, 9.07; N, 2.74. Recrystallization from acetone/ether/pentane (1:30:70) gave a small amount of single crystals.

[C17Fc][NO_3]. Green powder, 57% yield from octamethylferrocene. Anal. Calcd (%) for $C_{35}H_{60}FeNO_3$ (598.70): C, 70.57; H, 10.20; N, 2.29. Found: C, 65.75; H, 9.93; N, 2.17.

Magnetic measurements. Magnetic measurements were carried out using a Quantum Design MPMS-XL7 SQUID susceptometer; 30–60 mg of samples were loaded in a quartz tube and used for the measurements. Samples of [**C4Fc**][Tf_2N] in confined spaces were prepared as follows. A glass capillary (inner diameter 0.2 mm, outer diameter 0.3–0.4 mm) was filled with a liquid sample of [**C4Fc**][Tf_2N] (11 mg), and cut into lengths of 5 mm. The short capillary-tubes were aligned and loaded into a quartz tube for SQUID measurements. To prepare thin-layer samples of thickness 25 μm, a liquid sample of [**C4Fc**][Tf_2N] was loaded into a quartz sample-tube, in which 200 sheets of spacers and separators prepared from copper TEM grids (diameter 3 mm, thickness 25 μm) were alternately carefully immersed. The magnetic susceptibility data were corrected for the diamagnetic contribution so that the χT values became constant in the high-temperature region. The data for [**C4Fc**][Tf_2N] and [**C5'Fc**][Tf_2N] were further corrected for a very small amount of ferromagnetic impurities (3×10^{-5} emu) from the magnetization curve.

X-ray structure determination. Single crystals for X-ray structure determination were obtained by recrystallization. [**C3Fc**][Tf_2N] and [**C4Fc**][Tf_2N] was recrystallized from ethanol at –14 °C, and [**C4Fc**][PF_6], [**C6Fc**][PF_6], and [**C10Fc**][PF_6] were obtained from ethanol at –50 °C. [**C6Fc**][NO_3] and [**C10Fc**][NO_3] were obtained by slow diffusion of ether/pentane into acetone solutions (acetone : ether : pentane = 1:30:70). XRD data were collected with a Bruker Smart1000 CCD diffractometer using Mo Kα radiation (λ = 0.71073 Å) at 173 K (cooling rate: 1 K min^{-1}). The structures were solved by direct methods and refined using SHELXTL.[26] The crystallographic data are listed in Tables 3–4. The crystallographic data for the structures have been deposited with the Cambridge Crystallographic Data Centre as supplementary publication nos. 900446 ([**C3Fc**][Tf_2N]), 775548 ([**C4Fc**][Tf_2N]), 900447 ([**C4Fc**][PF_6]), 900448 ([**C6Fc**][PF_6]), 900449 ([**C6Fc**][NO_3]), 900450 ([**C10Fc**][PF_6]), and 900451 ([**C10Fc**][NO_3]).

Table 3. Crystallographic parameters for [**C3Fc**][Tf_2N], [**C4Fc**][Tf_2N], [**C4Fc**][PF_6], and [**C6Fc**][PF_6].

	[**C3Fc**][Tf_2N]	[**C4Fc**][Tf_2N]	[**C4Fc**][PF_6]	[**C6Fc**][PF_6]
Empirical formula	$C_{23}H_{32}F_6FeNO_4S_2$	$C_{24}H_{34}F_6FeNO_4S_2$	$C_{22}H_{34}F_6FeP$	$C_{24}H_{38}F_6FeP$
Formula weight	620.49	634.49	499.31	527.36
Crystal system	Monoclinic	Orthorhombic	Triclinic	Monoclinic
Space group	*C*2/*c* (No. 15)	*P*na2$_1$ (No. 33)	*P*–1 (No. 2)	*P*2$_1$/*c* (No. 14)
a (Å)	16.389(3)	26.602(3)	12.6489(14)	16.0571(16)
b (Å)	18.944(3)	8.7735(9)	13.2409(15)	8.9074(9)
c (Å)	19.262(3)	11.9016(12)	13.8307(16)	17.6910(18)
α (°)			91.767(2)	
β (°)	113.192(2)		91.233(2)	96.246(2)
γ (°)			94.617(2)	
Volume (Å^3)	5497.1(16)	2777.8(5)	2307.1(5)	2515.3(4)
Z	8	4	4	4
d_{calcd} (g cm^{-3})	1.499	1.517	1.438	1.393
μ (mm^{-1})	0.771	0.765	0.777	0.717
Reflections collected	14 381	13711	12 027	12 924
Independent reflections	5195	4875	8005	4741
F(000)	2568	1316	1044	1108
Parameters	343	352	595	298
R_1[a], wR_2[b] ($I > 2\sigma(I)$)	0.0390, 0.1087	0.0237, 0.0596	0.0400, 0.1055	0.0641, 0.1901
R_1[a], wR_2[b] (all data)	0.0447, 0.1135	0.0248, 0.0602	0.0511, 0.1133	0.0772, 0.2038

[a] $R_1 = \Sigma||F_o| - |F_c||/\Sigma\,|F_o|$. [b] $wR_2 = [\Sigma w(F_o^2 - F_c^2)^2/\Sigma w(F_o^2)^2]^{1/2}$.

Table 4. Crystallographic parameters for [**C6Fc**][NO_3], [**C10Fc**][PF_6], and [**C10Fc**][NO_3].

	[**C6Fc**][NO_3]	[**C10Fc**][PF_6]	[**C10Fc**][NO_3]
Empirical formula	$C_{24}H_{38}FeNO_3$	C_{28} H_{46} F_6 Fe P	C_{28} H_{46} F_6 Fe P
Formula weight	444.40	583.47	500.51
Crystal system	Monoclinic	Monoclinic	Triclinic
Space group	$P2_1/c$ (No. 14)	$P2_1/c$ (No. 14)	$P\bar{1}$ (No. 2)
a (Å)	17.982(5)	19.6648(18)	8.0742(13)
b (Å)	8.762(2)	8.7837(8)	9.8377(16)
c (Å)	17.319(5)	17.5494(16)	17.596(3)
α (°)			90.473(2)
β (°)	115.567(4)	102.498(2)	92.713(3)
γ (°)			97.649(3)
Volume (Å^3)	2461.6(11)	2959.5(5)	1385.5(4)
Z	4	4	2
d_{calcd} (g cm^{-3})	1.199	1.310	1.201
μ (mm^{-1})	0.635	0.616	0.572
Reflections collected	11 578	15520	6926
Independent reflections	4324	5600	4763
F(000)	956	1236	542
Parameters	271	334	307
R_1[a], wR_2[b] ($I > 2\sigma(I)$)	0.0584, 0.1196	0.0392, 0.1061	0.0349, 0.1051
R_1[a], wR_2[b] (all data)	0.0808, 0.1296	0.0546, 0.1175	0.0403, 0.1083

[a] $R_1 = \Sigma||F_o| - |F_c||/\Sigma\,|F_o|$. [b] $wR_2 = [\Sigma w(F_o^2 - F_c^2)^2/\Sigma w(F_o^2)^2]^{1/2}$.

References

(1) (a) *Ferrocenes: Homogenous Catalysis, Organic Synthesis, Materials Science*, Eds. A. Togni, T. Hayashi, Wiley-VCH, Weinheim, **1995**, Chapter 8, and references therein; (b) D. De Caro, C. Faulmann, L. Valade, *Chem. Eur. J.*, **2007**, *13*, 1650–1663; (c) J. S. Miller, A. J. Epstein, W. M. Reiff, *Angew. Chem., Int. Ed. Engl.*, **1994**, *33*, 385–415; (d) J. S. Miller, *J. Mater. Chem.*, **2010**, *20*, 1846–1857.

(2) (a) T. Inagaki, T. Mochida, *Chem. Lett.*, **2010**, *39*, 572–573; (b) T. Inagaki, T. Mochida, M. Takahashi, C. Kanadani, T. Saito, D. Kuwahara, *Chem. Eur. J.*, **2012**, *18*, 6795–6804.

(3) S. Ulrich, *Polyhedron*, **1997**, *16*, 1513–1516.

(4) (a) R. Deschenaux, M. Schweissguth, A. -M. Levelut, *Chem. Commun.*, **1996**, 1275–1276; (b) R. Deschenaux, M. Schweissguth, M. -T. Vilches, A. -M. Levelut, D. Hautot, G. L. Long, D. Luneau, *Organometallics*, **1999**, *18*, 5553–5559.

(5) P. M. Dean, J. M. Pringle, D. R. MacFarlane, *Phys. Chem. Chem. Phys.*, **2010**, *12*, 9144–9153.

(6) T. Mochida, S. Saruta, unpublished result.

(7) (a) N. V. Plechkova, K. R. Seddon, *Chem. Soc. Rev.*, **2008**, *37*, 123–150; (b) H. Tokuda, K. Hayamizu, K. Ishii, M. A. B. H. Susan, M. Watanabe, *J. Chem. Phys. B*, **2005**, *109*, 6103–6110.

(8) D. Turnbull, M. H. Cohen, *Modern Aspect of the Vitreous State*, Butterworth, *Vol. 1*, London, **1960**, p. 38.

(9) O. Yamamuro, Y. Minamimoto, Y. Inamura, S. Hayashi, H. Hamaguchi, *Chem. Phys. Lett.*, **2006**, *423*, 371–375.

(10) J. Timmermans, *J. Phys. Chem. Solids*, **1961**, *18*, 1–8.

(11) (a) Y. U. Paulechka, A. V. Blokhin, G. J. Kabo, A. A. Strechan, *J. Chem. Thermodyn.*, **2007**, *39*, 866–877; (b) Y. Shimizu, Y. Ohte, Y. Yamamura, K. Saito, *Chem. Phys. Lett.*, **2009**, *470*, 295–299.

(12) A. Paul, A. Samanta, *J. Phys. Chem. B*, **2008**, *112*, 16626–16632.

(13) G. S. Fulcher, *J. Am. Ceram. Soc*., **1925**, *8*, 339–355.

(14) K. R. Harris, M. Kanakubo, L. A. Woolf, *J. Chem*. *Eng*. *Data*, **2007**, *52*, 1080–1085.

(15) C. A. Angell, *J. Non-Cryst. Solids*, **1985**, *73*, 1–17.

(16) H. Schottenberger, K. Wurst, R. H. Herber, *J. Organomet. Chem*. **2001**, *625*, 200–207.

(17) T. Mochida, Y. Funasako, T. Inagaki, M. -J. Li, K. Asahara, D. Kuwahara, *Chem. Eur. J.* **2013**, *19*, 6257–6264.

(18) J. S. Miller, D. T. Glatzhofer, D. M. O'Hare, W. M. Reiff, A. Chakraborty, A. J. Epstein, *Inorg. Chem.*, **1989**, *28*, 2930–2939.

(19) J. S. Miller, J. C. Calabrese, H. Rommelmann, S. R. Chittipeddi, J. H. Zhang, W. M. Reiff, A. J. Epstein, *J. Am. Chem. Soc.*, **1987**, *109*, 769–781.

(20) (a) P. De Rango, M. Lees, P. Lejay, A. Sulpice, R. Tournier, M. Ingold, P. Germi, M. Pernet, *Nature*, **1991**, *349*, 770–772; (b) A. E. Mikelson, Y. K. Karklin, *J. Cryst. Growth*, **1981**, *52*, 524–529; (c) T. Sugiyama, M. Tahashi, K. Sassa, S. Asai, *ISIJ Int.*, **2003**, *43*, 855–861.

(21) (a) Y. Yoshida, H. Tanaka, G. Saito, *Chem. Lett.*, **2007**, 1096–1097; (b) K. Nishimura, G. Saito, *Synth. Met.*, **2005**, *153*, 385–388.

(22) W. Fujita, K. Awaga, Y. Nakazawa, K. Saito, M. Sorai, *Chem. Phys. Lett.*, **2002**, *352*, 348–352.

(23) (a) Y. Galyametdinov, M. A. Athanassopoulou, K. Griesar, O. Kharitonova, E. A. Soto Bustamante, L. Tinchurina, I. Ovchinnikov, W. Haase, *Chem. Mater.*, **1996**, *8*, 922–926; (b) K. Binnemans, Y. G. Galyametdinov, R. Van Deun, D. W. Bruce, S. R. Collinson, A. P. Polishchuk, I. Bikchantaev, W. Haase, A. V. Prosvirin, L. Tinchurina, I. Litvinov, A. Gubajdullin, A. Rakhmatullin, K. Uytterhoeven, L. Van Meervelt, *J. Am. Chem. Soc.*, **2000**, *122*, 4335–4344.

(24) C. Zou, M. S. Wrighton, *J. Am. Chem. Soc.*, **1990**, *112*, 7578–7584.

(25) A. Vij, Y. Y. Zheng, R. L. Kirchmeier, J. M. Shreeve, *Inorg. Chem.*, **1994**, *33*, 3281–3288.

(26) G. M. Sheldrick, *SHELXL: Program for the Solution for Crystal Structures*, University of Göttingen, Germany, **1997**.

LIST OF PUBLICATIONS

(1)* "Magnetic memory based on magnetic alignment of a paramagnetic ionic liquid near room temperature"

Y. Funasako, T. Mochida, T. Inagaki, T. Sakurai, H. Ohta, K. Furukawa, T. Nakamura, *Chem. Commun.* **2011**, *47*, 4475–4477.

(2) "Charge-transfer salts of methylferrocenes with DCNQI derivatives (DCNQI = *N*,*N*'-dicyano-1,4-benzoquinonediimine). Crystal structures and magnetic properties"

Y. Funasako, T. Mochida, T. Sakurai, H. Ohta, *J. Organomet. Chem.* **2011**, *696*, 2621–2626.

(3) "Charge-transfer complexes from decamethylferrocene and 1,4-quinone derivatives: neutral–ionic phase diagrams for metallocene complexes"

T. Mochida, Y. Funasako, H. Azumi, *Dalton. Trans.* **2011**, *40*, 9221–9228.

(4) "Order-disorder phase transition with associated cell tripling in the (octamethylferrocene)(2,3-dichloro-1,4-naphthoquinone)$_2$ charge-transfer complex"

Y. Funasako, T. Mochida, K. Yoza, *J. Organomet. Chem.* **2012**, *698*, 49–52.

(5) "Solid-state structure of a tetrazole-substituted ferrocenium salt with weak intermolecular C–H···N hydrogen bonds"

T. Mochida, Y. Funasako, *Inorg. Chim. Acta* **2012**, *382*, 207–209.

(6)* "Thermal properties of alkyloctamethylferrocenium salts with TFSA and TCNE (TFSA = bis(trifluoromethylsulfonyl)amide and TCNE = tetracyanoethylene)"

Y. Funasako, K. Abe, T. Mochida, *Thermochim. Acta* **2012**, *532*, 78–82.

(7) "Assembled structures and magnetic properties of viologen–[M(mnt)$_2$] charge-transfer salts (mnt = maleonitriledithiolato; M = Cu, Ni, Pt)"

T. Mochida, Y. Funasako, T. Kishida, C. Kachi-Terajima, *Inorg. Chim. Acta* **2012**, *384*, 111–116.

(8) "Phase transitions and thermal properties of decamethylferrocenium salts with perfluoroalkyl-sulfonate and -carboxylate anions exhibiting disorder"

S. Hamada, Y. Funasako, T. Mochida, D. Kuwahara, K. Yoza, *J. Organomet. Chem.* **2012**, *713*, 35–41.

(9)* "Vapochromic Ionic Liquids from Metal-Chelate Complexes Exhibiting Reversible Changes in Color, Thermal and Magnetic Properties"

Y. Funasako, T. Mochida, K. Takahashi, T. Sakurai, H. Ohta, *Chem. Eur. J.* **2012**, *18*, 11929–11936.

(10) "Copper(II) solvatochromic complexes [Cu(acac)(N^N)(ligand)]BPh_4 with various axial ligands. correlation between coordination geometries and d-d transition energies (acac = Acetylacetonato, N^N = 1,10-Phenanthoroline, 2,2'-Bipyridyl)"

R. Horikoshi, Y. Funasako, T. Yajima, T. Mochida, Y. Kobayashi, H. Kageyama, *Polyhedron* **2013**, *50*, 66–74.

(11) "Thermochromic and solvatochromic Nafion films incorporating cationic metal–chelate complexes"

Y. Funasako, T. Mochida, *Chem. Commun.* **2013**, *49*, 4688–4690.

(12) "Crystal Structures and Phase-Transition Dynamics of Cobaltocenium Salts with Bis(perfluoroalkylsulfonyl)amide Anions: Remarkable Odd–Even Effect of the Fluorocarbon Chains in the Anion"

T. Mochida, Y. Funasako, T. Inagaki, M.-J. Li, K. Asahara, D. Kuwahara, *Chem. Eur. J.* **2013**, *19*, 6257–6264.

(13)*"Organometallic ionic liquids from alkyloctamethylferrocenium cations: thermal properties, crystal structures, and magnetic properties"

Y. Funasako, T. Inagaki, T. Mochida, T. Sakurai, H. Ohta, K. Furukawa, T. Nakamura, *Dalton Trans.* **2013**, *42*, 8317–8327.

(14)*"Ionic liquids from copper(II) complexes with alkylimidazole-containing tripodal ligands"

Y. Funasako, M. Nosho, T. Mochida, *Dalton Trans.* **2013**, *42*, 10138–10143.

(15) "A spin-crossover ionic liquid from the cationic iron(III) Schiff base complex"

M. Okuhata, Y. Funasako, K. Takahashi, T. Mochida, *Chem. Commun.* **2013***, 49*, 7662–7664.

(16) "Weak Ferromagnetism below 41 K and Structural Transition at 395 K in $CeIr_3B_2$ Single Crystal"

K. Kubota, E. Matsuoka, Y. Funasako, T. Mochida, T. Sakurai, H. Ohta, T. Onimaru, T. Takabatake, H. Sugawara, *J. Phys. Soc. Jpn.* **2013**, *82*, 104715.

(17) "Crystal Architectures and Magnetic Properties of Alkylferrocenium Salts with F_nTCNQ (n = 0, 2, 4): Effect of Substituents on the Self-assembled Structures"

T. Mochida, T. Akasaka, Y. Funasako, Y. Nishio, H. Mori, *Cryst. Growth Des.* **2013**, *13*, 4460–4468.

*Main publications directly related to this dissertation.

ACKNOWLEDGMENTS

The present work was carried out under the supervision of Professor Tomoyuki Mochida. I wish to thank him for his critical discussions and continuous encouragement. I also thank Professor Takashi Uchino and Professor Kazuyuki Takahashi for extremely beneficial advice.

I thank Professor Hitoshi Ohta and Professor Takahiro Sakurai for measurements and discussion of magnetic susceptibility and ESR spectra. I also thank Professor Toshikazu Nakamura and Professor Ko Furukawa for measurement of magnetic susceptibility. I am indebted to Ms. Misaki Nosho for their help with the preparation of the tripodal ligands. Thanks are also due to all members of the Solid-State Chemistry Laboratory for their help and friendship. In particular, I thank Dr. Takashi Inagaki for providing deep insights about this work. I wish to thank Dr. Ryo Horikoshi for useful discussions and encouragements. Finally, I am sincerely grateful to my parents for their continuous support and encouragement.

January, 2014

Yusuke Funasako